

**Deformation mechanisms of the equiatomic  
Cr-Co-Ni medium-entropy alloy**

**LI Le**

2022

## Abstract

Human civilization has been pursuing better structural materials to achieve higher energy efficiency and very recently, reduce the CO<sub>2</sub> emission. Conventional structural alloys are usually composed of a single principal element with addition of small amounts of other elements. In the recently decade, a new class of structural alloys referred as high- and medium-entropy alloys (HEA/MEAs), defined as equiatomic mixtures of multiple elements, has aroused considerable interest in the field of materials science. The research interest of the present work focuses on the equiatomic HEA/MEAs composed of chromium, manganese, iron, cobalt and nickel and its subset with the simple face-centered cubic (FCC) structure, particularly the ternary Cr-Co-Ni MEA.

Firstly, the plastic deformation behavior of equiatomic Cr-Co-Ni MEA was investigated in a wide temperature range. Compressive tests of  $[\bar{1}23]$ -oriented single crystals between 14 K to 1373 K were performed to illuminate the temperature dependence of critical resolved shear stress (CRSS) and thermal activation process. Tensile tests at ambient and cryogenic temperatures, combined with electron backscattering diffraction (EBSD) and (scanning) transmission electron microscopy (TEM/STEM), were carried out to shed light on the deformation mechanisms of the Cr-Co-Ni MEA. The very high yield strength was attributed mainly to the significant solid solution strengthening (SSS) and the overall behavior of thermal activation was not unlike those conventional FCC alloys. The excellent work hardening ability arose from the activation of deformation twinning and martensitic phase transformation during the large strain level deformation, which is the so-called twinning-induced plasticity (TWIP) and transformation-induced plasticity (TRIP) effect, respectively.

The next study concerns the atomic scale chemical short-range ordering (SRO) and the possible effects on mechanical properties in the equiatomic Cr-Co-Ni MEA. The electrical resistivity measurement was used to monitor the occurrence and evolution of SRO after various heat treatments. Neither simple electron or X-ray diffraction could not capture the SRO in Cr-Co-Ni MEA. Compressive and tensile tests of single crystals combined with TEM and EBSD observation revealed that the occurrence of SRO did not significantly affect the CRSS, dislocation structures, stacking fault energy (SFE) or twinning behavior in Cr-Co-Ni MEA.

The third study summarizes the plastic deformation behaviors of single crystals of the equiatomic quinary Cr-Mn-Fe-Co-Ni, quaternary Cr-Fe-Co-Ni, and ternary Cr-Co-Ni and Fe-Co-Ni both in tension and in compression as a function of temperature over a wide range 10-300 K, to systematic investigate the SSS effect, Labusch-type thermal activation process, SFE and twinning behavior in these HEA/HEAs. The SSS effect of these FCC HEA/MEAs can be well described both by traditional Labusch-type model and by the mean-square atomic displacement (MSAD) model, and the Cr contributes significantly to the atomic size misfit interaction between solutes and dislocations. The activation of deformation twinning and martensitic phase transformation is attributed to a relatively low SFE. The SFE is found to near linearly correlate to the chemical compositions of most of the FCC subsets of the equiatomic quinary Cr-Mn-Fe-Co-Ni.

The present study investigated the plastic deformation behaviors of single crystals of the equiatomic Cr-Co-Ni MEA both in tension and in compression as a function of temperature over a wide range 14-1373 K. Many important material parameters, including CRSS at 0 K and finite temperatures, SFE, twinning shear stress, are obtained in high-quality bulk single crystals without grain size effect. These results provide a

detailed scenery of deformation mechanisms and can be directly compared to those obtained from theoretical estimations. Moreover, unified strengthening and toughening mechanisms are preliminary established based on the (MSAD, SFE)-composition relationships, indicating the great potential for further improvement of mechanical performance by tuning compositions even within the regime of five elements (Cr, Mn, Fe, Co, Ni). These results can be widely used to develop other strong and ductile HEA/MEAs.

## Acknowledgments

*'My way ahead is long; I see no ending; yet high and low I'll search with my will unbending'* (路漫漫其修远兮，吾将上下而求索). Despite that pursuing the degree of Doctoral of Engineering may be the beginning or ending of an academic career, it will never be completed without the invaluable support from my surroundings. First of all, I would like to express deep gratitude to my advisor, Prof. Haruyuki Inui. He is the real researcher who is exactly like the description from a Confucian classic: Study Extensively, Enquire Accurately, Reflect Carefully, Discriminate Clearly, Practice Earnestly (博学, 审问, 慎思, 明辨, 笃行). I am grateful to have his critical insights and incisive comments to push this work forward throughout the past three years. He has always encouraged me to write academical articles and make presentations in academical conferences.

I am thankful to Associate Prof. Kyosuke Kishida for his patience and kindness in discussing and solving many problems in practice. He is an expert both at the field of electron microscopy and dealing with Prof. Inui, the abilities that are really indispensable for me to finish this work with a relatively stable mood. Perhaps he will never want to help me take diffraction patterns of FCC alloys anymore.

To Assistant Prof. Zhenghao Chen, my fellow and mentor, I cannot thank him enough for his support, both professionally and personally, for work and life. I am also grateful to other fellows here. The clink of beer, the battle in Texas Hold'em and Mahjong, hiking and mount climbing, all are invaluable things among the many frustrations during pursuing the doctoral degree.

I am also very grateful to Prof. Isao Tanaka and Prof. Hideyuki Yasuda of Kyoto University, who were my dissertation committees. I thank other members of Inui group for their help on my research, particularly Dr. Kodai Niitsu (now in NIMS), Dr. Equbal Ashif, Mr. Kazuki Ehara and the secretary Ms. Miki Hazui. I am also thankful for the financial support from the Kyoto University Graduate Division Fellow.

Finally, I am indebted into my wife, Mrs. Zhang. I know that without her I would never started the journey of a doctoral program, let along finally finished it. While a husband and a father in 30s is generally supposed to work full-time to support his family, I am so fortunate to have the opportunity to pursuing a different goal with her support. While it is easily overwhelmed by the tough and tricky work under pressures, she and my daughter always remind me that life is far more just than work. I am also deeply indebted into my parents, Mr. Li and Mrs. Fan for the constant and unconditional support in the past 31 years of my life. Being tenacious, diligent, optimistic, modest, they have always been the role model of my life. Without them I would never be who I am now.

## Vita

- 1991 Born in Macheng, Hubei Province, China
- 2010-2014 B.S., Materials Science and Engineering,  
Huazhong University of Science and Technology,  
Wuhan, Hubei Province, China
- 2014-2017 M.S., Materials Science and Engineering,  
Huazhong University of Science and Technology,  
Wuhan, Hubei Province, China
- 2019-present Doctoral candidate, Materials Science and Engineering,  
Kyoto University,  
Kyoto, Japan

## Publication list

- [1] **Le Li**, Zhenghao Chen, Shogo Kuroiwa, Mitsuhiro Ito, Kyosuke Kishida, Haruyuki Inui, Easo P. George, Tensile and compressive plastic deformation behavior of medium-entropy Cr-Co-Ni single crystals from cryogenic to elevated temperatures, *International Journal of Plasticity*, Vol. 148, 103144, January, 2022.
- [2] Haruyuki Inui, Kyosuke Kishida, **Le Li**, Anna Maria Manzoni, Sebastian Haas, Uwe Glatzel, Uniaxial mechanical properties of face-centered cubic single-and multiphase high-entropy alloys, *MRS Bulletin*, Vol. 47, pp. 1 – 7, February, 2022.

# Contents

<b>Abstract .....</b>	<b>I</b>
<b>Acknowledgments.....</b>	<b>IV</b>
<b>Vita.....</b>	<b>VI</b>
<b>Publication list .....</b>	<b>VI</b>
<b>Contents.....</b>	<b>VII</b>
<b>Chapter 1 Introduction .....</b>	<b>1</b>
1.1 Background.....	1
1.2 High-entropy alloys .....	3
1.2.1 High-entropy hypothesis .....	3
1.2.2 HEAs with the face-centered cubic structure .....	6
1.3 Solid solution strengthening in FCC alloys.....	9
1.4 Deformation mechanisms in FCC alloys.....	11
1.5 Chemical short-range ordering .....	14
1.6 The objectives of the present study .....	17
Reference.....	18
<b>Chapter 2 Plastic deformation of single crystals of the equiatomic Cr-Co-Ni.....</b>	<b>21</b>
2.1 Introduction .....	21
2.2 Materials and methods.....	23
2.3 Results .....	25

2.3.1 Quality of single crystals .....	25
2.3.2 Compressive deformation.....	27
2.3.3 Tensile deformation .....	36
2.4 Discussion.....	49
2.4.1 Slip behavior.....	49
2.4.2 Twinning behavior .....	53
2.5 Conclusions .....	56
Supplementary figures .....	58
Reference .....	58
<b>Chapter 3 Short-range order in the equiatomic Cr-Co-Ni MEA.....</b>	<b>64</b>
3.1 Introduction .....	64
3.2 Materials and experiments.....	67
3.3 Results .....	69
3.3.1 Electrical resistivity .....	69
3.3.2 Observation of SRO.....	72
3.3.3 Mechanical properties.....	77
3.4 Discussion.....	90
3.4.1 Evidence of the existence of SRO .....	90
3.4.2 Microstructural evolution accompanying SRO .....	91
3.4.3 Changes in mechanical properties with SRO .....	93
3.5 Conclusions .....	100
Supplementary figures.....	102
Reference .....	105

<b>Chapter 4 Strengthening mechanisms in HEA/MEAs .....</b>	<b>112</b>
4.1 Introduction .....	112
4.2 Materials and methods.....	116
4.3 Results .....	117
4.3.1 Compression deformation behavior .....	117
4.3.2 Tensile deformation behavior .....	119
4.4 Discussion.....	122
4.4.1 Solid solution strengthening in HEA/MEAs .....	122
4.4.2 Mean-square atomic displacement .....	130
4.4.3 SFE and ductility of HEA/MEAs .....	133
4.5 Conclusions .....	137
Reference .....	138
<b>Chapter 5 Summary .....</b>	<b>141</b>

# Chapter 1 Introduction

## 1.1 Background

From the Bronze Age, human civilizations have been benefiting from the design, modification and applications of advanced structural materials. Increasing the reliability of civil engineering with advanced materials protects publics from catastrophic failures; the application of structural alloys with high specific strength on automobiles significantly reduces the fossil fuels consumption and carbon dioxide emission; gas and steam turbines operated at higher temperatures effectively improve the energy conversion efficiency of power plants: the development of better alloys plays a crucial role in that to what extent these objectives could be achieved in practice. Historically, the development of structural alloys has been constrained to the use of a single principal base metallic element (solvent) with addition of small amounts of other elements (solute), which is also reflected on the name of our structural materials (Aluminum alloys, Iron-base alloys, Nickel-base alloys). However, this one-principal-base convention actually limits the total number of alloys since the composition adjustment is inherently confined near one corner of the phase diagram. More importantly, these conventional alloys generally cannot satisfy all the manufacturing/performance requirements and inevitably suffer from significant tradeoffs. For example, it is well known that stronger materials usually exhibit terrible ductility and vice versa. This strength-ductility tradeoff has long been a dilemma in materials science and practical applications. While minor composition modifications combined with complicated thermal-mechanical process are applied to optimize

conventional alloys, endeavors to exploring the wide-open virgin land of phase diagram provide infinite and fascinating possibilities in the kingdoms of metallic materials.

A new class of alloys referred as high- and medium-entropy alloys (HEA/MEAs), originally defined by equiatomic mixtures of multiple elements, has aroused considerable interest in the field of materials science. Many reasons can be found for the extensive attraction from the research of HEAs in the recent decade, among which the atomic-scale structures for multi-component alloys solidified as overall solid solutions with simple crystal structures, and the micro-scale origins of their (some of them) excellent mechanical properties, have been standing in the spotlight on the stage of HEAs. On the other hand, the development of new HEAs has got rid of the original “equiatomic solid solution alloys” and countless non-equiatomic novel HEAs with high strength and ductility/toughness have been reported, which is albeit somehow arbitrary considering two facts that 1) no definite key material parameter that controlling the mechanical properties of HEAs is proposed and 2) no correlation between the composition and these potential key parameters is established even in the single phase HEAs with simple crystal structures.

To that end, the research interest of the present work focuses on the equiatomic HEAs composed of chromium, manganese, iron, cobalt and nickel and its subset with the simple face-centered cubic (FCC) structure, particularly the ternary Cr-Co-Ni alloys. The equiatomic Cr-Co-Ni alloy is one of the only a few solid solution HEA/MEAs and it exhibits one of the highest strengths among the quaternary and ternary derivatives of the Cr-Mn-Fe-Co-Ni HEA system, and excellent tensile ductility that increases with decreasing temperature. The present work investigated the plastic deformation behavior and atomic-scale structures of the equiatomic Cr-Co-Ni to shed light on the origin of its

superior mechanical properties. The research work of Cr-Co-Ni also serves as a prototype for the following investigation of other derivatives of the Cr-Mn-Fe-Co-Ni HEA to systematically and quantitatively describe their mechanical properties.

## 1.2 High-entropy alloys

### 1.2.1 High-entropy hypothesis

A phase can be defined as a stable portion with the same crystal structure, homogeneous composition and properties, which is distinguished from other parts by phase interfaces. The relative stability of one specific phase, compared to others, can be simply determined by the Gibbs free energy ( $G$ ) by the following equation

$$G = H - TS \quad (1-1)$$

Where  $H$  is the enthalpy,  $T$  is the absolute temperature,  $S$  is the entropy. From eq. (1-1) it is clear that the decrease of enthalpy and the increase of temperature or entropy will lower down the Gibbs free energy thus increase the phase stability. The configuration entropy  $S_{conf}$ , which is one of terms in the total entropy  $S$ , is expressed by the following Boltzmann equation

$$S_{conf} = k \ln m \quad (1-2)$$

in which  $k$  is the Boltzmann constant,  $m$  is the number of possible combination of atomic species. The change of entropy by mixing multi elements can be estimated as

$$\Delta S_{mix} = -R \sum_n c_n \ln c_n \quad (1-3)$$

Where  $R$  is the ideal gas constant,  $c_n$  is the atomic fraction of constituent atom  $n$ . According to eq. (1-2) and (1-3), the magnitude of configuration entropy increases with the number of constituent elements and is maximized by an equal mixture of each element

at a given element number. This high-entropy contributed phase stability was adopted to explain and predict the formation of multi-element solid solutions (SS) by Yeh [1] and is the most important one of the four core effects of these alloys [2]. Further, these alloys are classified into high-entropy alloys with configuration entropy  $> 1.5R$  and medium entropy alloys (MEA) with configuration entropy between  $R$  and  $1.5R$ . However, this high-entropy hypothesis has been clouded by the fact that both SS and intermetallics (IM) are observed frequently in HEA/MEAs. In the view paper by Miracle [2], 309 of 648 (48%) work reports SS microstructures while 268 (42 %) reports the mixtures of SS and IM, the left 66 (10%) alloys have only IM. Among the 309 SS alloys only 163 are single phase (25% of the total 648), as shown in Fig. 1.1.

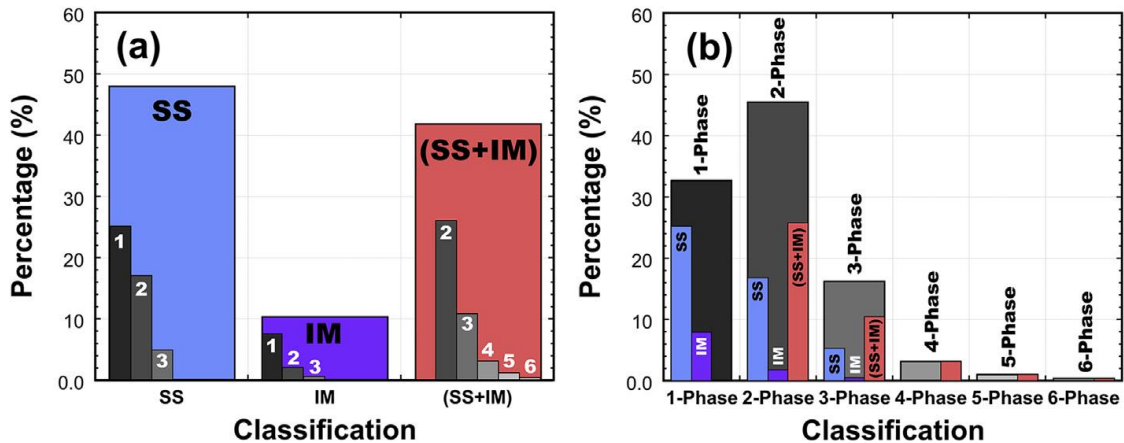


**Fig. 1.1** (a) Microstructure classification by phase type with sub-classification by the number of phases. (b) Classification by number of phases with sub-classification by the phase types [2].

Of important to note that the most common single phase SS alloys are with the face-centered cubic (FCC) structure, all of which are composed of 3d transition metals. While the high configuration entropy may contribute to the phase stability of solid solution HEAs, it is not supposed to be the determinative and exclusive factor.

A scrutiny of eq. (1-1), which should be strictly expressed for solid solutions as the following

$$G^{SS} = H^{SS} - TS^{SS} \quad (1-4)$$

All the symbols denote the same physical meanings as in eq. (1-1) but for SS. For ideal solutions mix enthalpy  $H^{SS-ideal}=0$  and the ideal configuration  $S^{SS-ideal}$  can be expressed as eq. (1-2) and (1-3). This also approximately holds true for regular solutions in which  $H^{SS} \neq 0$  but is very small. For sub-regular solutions, the atom arrangement deviates from the random state, the tendency of which depends on the mix enthalpy. When  $H^{SS} > 0$  phase separation tends to occur, and chemical short-range order (SRO) may occur for  $H^{SS} < 0$ . Previous calculation work has reported that 85 % of 1176 binary metallic systems are sub-regular, i.e. non-random solutions even at liquid state [3]. In real materials at solid state, the magnitude of mix enthalpy is supposed to be higher and its effect on phase stability should be more significant.

The results in Ref. [3] also provide addition hint from the term of mix enthalpy for the preference of 3d-transition metals in the formation of single phase FCC HEAs as afore-mentioned. Table 1.1 lists mixing enthalpy of equiatomic binary among Cr, Mn, Fe, Co, Ni. For the 10 binary systems, 8 are with negative mix enthalpy within the range from -8.2 kJ/mol (Mn-Ni) to -0.2 kJ/mol (Co-Ni), and the only two positive values come from Cr-Mn (2.1 kJ/mol) and Mn-Fe (0.2 kJ/mol).

The negative mix enthalpy will decrease the Gibbs free energy and favor the solid solution stability. Moreover, the magnitude of mix enthalpy is relatively small when compared with some well-known binary systems that forms intermetallics, such as the L1<sub>2</sub> order phase composed of Al and Ni with the binary mix enthalpy of -22.3 kJ/mol [3]. This may prevent the SS from deleterious phase separation of some brittle intermetallics, albeit the mix enthalpies of ternary, quaternary or quinary systems of these elements are not clear.

**Table 1.1** The mixing enthalpy of equiatomic binary among Cr, Mn, Fe, Co, Ni [3].

Alloy	Mixing enthalpy (kJ/mol)
Cr-Mn	2.1
Cr-Fe	-1.5
Cr-Co	-4.5
Cr-Ni	-6.7
Mn-Fe	0.2
Mn-Co	-5.2
Mn-Ni	-8.2
Fe-Co	-0.6
Fe-Ni	-1.6
Co-Ni	-0.2

### 1.2.2 HEAs with the face-centered cubic structure

In 2004, Cantor [4] first reported an equiatomic Cr-Mn-Fe-Co-Ni multi-component alloys that formed a single FCC solid solution with severe segregation among the dendritic structures. The subsequent work further confirmed the single FCC structure of the alloy and the dendritic structures could be effectively eliminated by traditional homogenization, cold rolling and annealing treatments [5,6]. Since then, the Cr-Mn-Fe-Co-Ni HEA has attracted remarkable attention due to its intriguing mechanical properties. The Cr-Mn-Fe-Co-Ni HEA can achieve a yield strength of 410 MPa and strain to failure of 57% at 293 K [7], which are comparable to that of many advance alloys like austenitic stainless steels and twinning-induced plasticity (TWIP) steels. The yield strength and strain to failure even simultaneously increase at cryogenic temperatures. This HEA

exhibits extraordinary fracture toughness ( $K_{JIC}=220 \text{ MPa}\cdot\text{m}^{1/2}$ ) from 293 K to 77 K [7], which surpasses that of all pure metals and metallic alloys.

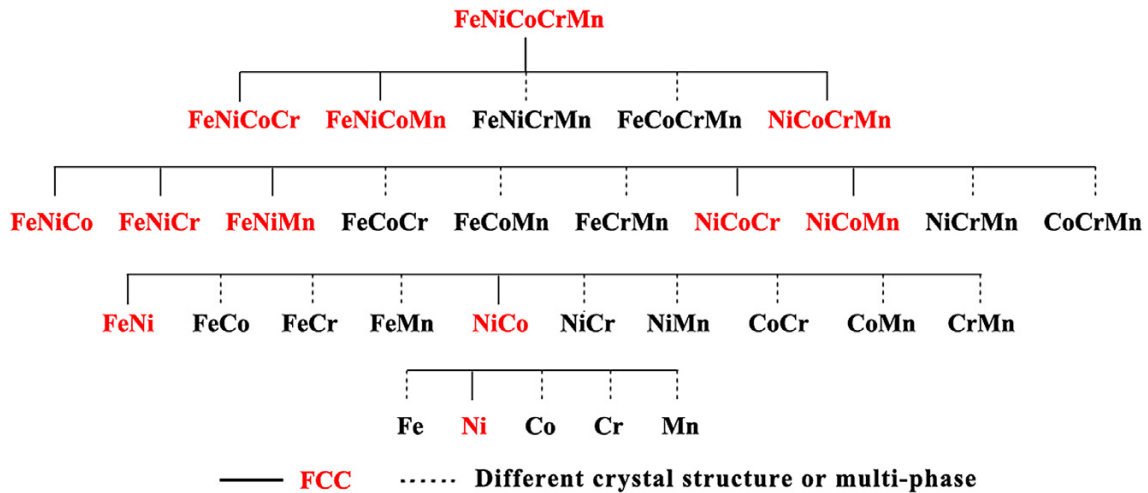


**Fig. 1.2** All the quaternary, ternary, binary and pure metal subsets of the quinary Cr-Mn-Fe-Co-Ni HEA [5].

A systematic work by Wu [5] examined the microstructures all the equiatomic MEA subsets derived from the Cr-Mn-Fe-Co-Ni HEA, as shown in Fig. 1.2. In contrast to the high-entropy hypothesis, only 3 of 5 quaternary, 5 of 10 ternary and 2 of 10 binary subsets possessed a simple FCC structure, all of which contained Ni but not vice versa. Furthermore, the mechanical properties of the above alloys were investigated and the results at 293 K are summarized as in Fig. 1.3 [6]. Apparently, neither the strength nor the ductility is necessarily related to the number of constituent elements. Generally, the alloys containing more Cr possess higher strength. The ternary equiatomic Cr-Co-Ni MEA exhibits both better strength and ductility than the Cr-Mn-Fe-Co-Ni and all other subsets. Gludovatz [8] reported the superior fracture toughness ( $K_{JIC}=275 \text{ MPa}\cdot\text{m}^{1/2}$ ) of Cr-Co-Ni than that of the Cr-Mn-Fe-Co-Ni at cryogenic temperatures.

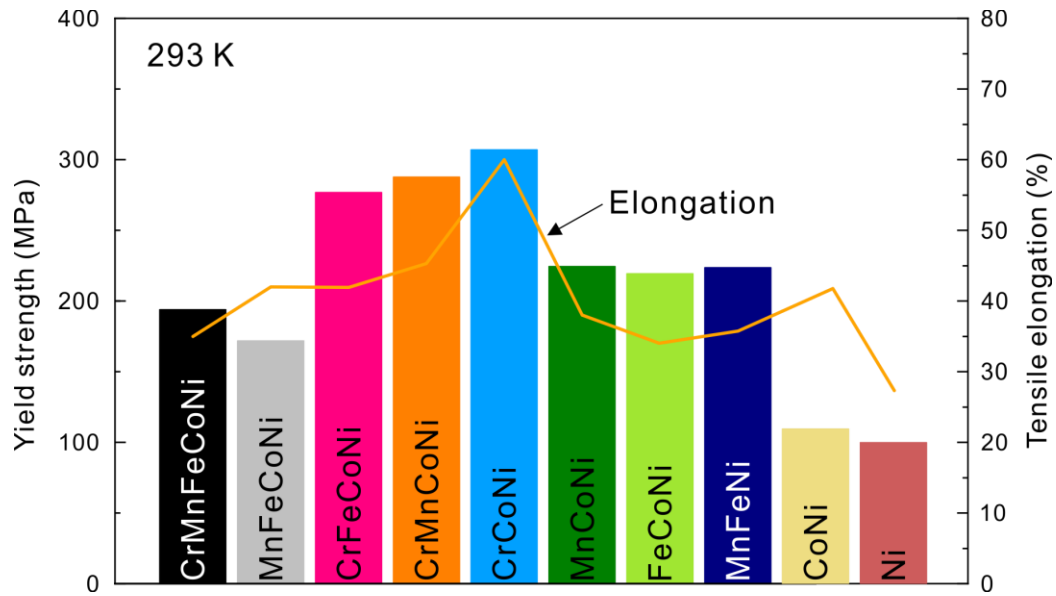


**Fig. 1.3** Yield strength and tensile elongation of the FCC subsets of Cr-Mn-Fe-Co-Ni [6].

The origins of extraordinary mechanical properties of HEA/MEA are investigated extensively both from theoretical calculations and experimental work. It has been widely accepted that the high yield strength of HEA benefits from the significant substitutional solid solution strengthening (SSS) excepting for some argument that chemical SRO may also play a role, even though without clear distinguishing of solute and solvent atoms. The critical resolved shear stress (CRSS) of the HEA/MEA is much higher than those of pure FCC metals and some binary FCC alloys but not exceptionally high when compared with those of some FCC solid solution alloys. On the other hand, the high ductility has been attributed to deformation twinning and even deformation-induced phase transformations, whose propensity is believed to increase with decreasing stacking fault energy. This is not unexpected since before the mechanical tests the Zaddach [9] already reported the SFE between 20-30 mJ/m<sup>2</sup> by density functional theory (DFT) and X-ray diffraction (XRD) in Cr-Mn-Fe-Co-Ni, which has been further verified from the partial dislocation dissociation width of single crystals. While these SFE values are supposed to be low enough for the occurrence of deformation twinning and phase transformation, they

are also comparable to those of the austenitic stainless steels and many Cu based binary alloys. In short, the excellent mechanical properties of these FCC HEA/MEA are exciting and promising but not unprecedented when compared with some single principal element based conventional alloys.

### **1.3 Solid solution strengthening in FCC alloys**

The solid solution strengthening (SSS) has been well established in binary alloy systems owing to the work by Fleischer and Labusch. These SSS models treat the stationary solute atoms as obstacles against the gliding dislocations and the predominant solute-dislocation interaction arises from the combination of two aspects: the size misfit and modulus misfit in the solid solutions. In Fleischer model [10], a solute atom in the solvent is assumed to be isolated from the others thus the dislocations are pinned by these isolated pinning solute atoms (strong pinning). Naturally, only for very dilute solute concentration ( $<1$  at.%) the assumption can still hold true and the model is applicable. Based on Fleischer's model, Labusch [11] considered the spatial distribution of solute atoms in higher concentration (several at.%) and assumed a statistical variation of solute-dislocation interaction energies. Taking a step forward, Gypen and Deruyttere [12,13] proposed the model to quantitate the SSS in multi-component alloys by assuming that there is no (or very small) interaction among solute atoms. All of these SSS models show good agreement within some reported experimental results of conventional alloys. However, the key parameter of all these SSS models is the solute-dislocation interaction, which seems to be not applicable in equiatomic HEAs since the solute cannot be clearly defined. In addition, the very high concentration (33.3 at.% for ternary MEAs) also seems far beyond the concentration limitation of Labusch model.

Recently, several new attempts have been made to model the SSS in HEAs including the equiatomic Cr-Mn-Fe-Co-Ni system. Toda-Caraballo [14] further developed the model proposed by Gypen and Deruyttere [12,13] and considered each constituent element as the solute with respect to the others to calculate the size misfit and modulus misfit. Similarly, Curtin [15,16] also estimated the misfit volume (the equivalent of size misfit) of each constituent element with respect to an assumed effective medium matrix. On top of that, in both models, the size misfit predominates the SSS in edge dislocation controlled FCC HEAs. It is important to note that all atoms in HEAs are expected to be displaced from the ideal lattice positions due to the different atomic sizes of constituent elements. An alternative approach to describe the size misfit is thus to consider the displacement. The Mean-square atomic displacement (MSAD) was proposed to quantify the lattice distortion and rationalize SSS in the Cr-Mn-Fe-Co-Ni system.

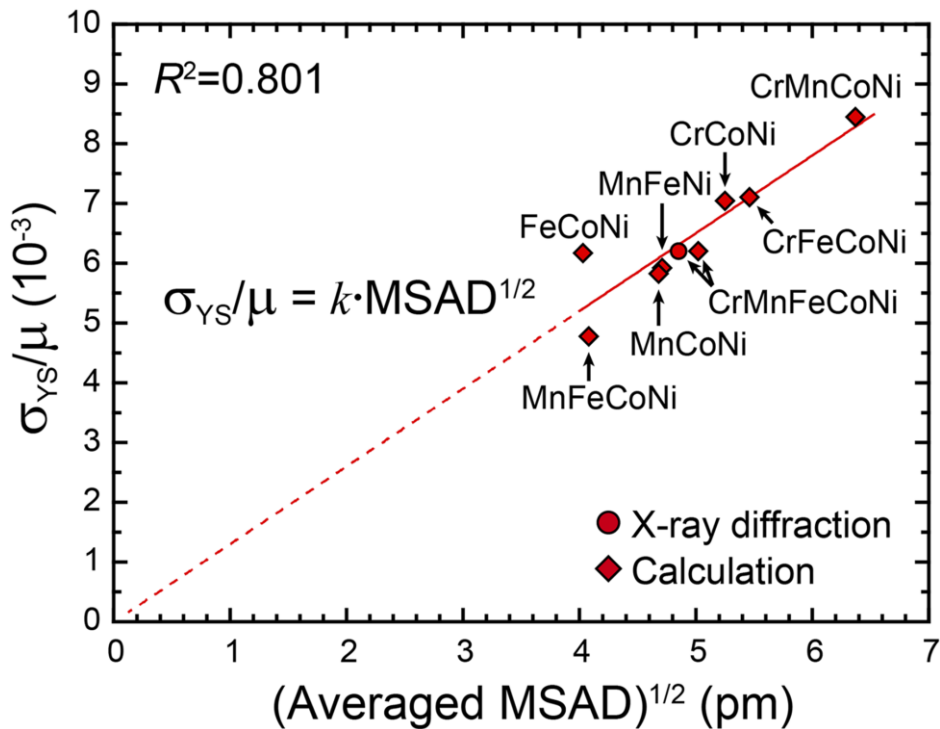


**Fig. 1.4** Yield stress at 0 K normalized by shear modulus plotted against the square root of average MSAD [17].

As shown in Fig. 1.4 [17], the yield strengths at 0 K normalized by shear modulus obtained from polycrystals of the Cr-Mn-Fe-Co-Ni families exhibit rough linear correlation with square root of the average MSAD. It is of great significance that it suggests that the resistance to dislocation motion is controlled by the lattice distortion. More importantly, it breaks the conventional solute-solvent concept and there is no concentration limitation that requires to consider the solute-dislocation interaction force. The MSAD model is a promising scaling factor to explain and predict the SSS in concentrated solid solutions. However, it is well known that polycrystals always suffer the grain size effect on yield strength, which will affect the evaluation of the contribution of SSS. Therefore, experimental results from single crystals are required to scale the SSS by MSAD model in high and medium entropy alloys.

#### **1.4 Deformation mechanisms in FCC alloys**

The strength-ductility combination can be achieved by introducing multiple deformation mechanisms along with the plastic deformation proceeding, such as the deformation twinning and martensite transformation, known as the twinning-induced plasticity (TWIP) and transformation-induced plasticity (TRIP) effect. Both the TWIP and TRIP have been observed in Cr-Fe-Ni austenitic stainless steels, Fe-Mn-C steels and the present HEAs/MEAs, and a relatively low stacking fault energy has been well accepted as the trigger of TWIP/TRIP effect in FCC alloys. In the review paper of TWIP steels [18], the influence of  $\gamma_{isf}$  on deformation mechanisms in some Fe-base FCC alloys was summarized, as shown in Fig. 1.5. An empirical criterion was also concluded for the relationship between  $\gamma_{isf}$  and deformation model: 1)  $\gamma_{isf} > 45 \text{ mJ/m}^2$  results in

perfect dislocation glide; 2)  $15 < \gamma_{isf} < 45 \text{ mJ/m}^2$  is responsible for TWIP effect; 3)  $\gamma_{isf} < 15 \text{ mJ/m}^2$  induces TRIP effect. Therefore, by manipulating the intrinsic stacking fault energy, the deformation mechanism can be effectively controlled.

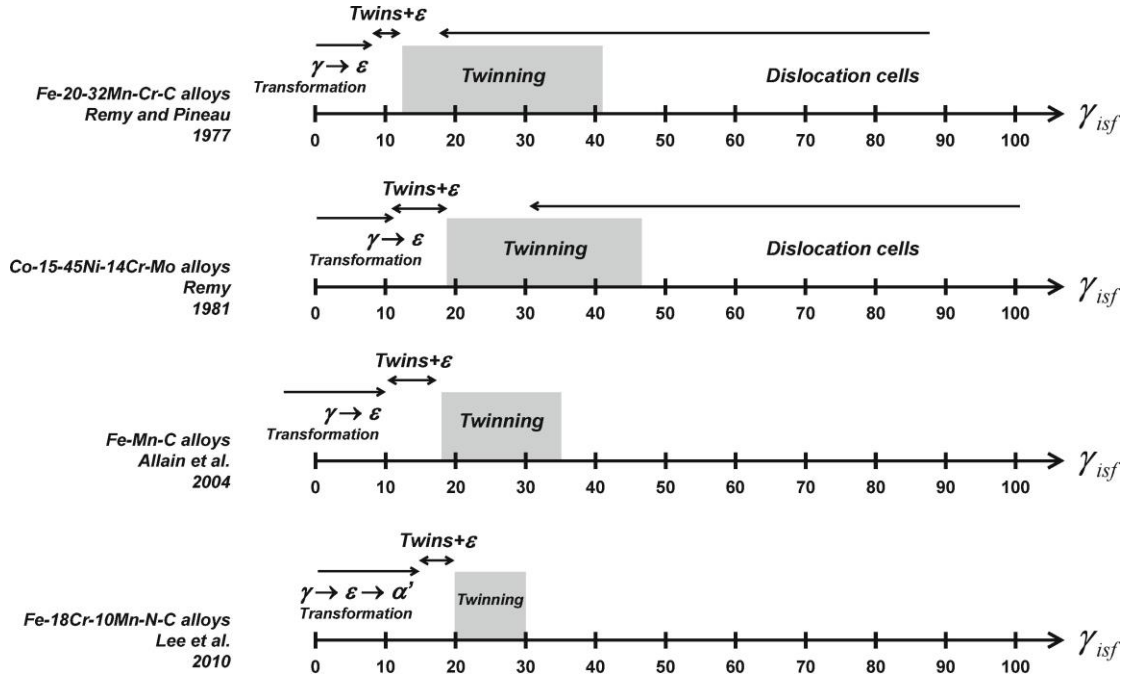


**Fig. 1.5** Ranges of the intrinsic stacking fault energy  $\gamma_{isf}$  for dislocation glide, deformation twinning and phase transformation in FCC alloys [18].

On the other hand, the intrinsic stacking fault energy  $\gamma_{isf}$  can be expressed as [19]

$$\gamma_{isf} = 2\rho_A \Delta G^{FCC \rightarrow HCP} + 2\sigma^{FCC \rightarrow HCP} \quad (1-5)$$

where  $\Delta G^{FCC \rightarrow HCP}$  is the Gibbs free energy difference between the FCC and HCP (hexagonal close-packed) phase,  $\rho_A$  is the planar packing density of a close-packed plane,  $\sigma^{FCC \rightarrow HCP}$  is the FCC-HCP interfacial energy. Since the interfacial energy of transition metals has been reported to be  $10 \pm 5 \text{ mJ/m}^2$  [19], the  $\gamma_{isf}$  mainly depends on the Gibbs free energy difference between FCC and HCP phase, i.e. the relative stability of FCC with respect to HCP phase.

The effect of alloying on  $\gamma_{isf}$  has been investigated with transition metals in Ni binary alloys [20] (Fig. 1.6). For Ni-base binary alloys, the results in Fig. 1.6 indicate that Cr, Mn and Co are effective to decrease the  $\gamma_{isf}$  while Fe has little influence. While it remains unclear whether similar relationships still hold true or not in the complex Cr-Mn-Fe-Co-Ni system, it is promising to tune the  $\gamma_{isf}$  by tailoring the chemical compositions of the FCC HEA/MEAs.

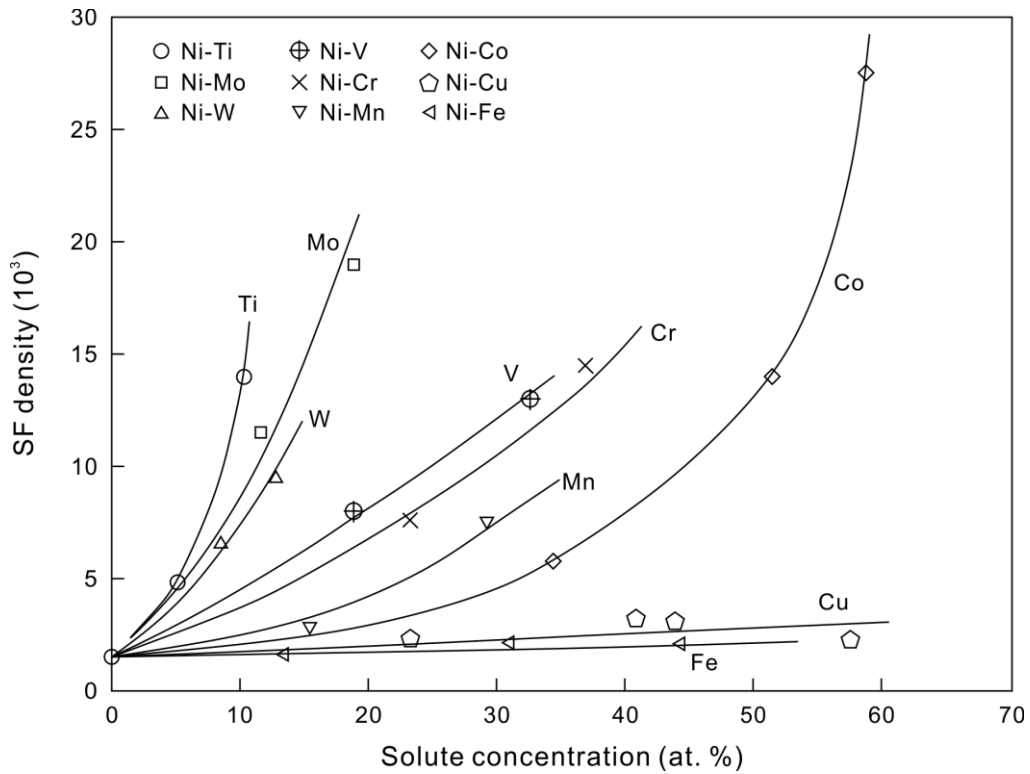


**Fig. 1.6** The stacking fault density (proportional to  $\gamma_{isf}$ ) vs. solute concentration for Ni-alloys with transition metals re-drawn from Ref. [20].

The above results suggest that the deformation mechanisms can be controlled by tuning the  $\gamma_{isf}$  through composition adjustment, but a quantitative relationship between the deformation twinning behavior and the  $\gamma_{isf}$  remains unclear. In polycrystals the twinning behavior is significantly affected by the grain size effect. Therefore, single

crystals results are also needed to precisely investigate the twinning behavior and its relation to SFE.

## 1.5 Chemical short-range ordering

As mentioned in section 1.2.1, negative mix enthalpy of the binary system will result in chemical SRO, i.e. some specific bond pairs are energetically preferred than the others within the nearest neighbor shells over the lattice. For a binary A-B system with the negative mix enthalpy, the number of A-B bonding pairs are higher than that of the completely random solid solution, as illustrated in the schematic Fig. 1.7 [21], where the completely disordered solid solutions (Fig. 1.7(a)), SRO with increased number of A-B bonds (Fig. 1.7(b)) and the completely long-range ordered state (Fig. 1.7(c)) are shown.

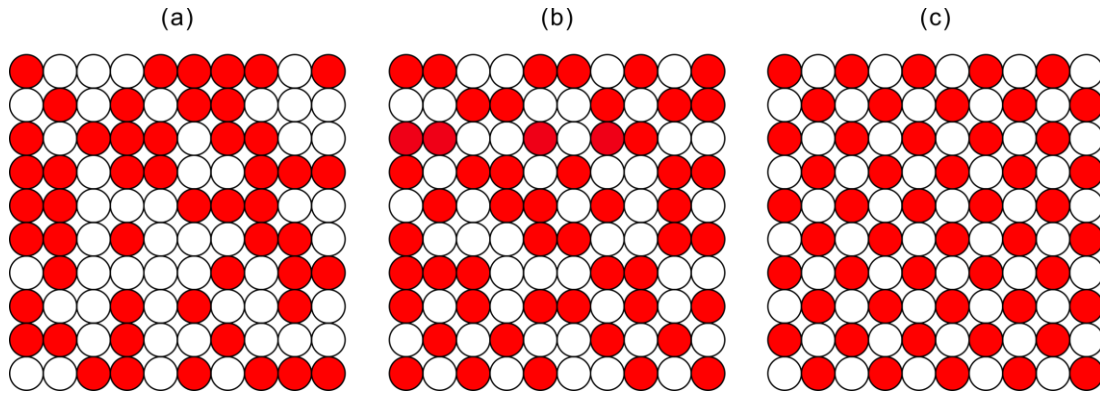


**Fig. 1.7** Schematic illustration of (a) random solid solution, (b) short-range ordering, with increased number of A-B bonds (c) long-range order of an A-B binary system [21].

The degree of SRO in the A-B binary system can be quantitatively expressed by the Warren-Cowley parameter [22]

$$\alpha_i = 1 - \frac{P_{BA_i}}{c_A}, P_{BA_i} = \frac{n_{A_i}}{z_i} \quad (1-6)$$

Where  $i$  is the atomic shell around the center atom B,  $P_{BA_i}$  is the proportion of A-B bonding pairs on the  $i$  shell,  $c_A$  is the atomic fraction of A atom,  $n_{A_i}$  is the number of A

atoms on the  $i$  shell,  $Z_i$  is the total number of atoms on the  $i$  shell, i.e. the coordinate number.

**Table 1.2** The mixing enthalpy of some equiatomic binaries [3].

Alloy	Mixing enthalpy (kJ/mol)
Ni-Cr	-6.7
Ni-Mo	-7.3
Cu-Al	-7.6
Cu-Au	-8.8
Au-Ag	-5.5

SRO has been investigated for several decades in many conventional FCC alloys, typically as Ni-Cr [23,24], Ni-Mo [25], Cu-Al [26-28] and Cu-Au [29,30] alloys. It is not occasional when we note that all these equiatomic binaries have negative mixing enthalpy values as in Table 1.2, which may be indicative of the occurrence of SRO.

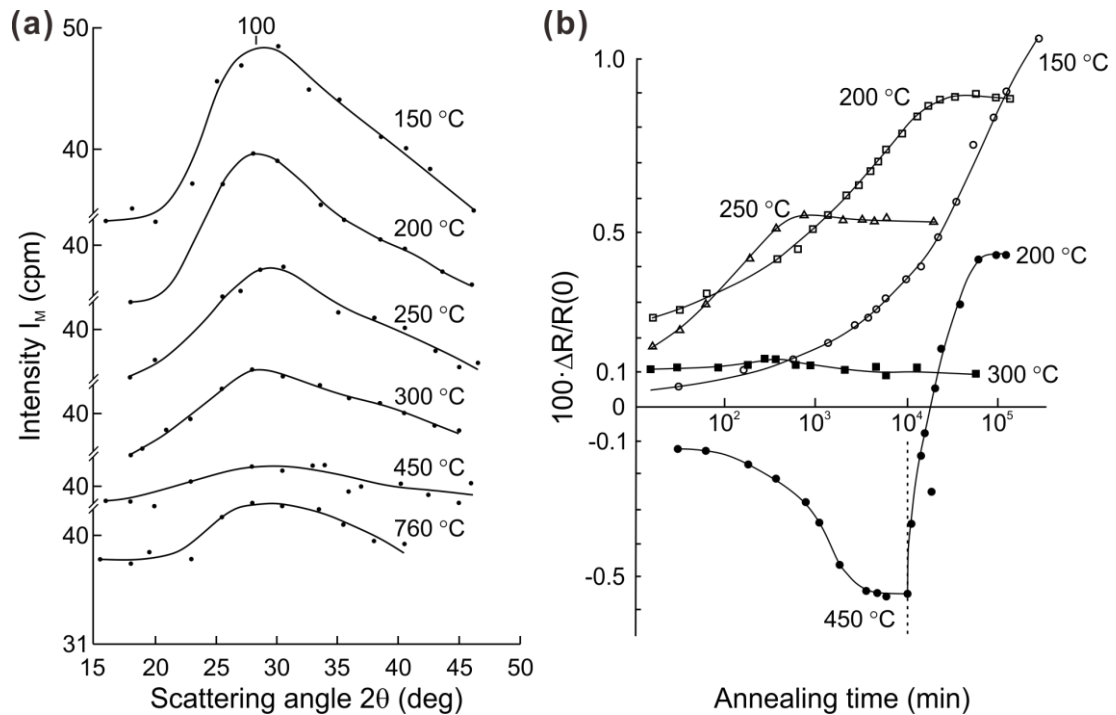


**Fig. 1.8** (a) The scattered X-ray intensity and (b) electrical resistance change of Cu-Au alloys after isothermal annealing at various temperatures [29].

The existence of SRO has been verified by x-ray, neutron or electron diffraction, usually combined with electrical resistivity measurements or specific heat measurements in these alloys [23-30]. For X-ray or neutron diffractions, the additional forbidden reflections for FCC (such as 100 or 110) have indicated the formation of SRO in Cu-Au alloy, as shown in Fig. 1.8 [29]. The intensities of the additional reflections are in good agreement with the electrical resistivity change after isothermal annealing, and both imply the development of SRO in Cu-Au alloy.

For electron diffraction, the diffuse intensities at the positions of  $1/3\{422\}$  in  $[111]$  zone axis selected area electron diffraction (SAED) were first proposed as the evidence for SRO in Ni-25Cr alloys by Maruccio [23]. Subsequently, observation of  $1/2\{311\}$  diffuse intensities in  $[112]$  SAED were also attributed to the existence of SRO in Cr-Fe-Ni alloys [31].

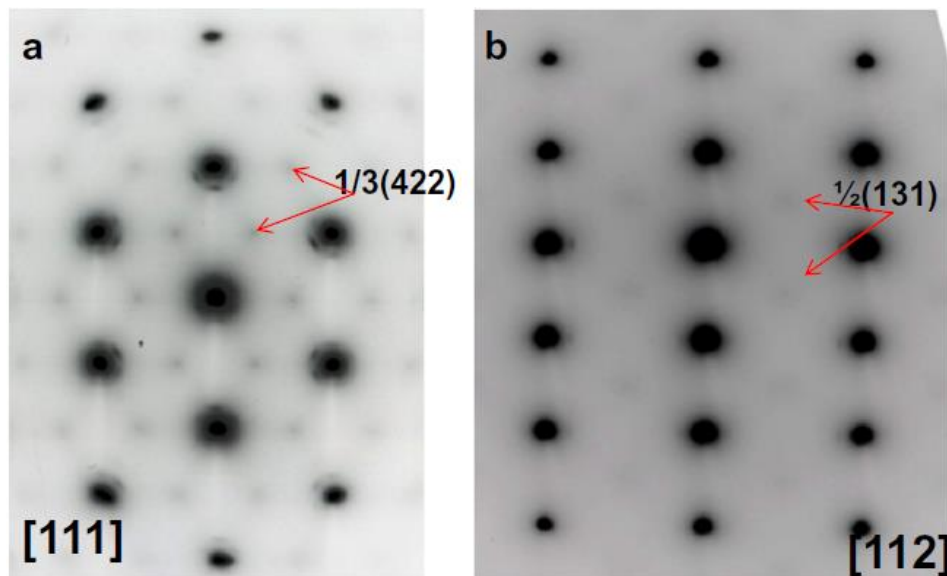


**Fig. 1.9** The diffuse intensities at the positions of  $1/3\{422\}$  and  $1/2\{311\}$  of Alloy 600 after slow strain rate tensile tests at 633 K [31].

Fig. 1.9 shows the [111] and [112] zone axes SAED of the Alloy 600 after slow strain rate tensile tests at 633 K [31]. In recently years, similar diffuse intensities are also observed in some FCC HEA/MEAs and adopted as the evidence of SRO. Efforts are also made to record the atomic-scale contrast by using these diffuse intensities as the operating reflections [32–35]. However, the verification of SRO by electron diffraction has been remaining a big challenge and controversy ever since the first attempt when considering the sophisticated transmission electron microscopy (TEM). It is never too careful to correctly interpret the origins of any observed contrast by TEM since it may arise from many other factors other than SRO.

## **1.6 The objectives of the present study**

In the present work, the equiatomic Cr-Co-Ni, with the best combination of strength and ductility among these FCC high and medium entropy alloys, are selected as the research object. Single crystals are used for mechanical tests to avoid the uncertainty of grainsize effect. The plastic deformation behavior and SRO of the alloy are investigated in order to reveal the deformation mechanisms and illustrate the mechanisms for high strength and ductility for this alloy.

The second chapter investigates the plastic deformation behavior of single crystals of the equiatomic Cr-Co-Ni both in tension and in compression as a function of temperature over a wide range, 14-1373 K, in order to experimentally deduce materials parameters.

The third chapter contains the electrical resistivity and plastic deformation behavior of polycrystalline and bulk single crystals of the equiatomic Cr-Co-Ni both in tension and in compression as a function of annealing temperature and duration, in order to

experimentally study the occurrence, evolution and effects of SRO on materials parameters.

The forth chapter summarizes the plastic deformation behavior single crystals of equiatomic Cr-Mn-Fe-Co-Ni, Cr-Fe-Co-Ni and Fe-Co-Ni. The solid solution strengthening and deformation twinning behaviors are discussed to provides insights into the mean-square atomic displacement (MSAD) and stacking fault energy (SFE) as the key material parameters controlling the strength and ductility of HEAs. The correlations between alloy compositions and MSAD and SFE are also studied.

Chapter 5 is the summary of all the above results.

## Reference

- [1] J.W. Yeh, S.K. Chen, S.J. Lin, J.Y. Gan, T.S. Chin, T.T. Shun, C.H. Tsau, S.Y. Chang, Nanostructured High-Entropy Alloys with Multiple Principal Elements: Novel Alloy Design Concepts and Outcomes, *Adv. Eng. Mater.* 6 (2004) 299–303. <https://doi.org/https://doi.org/10.1002/adem.200300567>.
- [2] D.B. Miracle, O.N. Senkov, A critical review of high entropy alloys and related concepts, *Acta Mater.* 122 (2017) 448–511. <https://doi.org/10.1016/j.actamat.2016.08.081>.
- [3] A. Takeuchi, A. Inoue, Mixing enthalpy of liquid phase calculated by miedema's scheme and approximated with sub-regular solution model for assessing forming ability of amorphous and glassy alloys, *Intermetallics*. 18 (2010) 1779–1789. <https://doi.org/10.1016/j.intermet.2010.06.003>.
- [4] B. Cantor, I.T.H. Chang, P. Knight, A.J.B. Vincent, Microstructural development in equiatomic multicomponent alloys, *Mater. Sci. Eng. A*. 375–377 (2004) 213–218. <https://doi.org/https://doi.org/10.1016/j.msea.2003.10.257>.
- [5] Z. Wu, H. Bei, F. Otto, G.M. Pharr, E.P. George, Recovery, recrystallization, grain growth and phase stability of a family of FCC-structured multi-component equiatomic solid solution alloys, *Intermetallics*. 46 (2014) 131–140. <https://doi.org/https://doi.org/10.1016/j.intermet.2013.10.024>.
- [6] Z. Wu, H. Bei, G.M. Pharr, E.P. George, Temperature dependence of the mechanical properties of equiatomic solid solution alloys with face-centered cubic crystal structures, *Acta Mater.* 81 (2014) 428–441. <https://doi.org/https://doi.org/10.1016/j.actamat.2014.08.026>.
- [7] B. Gludovatz, A. Hohenwarter, D. Catoor, E.H. Chang, E.P. George, R.O. Ritchie, A fracture-resistant high-entropy alloy for cryogenic applications, *Science*. 345 (2014) 1153–1158. <https://doi.org/10.1126/science.1254581>.

- [8] B. Gludovatz, A. Hohenwarter, K.V.S. Thurston, H. Bei, Z. Wu, E.P. George, R.O. Ritchie, Exceptional damage-tolerance of a medium-entropy alloy CrCoNi at cryogenic temperatures, *Nat. Commun.* 7 (2016) 1–8. <https://doi.org/10.1038/ncomms10602>.
- [9] A.J. Zaddach, C. Niu, C.C. Koch, D.L. Irving, Mechanical Properties and Stacking Fault Energies of NiFeCrCoMn High-Entropy Alloy, *JOM.* 65 (2013) 1780–1789. <https://doi.org/10.1007/s11837-013-0771-4>.
- [10] R.L. Fleischer, Substitutional solution hardening, *Acta Metall.* 11 (1963) 203–209. [https://doi.org/10.1016/0001-6160\(63\)90213-X](https://doi.org/10.1016/0001-6160(63)90213-X).
- [11] R. Labusch, A Statistical Theory of Solid Solution Hardening, *Phys. Status Solidi.* 41 (1970) 659–669. <https://doi.org/10.1002/pssb.19700410221>.
- [12] L.A. Gypen, A. Deruyttere, Multi-component solid solution hardening - Part 1 Proposed model, *J. Mater. Sci.* 12 (1977) 1028–1033. <https://doi.org/10.1007/BF00540987>.
- [13] L.A. Gypen, A. Deruyttere, Multi-component solid solution hardening - Part 2 Agreement with experimental results, *J. Mater. Sci.* 12 (1977) 1034–1038. <https://doi.org/10.1007/BF00540988>.
- [14] I. Toda-Caraballo, P.E.J. Rivera-Díaz-del-Castillo, P.E.J. Rivera-Díaz-Del-Castillo, Modelling solid solution hardening in high entropy alloys, *Acta Mater.* 85 (2015) 14–23. <https://doi.org/10.1016/j.actamat.2014.11.014>.
- [15] C.C. Varvenne, A. Luque, W.A. Curtin, Theory of strengthening in fcc high entropy alloys, *Acta Mater.* 118 (2016) 164–176. <https://doi.org/10.1016/j.actamat.2016.07.040>.
- [16] C. Varvenne, G.P.M.M. Leyson, M. Ghazisaeidi, W.A. Curtin, Solute strengthening in random alloys, *Acta Mater.* 124 (2017) 660–683. <https://doi.org/https://doi.org/10.1016/j.actamat.2016.09.046>.
- [17] N.L. Okamoto, K. Yuge, K. Tanaka, H. Inui, E.P. George, Atomic displacement in the CrMnFeCoNi high-entropy alloy-A scaling factor to predict solid solution strengthening, *AIP Adv.* 6 (2016) 125008. <https://doi.org/10.1063/1.4971371>.
- [18] B.C. De Cooman, Y. Estrin, S.K. Kim, Twinning-induced plasticity (TWIP) steels, *Acta Mater.* 142 (2018) 283–362. <https://doi.org/10.1016/j.actamat.2017.06.046>.
- [19] Z. Li, D. Raabe, Strong and Ductile Non-equiatomic High-Entropy Alloys: Design, Processing, Microstructure, and Mechanical Properties, *JOM.* 69 (2017) 2099–2106. <https://doi.org/10.1007/s11837-017-2540-2>.
- [20] L. Deléhouzée, A. Deruyttere, The stacking fault density in solid solutions based on copper, silver, nickel, aluminium and lead, *Acta Metall.* 15 (1967) 727–734. [https://doi.org/10.1016/0001-6160\(67\)90353-7](https://doi.org/10.1016/0001-6160(67)90353-7).
- [21] D.A. Porter, K.E. Easterling, M.Y. Sherif, Phase transformations in metals and alloys, fourth edi, CRC press, Boca Raton, 2022.
- [22] J.M. Cowley, An approximate theory of order in alloys, *Phys. Rev.* 77 (1950) 669–675. <https://doi.org/10.1103/PhysRev.77.669>.
- [23] A. Marucco, B. Nath, Effects of ordering on the properties of Ni-Cr alloys, *J. Mater. Sci.* 23 (1988) 2107–2114.
- [24] B. Schönfeld, L. Reinhard, G. Kostorz, W. Bührer, Short-Range Order and Atomic Displacements in Ni–20 at.% Cr Single Crystals, *Phys. Status Solidi.* 148 (1988) 457–471. <https://doi.org/10.1002/pssb.2221480203>.

- [25] D.M.C. Nicholson, R.H. Brown, Electrical resistivity of Ni<sub>0.8</sub>Mo<sub>0.2</sub>: Explanation of anomalous behavior in short-range ordered alloys, *Phys. Rev. Lett.* 70 (1993) 3311–3314. <https://doi.org/10.1103/PhysRevLett.70.3311>.
- [26] M.S. Wechsler, R.H. Kernohan, Lattice defects in a copper-aluminum alloy, *Acta Metall.* 7 (1959) 599–607. [https://doi.org/10.1016/0001-6160\(59\)90129-4](https://doi.org/10.1016/0001-6160(59)90129-4).
- [27] R.G. Davies, R.W. Cahn, Short range order in aluminium bronze, *Acta Metall.* 10 (1962) 170–171. [https://doi.org/10.1016/0001-6160\(62\)90062-7](https://doi.org/10.1016/0001-6160(62)90062-7).
- [28] J.B. Cohen, M.E. Fine, Some aspects of short-range order, *J. Phys. Radium.* 23 (1962) 749–762. <https://doi.org/10.1051/jphysrad:019620023010074901i>.
- [29] N. Büttner, E. Nembach, On short-range order hardening in Cu-10 at.% Au, *Acta Metall.* 30 (1982) 83–86. [https://doi.org/10.1016/0001-6160\(82\)90047-5](https://doi.org/10.1016/0001-6160(82)90047-5).
- [30] E. Nembach, H. Riisner, O. Kuhlmann, Order-softening of Cu- 10 at.% Au, *Mater. Sci. Eng. A.* 236 (1997) 234–236.
- [31] Y.S. Kim, W.Y. Maeng, S.S. Kim, Effect of short-range ordering on stress corrosion cracking susceptibility of Alloy 600 studied by electron and neutron diffraction, *Acta Mater.* 83 (2015) 507–515. <https://doi.org/10.1016/j.actamat.2014.10.009>.
- [32] R. Zhang, S. Zhao, J. Ding, Y. Chong, T. Jia, C. Ophus, M. Asta, R.O. Ritchie, A.M. Minor, Short-range order and its impact on the CrCoNi medium-entropy alloy, *Nature.* 581 (2020) 283–287. <https://doi.org/10.1038/s41586-020-2275-z>.
- [33] X. Chen, Q. Wang, Z. Cheng, M. Zhu, H. Zhou, P. Jiang, L. Zhou, Q. Xue, F. Yuan, J. Zhu, X. Wu, E. Ma, Direct observation of chemical short-range order in a medium-entropy alloy, *Nature.* 592 (2021) 712–716. <https://doi.org/10.1038/s41586-021-03428-z>.
- [34] L. Zhou, Q. Wang, J. Wang, X. Chen, P. Jiang, H. Zhou, F. Yuan, X. Wu, Z. Cheng, E. Ma, Atomic-scale evidence of chemical short-range order in CrCoNi medium-entropy alloy, *Acta Mater.* 224 (2022) 16–18. <https://doi.org/10.1016/j.actamat.2021.117490>.
- [35] J. Wang, P. Jiang, F. Yuan, X. Wu, Chemical medium-range order in a medium-entropy alloy, *Nat. Commun.* 13 (2022) 1–6. <https://doi.org/10.1038/s41467-022-28687-w>.

# Chapter 2 Plastic deformation of single crystals of the equiatomic Cr-Co-Ni

## 2.1 Introduction

There is considerable interest in high-entropy alloys (HEAs) and medium-entropy alloys (MEAs), an interest that stems at least partly from their special atomic structures and mechanical properties [1–4]. Early investigations focused on what role, if any, configurational entropy played in stabilizing solid solutions at high temperatures [5,6]. More recently, chemical short-range order, presumably driven by mixing enthalpy, has been a focus, and attempts have been made to elucidate interesting aspects of atomic structure and potential effects on [7–12]. A striking feature of the mechanical properties of certain HEAs and MEAs, especially those with stable or metastable face-centered cubic (FCC) structures, is excellent combination of high strength and high ductility [1–3,13–19]. One contribution to high strength appears to be their severely distorted crystal lattice, which has been tackled *via* different theoretical approaches to obtain correlations between the strength of HEAs and MEAs and appropriate parameters that describe the distorted crystal lattices, including mean-square atomic displacement (MSAD) and lattice mismatch strain [20–23]. High ductility on the other hand has been attributed to deformation twinning, whose propensity is believed to increase with decreasing stacking fault energy, and deformation-induced phase transformations [18,19,24–30]. Together, these results indicate it may be possible to tune lattice distortion and stacking fault energy to attain excellent combination of high strength and high ductility in HEAs and MEAs.

Equiatomic Cr-Co-Ni in the FCC solid-solution state has attracted considerable interest, as it exhibits excellent tensile ductility that increases with decreasing temperature and one of the highest strengths among the quaternary and ternary MEA derivatives of the Cr-Mn-Fe-Co-Ni HEA system [18,19,24–30]. Correspondingly, the MSAD value of Cr-Co-Ni is very large and its high strength is consistent with several different theoretical correlations and predictions [15,20,31,32]. The excellent tensile ductility of Cr-Co-Ni is related to its low stacking-fault energy that results in high propensity for deformation twinning and, in turn, twinning-induced plasticity (TWIP) [25,26,28]. Thin HCP layers have been observed next to deformation twins in the Cr-Co-Ni MEA suggesting that, in addition to TWIP, TRIP (transformation induced plasticity) may also contribute to its excellent tensile ductility as in high-Mn steels and in certain off-equiatomic HEAs [16,17,26,28,33–36]. The theoretically calculated stacking fault energy of the equiatomic Cr-Co-Ni MEA decreases with decrease in temperature, which is *qualitatively* consistent with its experimentally observed increased propensity for twinning and higher tensile ductility at lower [25,30,37,38]. Notwithstanding this, it is very difficult to *quantitatively* compare experimental and theoretical results, as most of the former (including CRSS and twinning stress) are deduced from experiments on polycrystals which usually suffer from grain-size effects.

To the author's knowledge, there are only three studies that used single crystals to investigate the plastic and elastic behavior of equiatomic Cr-Co-Ni [39–41]. In these studies, the CRSS for  $\{111\}\langle 1\bar{1}0\rangle$  slip was determined to be 69-78 and 140-160 MPa respectively at room temperature and 77 K, which are considerably lower than those (117 and 183 MPa) estimated from the polycrystalline yield stresses and the corresponding Taylor factor. The twinning shear stress at room temperature was determined to be  $78 \pm$

5 MPa (comparable to the CRSS for  $\{111\}\langle 1\bar{1}0\rangle$  slip), which is again much smaller than that ( $260 \pm 30$  MPa) estimated from polycrystals [25]. Although the single-crystal data are truly free from grain size effects, the discrepancy with the polycrystalline data seems rather large to be ascribed only to grain size effects. Therefore, additional work with single crystals is needed to deepen our understanding of the mechanical behavior of the equiatomic Cr-Co-Ni MEA.

In the present chapter, the plastic deformation behavior of single crystals of the equiatomic Cr-Co-Ni MEA both in tension and in compression as a function of temperature over a wide range, 14-1373 K, were investigated, in order to experimentally deduce materials parameters (such as CRSS for slip, twinning shear stress as well as stacking fault energy). The results are compared with theoretical estimates.

## 2.2 Materials and methods

Button-shaped ingots of the equiatomic Cr-Co-Ni MEA were prepared from high-purity (>99.9%) Cr, Co and Ni by arc-melting in Ar. All of the ingots were flapped over by 5 time for re-melting to increase the homogeneity and finally combined into rods. Single crystals were grown from the polycrystalline rods with an optical floating-zone furnace in flowing Ar at a growth rate of 10 mm/h. They were then heat-treated at 1473 K for 168 hours, followed by water quenching to suppress, as much as possible, the chemical short-range ordering (SRO) that is expected to develop more significantly at lower temperatures [7,9–12]. Crystallographic orientations of the heat-treated single crystals were determined by the X-ray back reflection Laue method. Oriented specimens with gauge dimensions of  $2 \times 2 \times 5$  mm<sup>3</sup> were prepared by electrical discharge machining for tension and compression, as shown in Fig. 2.1. Specimen surfaces were first polished

mechanically and then electrolytically in a solution of nitric acid and methanol (1:4 by volume) prior to mechanical testing.

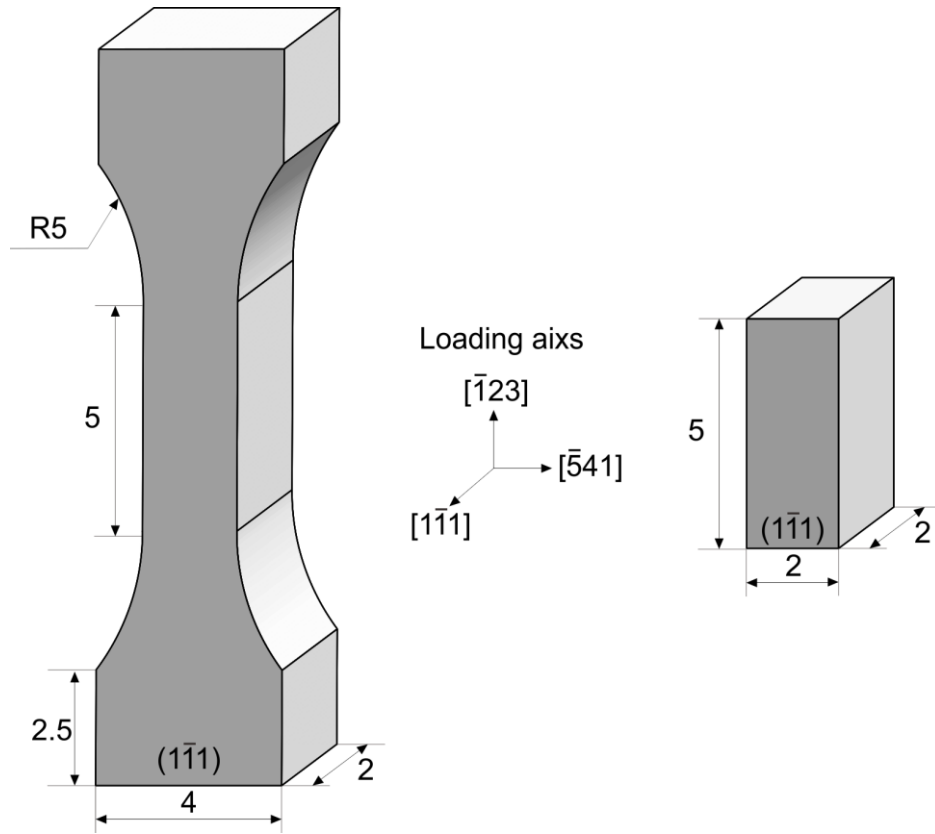


**Fig. 2.1** Schematic illustration of the tensile and compressive specimen.

Compression and tensile tests were conducted along the  $[\bar{1}23]$  loading axis on an Instron-type testing machine in vacuum in the temperature range 14-1373 K at an initial strain rate of  $1 \times 10^{-4} \text{ s}^{-1}$ . The strain-rate sensitivity of flow stress was measured by strain-rate jump tests at selected temperatures below room temperature. Deformation microstructures were examined in an optical microscope (OM) and scanning electron microscope (SEM) equipped with electron back-scatter diffraction (EBSD) and energy dispersive X-ray spectroscopy (EDS) systems. Fine deformation microstructures were examined by transmission electron microscopy (TEM) and scanning transmission electron microscopy (STEM) with JEOL JEM-2000FX, JEM-2100F and JEM-ARM200F

electron microscopes. Thin foils for TEM/STEM observations were prepared by electro-polishing in a solution of nitric acid, ethylene glycol and methanol (2:5:20 by volume).

## 2.3 Results

### 2.3.1 Quality of single crystals

The as-grown single crystals exhibited a featureless microstructure without significant heterogeneity caused by rapid dendritic growth, because of the slow growth rate employed (10 mm/h) and the high thermal gradient at the solid-liquid interface in the optical floating-zone furnace, as shown in Fig. 2.2 (a). The point-to-origin analysis exhibits that the misorientation within the gage section of the specimen is less than  $1^\circ$  (Fig. 2.2 (b)). The chemical composition determined by wet chemistry averaged over 5 different measurements on single crystals quenched from 1473 K is 33.65Cr – 33.22Co – 33.13Ni (at. %), which is close to the nominal equiatomic composition.

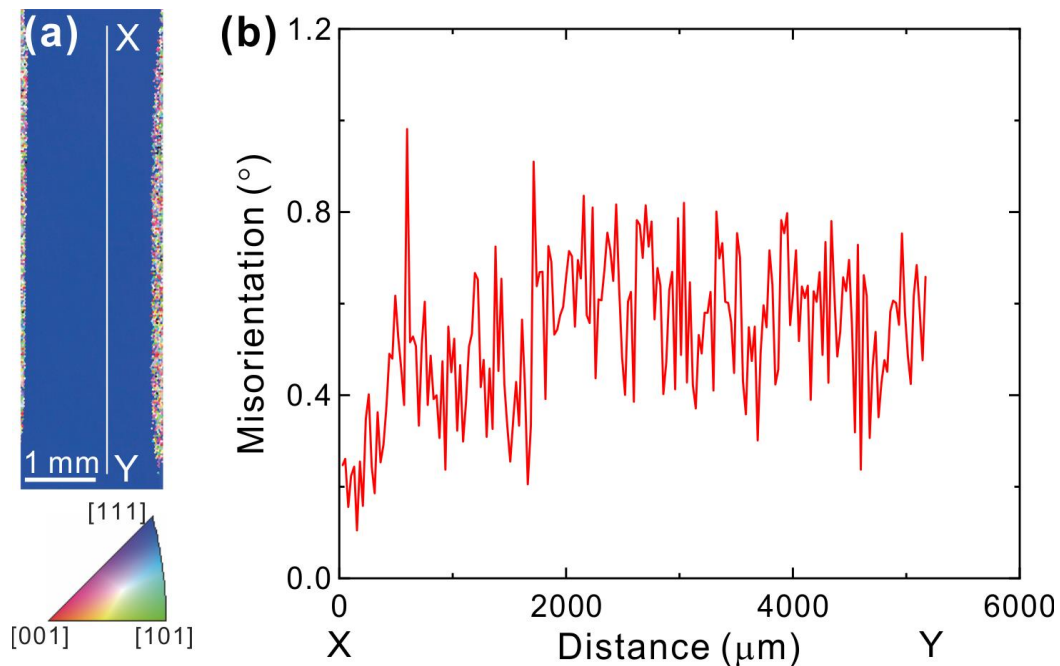


**Fig. 2.2** (a) The EBSD IPF map and (b) the corresponding point-to-origin misorientation analysis of the single crystal specimen of the Cr-Co-Ni.

In the selected-area electron diffraction (SAED) pattern taken along the [111] zone axis of a single crystal water-quenched from 1473 K (Fig. 2.3(a)), some diffuse intensity is observed at positions of  $1/3\{422\}$  (marked with circles in Fig. 2.3(a)) in addition to Bragg spots of the FCC structure. This is similar to what has been observed in single crystals of the Cr-Mn-Fe-Co-Ni quinary equiatomic high-entropy alloy (Fig. 2.3(b) [42–44]) and is indicative of local fluctuation in interatomic distances accompanied by static displacement of the constituent elements due to their atomic radius differences and/or chemical short-range quenching from 1473 K cannot be precisely determined from such SAED patterns and requires further investigation considering the fact that the difference in atomic scattering factor among Cr, Co and Ni is virtually negligible and therefore, it is technically impossible to detect any kind of atomic ordering formed with Cr, Co and Ni simply by SAED. The evolution of diffuse intensity at positions of  $1/3\{422\}$  with annealing and its effects on yield strength are part of a follow-on study that will be described in Chapter 3 of this work.

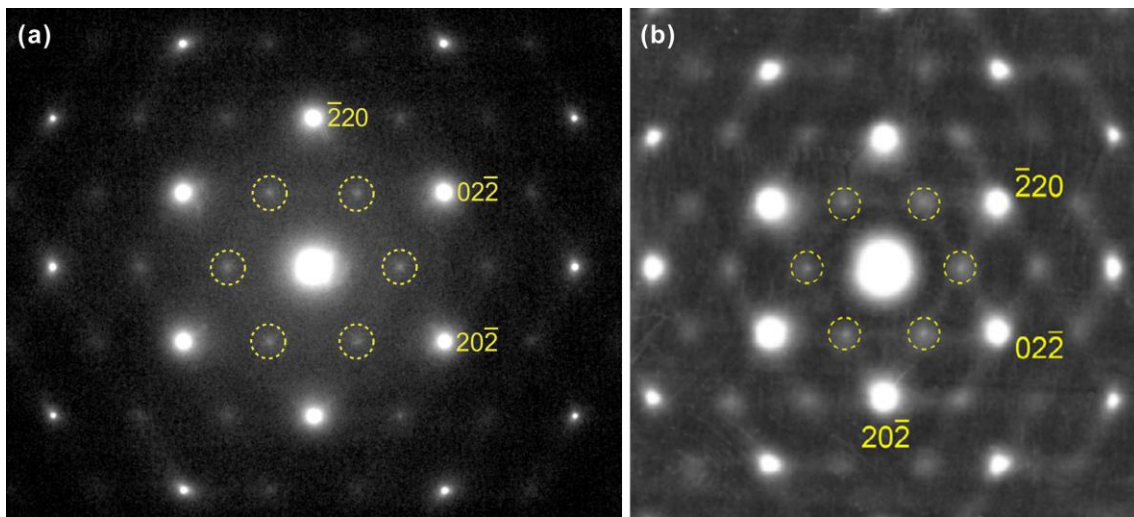


**Fig. 2.3** SAED patterns with the [111] incidence obtained from the single crystal of the equiatomic (a) Cr-Co-Ni and (b) Cr-Mn-Fe-Co-Ni water quenched from 1473 K [42]. Diffuse intensities at positions of  $1/3\{422\}$  are marked with circles.

## 2.3.2 Compressive deformation

### 2.3.2.1 Stress-strain behavior

Typical compressive stress-strain curves are shown in Fig. 2.4. All compression tests began at a strain rate of  $1 \times 10^{-4} \text{ s}^{-1}$  to determine the yield stress. Above room temperature, straining was continued at this rate but, at room temperature and below, strain-rate jump tests were performed within the strain range of 'easy glide' (stage I) to minimize effects of work hardening on the strain-rate sensitivity measurements.

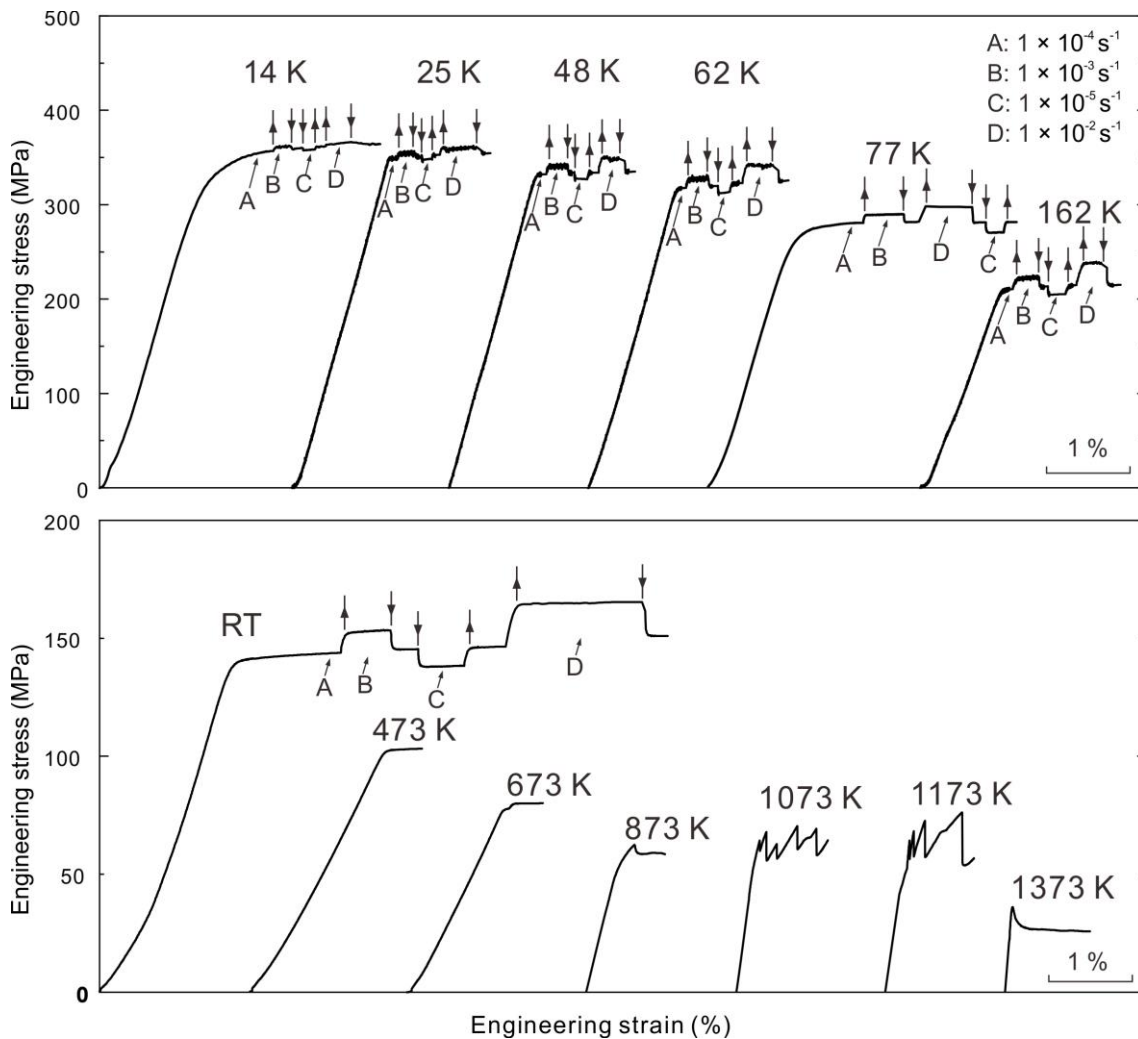


**Fig. 2.4** Stress-strain curves obtained for  $[\bar{1}23]$ -oriented single crystals deformed in compression. Compression tests were usually started at a strain rate of  $1 \times 10^{-4} \text{ s}^{-1}$  to determine the yield stress and then strain-rate sensitivity were measured by strain-rate jump tests (at room temperature and below).

At all tested temperatures, only  $(111) [\bar{1}01]$  slip occurred in stage I with no deformation twinning, as confirmed by examination in OM, SEM and TEM. Deformation markings are very straight, in particular at lower temperatures, traversing from one surface to another (examples at 77 K, 212 K and room temperature are shown in (Fig. 2.5) and they gradually cover the gauge section as the plastic strain increases until it is filled with these straight  $(111)$  slip lines at the end of stage I, which extends to more than 20% plastic strain at room temperature (as can be seen in the tensile stress-strain curve of Fig. 2.9, which will be discussed later).

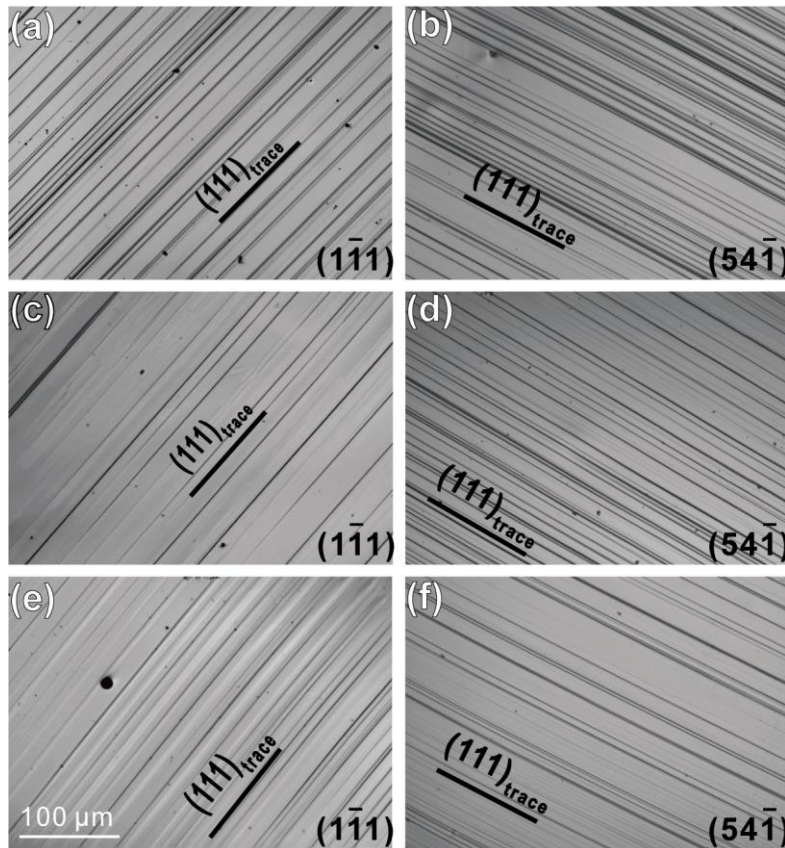


**Fig. 2.5** Deformation markings observed on two orthogonal side surfaces ((a,c,e)  $(1\bar{1}\bar{1})$  and (b,d,f)  $(54\bar{1})$ ) of  $[\bar{1}23]$ -oriented single crystals deformed in compression at (a,b) 77 K, (c, d) 212 K and (e, f) room temperature.

From tests such as those described above, the 0.2% offset yield stress was determined and the Schmid factor of 0.467 was then used to calculate the CRSS for (111)  $[\bar{1}01]$  slip whose temperature dependence is plotted in Fig. 2.6. For comparison, the previous results for the quinary equiatomic Cr-Mn-Fe-Co-Ni HEA single crystals [42] and two Cu-Al binary alloys [45] are also shown.

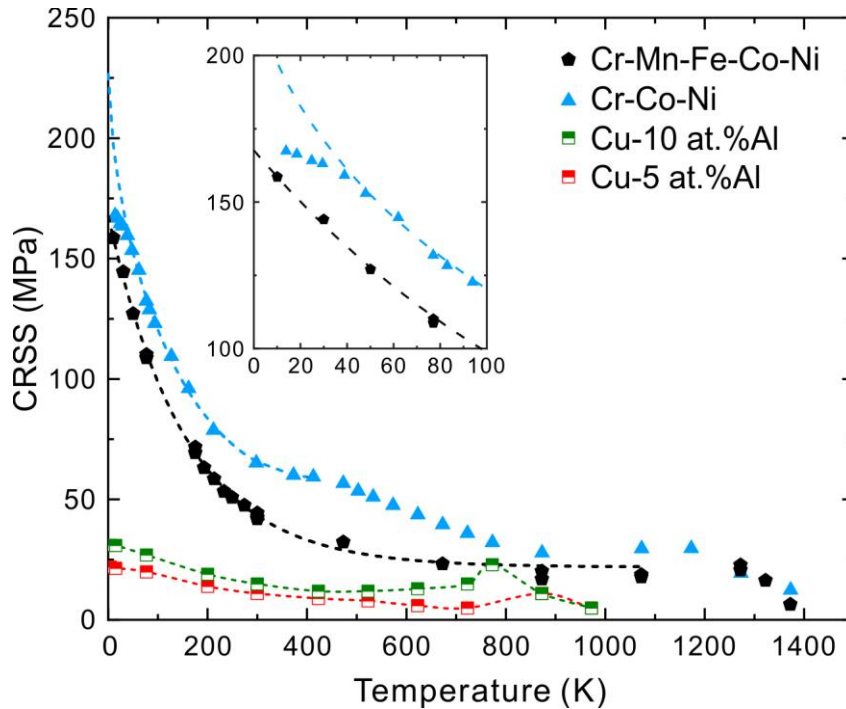


**Fig. 2.6** Temperature dependence of CRSS for (111) $[\bar{1}01]$  slip in the equiatomic Cr-Co-Ni MEA. Data for the equiatomic Cr-Mn-Fe-Co-Ni HEA and Cu-Al binary alloys are shown for comparison.

The CRSS increases rapidly as the temperature is decreased below room temperature, as observed in many conventional FCC solid-solution alloys and FCC HEAs. However, three characteristic behaviors of the present MEA are worth noting. Firstly, a dulling of the temperature dependence of CRSS below 50 K is observed in equiatomic Cr-Co-Ni, which can be seen more clearly in the magnified view shown in the inset of Fig. 2.6. While this has long been known to occur in some conventional FCC alloys (such as Cu alloys with Al, Ni or Ge) below 77 K through the so-called dislocation inertia effect [47],

it was not evident in the earlier study of the equiatomic Cr-Mn-Fe-Co-Ni HEA down to 10 K [42]. However, Tirunilai et al. [47] recently reported a plateau in the yield stress-temperature curve for Cr-Mn-Fe-Co-Ni polycrystals below 15 K. Therefore, more detailed study of the inertia effect in the quinary equiatomic Cr-Mn-Fe-Co-Ni HEA is needed. Secondly, an inflection in the CRSS-temperature curve of the equiatomic Cr-Co-Ni MEA is clearly observed at around 473 K. A close look at the temperature dependence of CRSS of the equiatomic Cr-Mn-Fe-Co-Ni HEA suggests a similar inflection may be present in that alloy also, but the paucity of data in the relevant temperature range precludes a definitive assessment. The reason for the inflection is not clear yet, but we suspect it may be related to the motion of quenched-in vacancies from the 1473 K heat treatment because the inflection temperature of 473 K is also the onset temperature for migration of vacancies introduced by electron irradiation in HEAs and MEAs in the Cr-Mn-Fe-Co-Ni system (Sugita et al. [48]). Finally, there is a slight increase of the CRSS of the equiatomic Cr-Co-Ni MEA above 1073 K, where serrated flow is observed in the stress-strain curves (Fig. 2.4). This was also observed in the equiatomic Cr-Mn-Fe-Co-Ni HEA [42]. Based on the strain-rate and temperature sensitivity of flow stress (including the extent of serration), the serrated flow has been interpreted to be caused by the interaction between solute atoms (which in the case of equiatomic alloys are simply one of the constituent elements) and dislocations (more specifically, extended dislocations bounding a stacking fault), a phenomenon referred to as the Portevin-Le Chatelier (PLC) effect, as discussed in the previous work on single crystals of the equiatomic Cr-Mn-Fe-Co-Ni HEA [42] and also in a paper on polycrystals of various MEA and HEA [49].

The CRSSs are considerably higher for the ternary equiatomic Cr-Co-Ni MEA (65 and 130 MPa) than for the quinary equiatomic Cr-Mn-Fe-Co-Ni HEA (44 and 113 MPa)

[42] at room temperature and 77 K, respectively. These CRSS values of the equiatomic Cr-Co-Ni MEA are comparable to that reported by Uzer et al. [41] at room temperature (69 MPa) but are considerably lower than those reported by Abuzaid and Patriarca [41] at room temperature (78 MPa) and at 77 K (140-160 MPa). The CRSS value at 0 K for the equiatomic Cr-Co-Ni MEA is estimated to be 225 MPa by extrapolating the CRSS-temperature curve down to 0 K (excluding the data points below 50 K in the anomalous temperature range that are influenced by the inertia effect). The 0 K CRSS value thus estimated is comparable to that (215 MPa) estimated from polycrystals of the equiatomic Cr-Co-Ni MEA [20,32]. The 0 K CRSS value of the equiatomic Cr-Co-Ni MEA is considerably larger than that (168 MPa) of the equiatomic Cr-Mn-Fe-Co-Ni HEA [42]. This is consistent with experimental data on polycrystals [32] as well as the prediction for the 0 K CRSS from the values of mean-square atom displacement [20].

### **2.3.2.2 Strain rate sensitivity of flow stress**

The strain-rate sensitivity of flow stress in the strain range of easy glide is plotted in Fig. 2.7(a). In this figure, the plotted shear stress and shear strain were converted from axial stress and strain assuming single  $(111)[\bar{1}01]$  slip. In stage I, the flow stress at fixed strain rate and temperature does not depend significantly on strain. A clearer view of the extent of the strain-rate sensitivity of flow stress shown in Fig. 2.7(a) can be obtained by evaluating its gradient as a function of temperature, which is shown in Fig. 2.7(b). Since the flow stress of the equiatomic Cr-Co-Ni MEA increases with strain rate, the strain-rate sensitivity of flow stress increases with decreasing temperature down to 62 K (because of the more significant temperature dependence of CRSS), below which the strain-rate

sensitivity of flow stress becomes smaller as the temperature is decreased as shown in

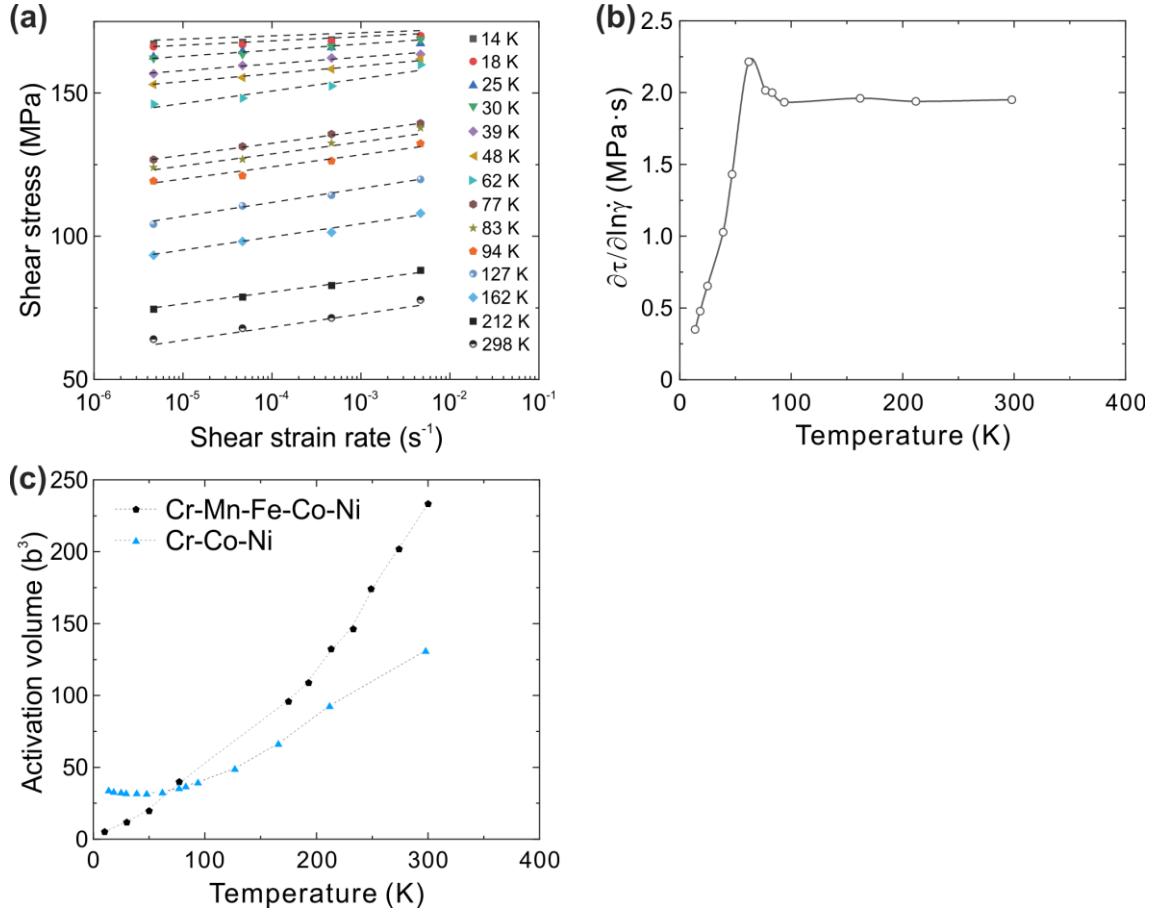


**Fig. 2.7** (a) The strain-rate sensitivity of flow stress measured for  $[\bar{1}23]$ -oriented single crystals of the equiatomic Cr-Co-Ni MEA. (b) The gradient of the strain-rate sensitivity shown in (a) plotted as a function of temperature. (c) Temperature dependence of activation volume for deformation in the equiatomic Cr-Co-Ni MEA, together with data for the equiatomic Cr-Mn-Fe-Co-Ni HEA for comparison [42].

Fig. 2.7(b). The decrease observed below 62 K is clear evidence for the inertia effect [46], which is responsible for the duller temperature dependence of CRSS (Fig. 2.4).

Fig. 2.7(c) plots the temperature dependence of the activation volume ( $V$ ) estimated using the following conventional equation:

$$V = kT \left[ \frac{\partial \ln \dot{\gamma}}{\partial \tau} \right]_T \quad (2-1)$$

where  $k$  is the Boltzmann constant,  $T$  is the absolute temperature,  $\dot{\gamma}$  is the shear strain rate, and  $\tau$  is the shear stress. For comparison, values of the activation volume similarly determined for single crystals of the equiatomic Cr-Mn-Fe-Co-Ni HEA [42] are also plotted in Fig. 2.7(c). The activation volume of the equiatomic Cr-Co-Ni MEA is less temperature dependent than that of the equiatomic Cr-Mn-Fe-Co-Ni HEA. Additionally, while the activation volume at room temperature is much smaller for Cr-Co-Ni ( $\sim 130 b^3$ ) than for Cr-Mn-Fe-Co-Ni ( $\sim 233 b^3$ ), it is inverse at 14 K ( $\sim 34 b^3$  for the Cr-Co-Ni and  $\sim 5 b^3$  for Cr-Mn-Fe-Co-Ni). Of interest to note in Fig. 2.7(c) is that the activation volume of the Cr-Co-Ni MEA increases slightly with decreasing temperature below 50 K, which is consistent with the inertia effect occurring in that temperature range. The activation volumes at 77 K and room temperature ( $\sim 36$  and  $\sim 130 b^3$ , respectively) obtained for Cr-Co-Ni in the present study are considerably larger than those ( $\sim 14$  and  $\sim 47 b^3$ ) reported for polycrystals of the same alloy by [51]. The reason for the discrepancy remains to be clarified.

### 2.3.2.3 Dislocation structures

A typical dislocation structure observed after room-temperature compression to about 3% plastic strain is shown in Fig. 2.8(a). Planar arrays of dislocations were observed in the TEM foil extracted parallel to the (111) primary slip plane; no cell structures were observed. These observations are consistent with the alloy being a single crystal as well as its low stacking fault energy. Widely dissociated, coupled partial-dislocations were clearly visible in weak-beam TEM images (see example in Fig. 2.8(b)). From the separation distances measured as a function of angle ( $\theta$ ) between the Burgers vector and

line direction of dislocations, the stacking fault energy is  $14 \pm 3$  mJ/m<sup>2</sup> (Fig. 2.8(c)).

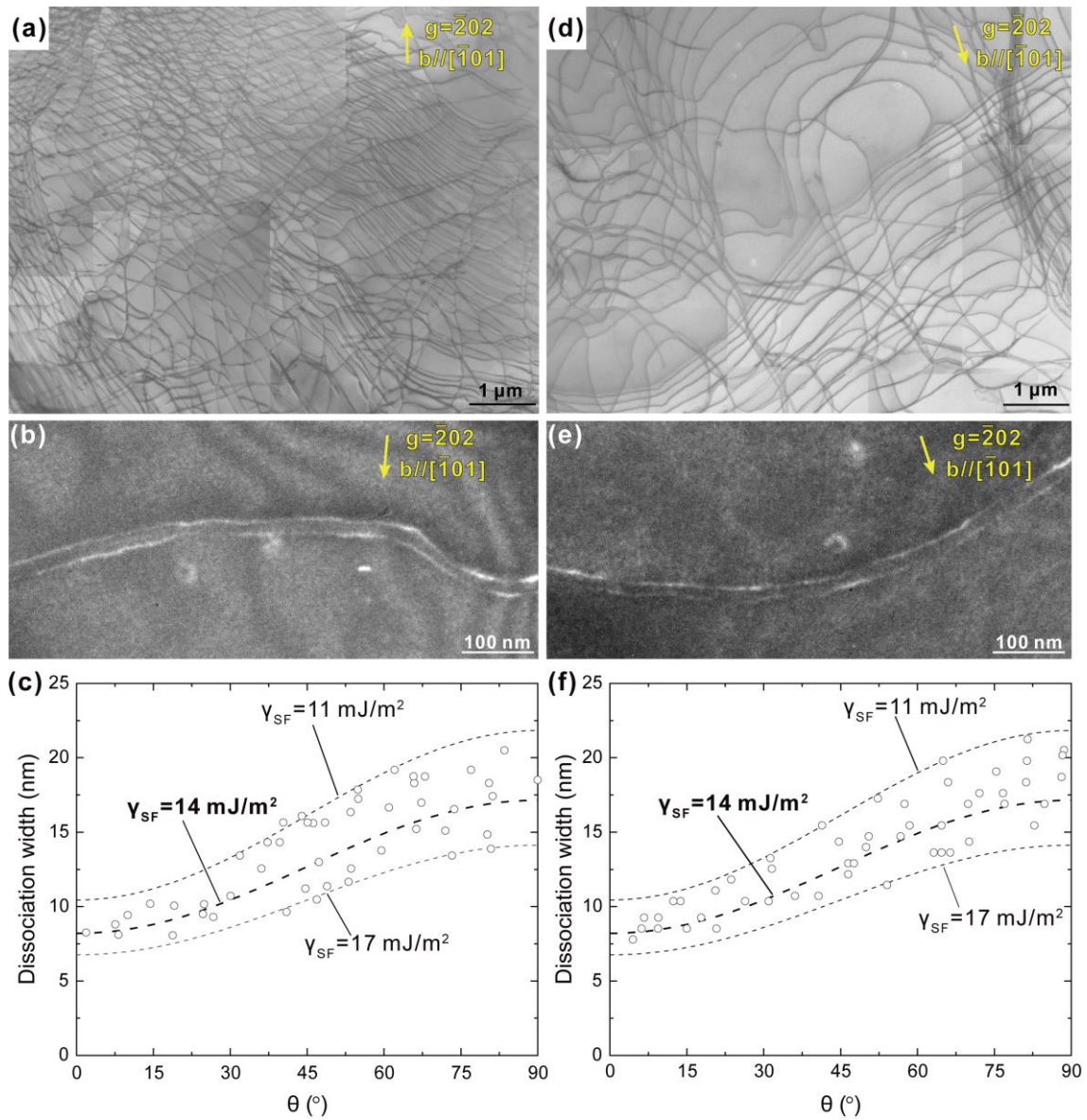


**Fig. 2.8** Typical dislocation structures observed in a  $[\bar{1}23]$ -oriented single crystal of the equiatomic Cr-Co-Ni MEA deformed in compression to about 3% plastic strain at (a) room temperature and (d) 77 K. Weak-beam image of a widely separated partial dislocations in specimens deformed at (b) room temperature and (e) 77 K. Dissociation widths of partials plotted as a function of angle between the Burgers vector of  $1/2[\bar{1}01]$  and dislocation line are shown in (c) and (f) for room temperature and 77 K, respectively.

Scatter in dissociation widths at a given  $\theta$  in the present equiatomic Cr-Co-Ni MEA is similar in magnitude to those in pure metals such as pure Cu and Ag [52,53] and in the

equiatomic Cr-Mn-Fe-Co-Ni HEA [42,43]. No significant local variation in dissociation widths was observed in the present equiatomic Cr-Co-Ni MEA, in contrast to what has been reported elsewhere [28,54]. The value of stacking fault energy ( $14 \pm 3 \text{ mJ/m}^2$ ) obtained in the present study of equiatomic Cr-Co-Ni is considerably smaller than that ( $30 \text{ mJ/m}^2$ ) obtained previously for equiatomic Cr-Mn-Fe-Co-Ni [42,43], is also a bit smaller than those determined from polycrystals of equiatomic Cr-Co-Ni ( $22 \pm 4 \text{ mJ/m}^2$  in [25] and  $18 \pm 4 \text{ mJ/m}^2$  in [55] and is in good agreement with that ( $10 - 20 \text{ mJ/m}^2$ ) obtained for polycrystalline Cr-Co-Ni [56]. Of interest to note is that a very low stacking fault energy of  $8.18 \pm 1.43 \text{ mJ/m}^2$  has been reported by Zhang et al. [12] for a specimen quenched from 1473 K, which is exactly the same quenching procedure employed in the present study. In their paper, Zhang et al. [12] also mentioned that the stacking fault energy of the equiatomic Cr-Co-Ni alloy increases when annealed at lower temperatures accompanied by an increase in the extent of short-range ordering.

Typical dislocation structure observed at room temperature in a TEM foil extracted parallel to the (111) primary slip plane of a bulk specimen pre-compressed at 77 K to about 3% plastic strain is shown in Fig. 2.8(d). Dislocation arrays are again very planar without the formation of dislocation cells. Consistent with this, dislocations are observed clearly to dissociate into two Shockley partials (Fig. 2.8(e)). Stacking fault energies were estimated from the dislocation dissociation widths, as described above, to evaluate the temperature dependence of stacking fault energy and compare with theoretical calculations [30,37,38]. However, the estimated stacking fault energy for the specimen deformed at 77 K is  $14 \pm 3 \text{ mJ/m}^2$  (Fig. 2.8(f)), which is virtually the same as that obtained from the specimen deformed at room temperature (Fig. 2.8(c)). This suggests that, regardless of the deformation temperature, the dislocation dissociation width settles at the

room-temperature equilibrium value as long as TEM observations are made at room temperature. In-situ measurements of the dissociation width are therefore needed to explore the temperature dependent stacking fault energy of the equiatomic Cr-Co-Ni MEA.

### 2.3.3 Tensile deformation

#### 2.3.3.1 Stress-strain behavior

Stress-strain curves of the Cr-Co-Ni single crystals tested a constant engineering strain rate of  $1 \times 10^{-4} \text{ s}^{-1}$  at room temperature and 77 K are shown in Fig. 2.9(a). Stage I (strain range of easy glide) is considerably longer for the ternary equiatomic Cr-Co-Ni MEA than for the quinary equiatomic Cr-Mn-Fe-Co-Ni HEA both at room temperature and 77 K, consistent with the considerably lower stacking fault energy of the former.

At room temperature, stage I extends to about 25% plastic strain, which is much larger than the 13% strain of the Cr-Mn-Fe-Co-Ni HEA [42]. This is consistent with the general belief that stage I is longer in FCC alloys with lower stacking fault energy [57]. The long stage I is followed by stage II with a high work-hardening rate of about  $G/390$  ( $G$ : shear modulus), which is well within the range of many conventional FCC alloys. Similar to what is observed in stage I, plastic deformation in Stage II also occurs essentially by  $(111)[\bar{1}01]$  primary slip, although deformation markings corresponding to the  $(\bar{1}\bar{1}1)[011]$  conjugate slip system are also sporadically observed. The room-temperature CRSS in tension is 62 MPa, which agrees well with that ( $65 \pm 5$  MPa) obtained in compression at room temperature (see earlier section). These results confirm the lack of any significant tension-compression asymmetry in yield stress, which implies ‘normal’ behavior of dislocations. Interestingly, stage II is followed by a large region of

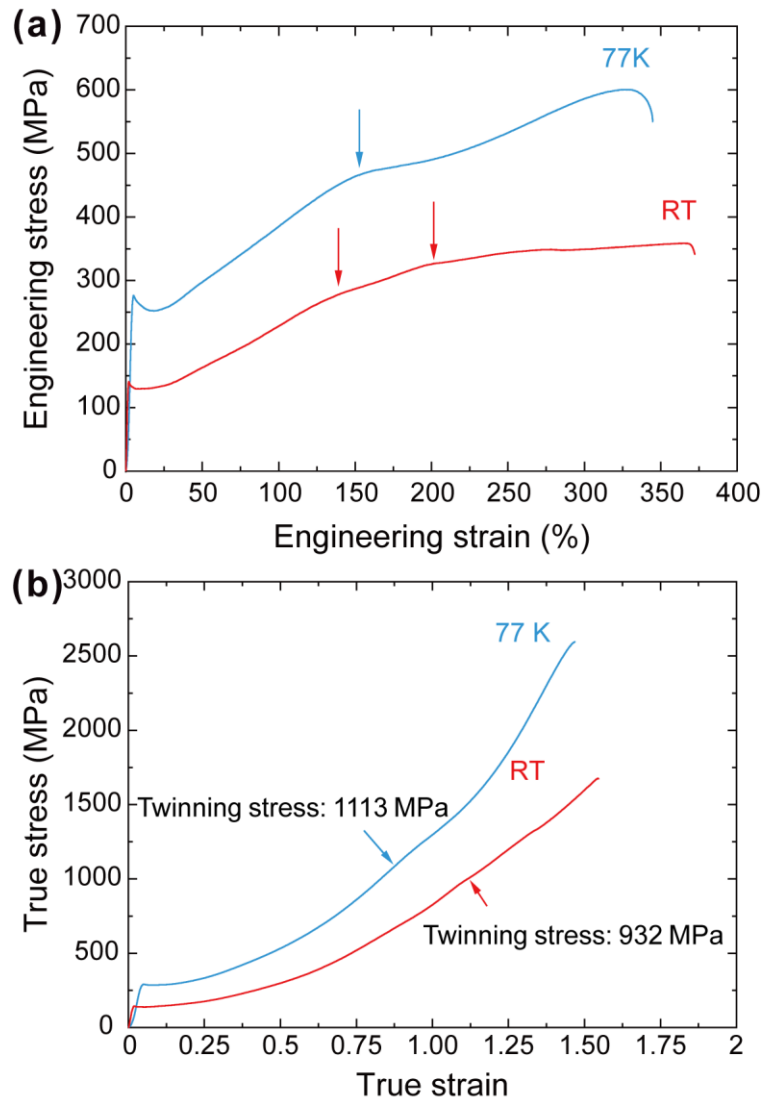


**Fig.2.9** (a) Engineering stress-engineering strain curves and (b) true stress-true strain curves obtained for  $[\bar{1}23]$ -oriented single crystals of the equiatomic Cr-Co-Ni MEA deformed in tension to failure at 77 K and room temperature.

flow accompanied by two inflection points (red arrows) before failure eventually occurs. This is in contrast to the room-temperature tensile deformation behavior of single crystals of the quinary equiatomic Cr-Mn-Fe-Co-Ni HEA, in which failure occurs at the end of stage II [42].

To identify physical origins of the two inflection points in the stress-strain curves, a room-temperature tensile test was interrupted repeatedly at points A-E in Fig. 2.10(a) so

that the evolution of microstructure could be examined by OM (Fig. 2.10(b)) and SEM with EBSD (Fig. 2.10(c)). The first inflection point, marked by the arrow between points B and C in Fig. 2.10(a) and corresponding to a sudden change in work-hardening rate at a strain of about 140%, was confirmed to be due to the change of the dominant slip system from the  $(111)[\bar{1}01]$  primary slip system to the  $(\bar{1}\bar{1}1)[011]$  conjugate slip system. Therefore, the first inflection point corresponds to the end of overshoot of the rotation of the tensile axis toward  $[\bar{1}01]$ . The tensile-axis orientation at this point was determined to be  $[\bar{5}49]$  (Fig. 2.10(d)). After the first inflection point,  $(\bar{1}\bar{1}1)[011]$  conjugate slip occurs in the form of Lüders band, as seen in the low- magnification SEM/EBSD image corresponding to point C, Fig. 2.10(c). The Lüders front propagates from the top of the gauge section to the bottom until the whole gauge section is fully covered with deformation markings of the conjugate slip at the second inflection point (marked by arrow between points D and E in Fig. 2.10(a)). In the quinary equiatomic Cr-Mn-Fe-Co-Ni HEA with the  $[\bar{1}23]$  orientation, conjugate twinning is observed to occur at 77 K in the form of Lüders band after stage II dominated by primary slip [42]. Although the Lüders band appears similarly on the conjugate system in equiatomic Cr-Co-Ni at room temperature, twinning is not involved in the deformation after the first inflection point, as is evident from Fig. 2.10(c) which shows SEM/EBSD images at points C and D (prior to the second inflection point). The orientation difference of 60 degrees between the matrix and twin is clear in Fig. 2.10(e) for the E3 region of the SEM/EBSD image in Fig. 2.10(c). The second inflection point at a strain of about 200% after point D was confirmed to

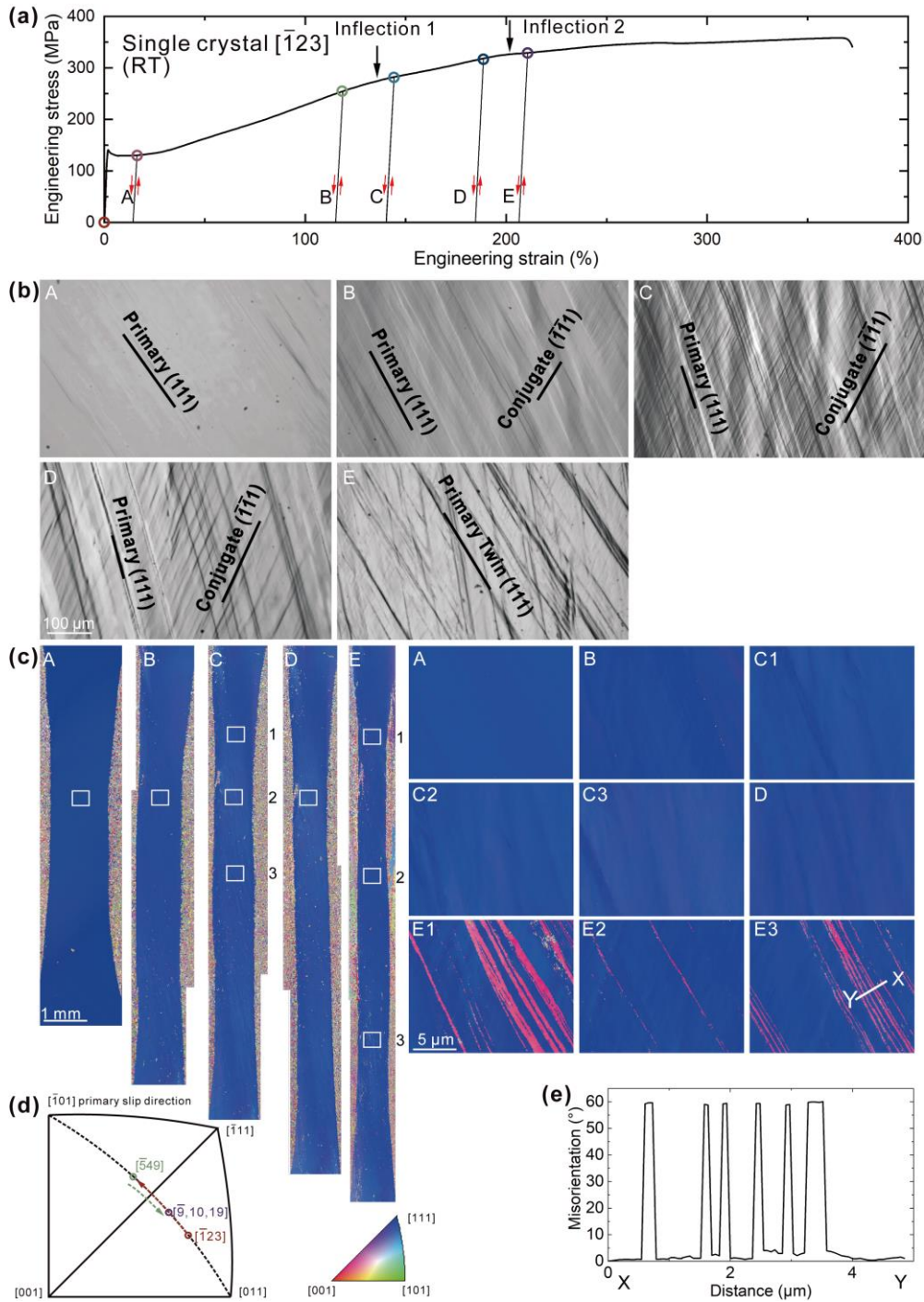


**Fig. 2.10** (a) Stress-strain curve of a  $[\bar{1}23]$ -oriented single crystal of the equiatomic Cr-Co-Ni MEA deformed in tension at room temperature, showing the points A-E at which the test was interrupted for microstructure observations. (b) Microstructures observed by optical microscopy at points A-E on the  $(1\bar{1}1)$  surface. (c) EBSD orientation maps at points A-E with the framed areas shown enlarged on the right-hand side. (d) Tensile-axis rotation during deformation shown in the stereographic projection. (e) Misorientation along the line X - Y in the EBSD map of E3, showing the existence of deformation twins.

correspond to the change of the dominant deformation mode from  $(\bar{1}\bar{1}1)[011]$  conjugate slip to  $(111)[\bar{2}11]$  primary twinning, as clearly seen in the SEM/EBSD images of point E in Fig. 2.10(c). The second inflection point corresponds to the end of overshoot of the tensile axis back toward  $[011]$  in the original standard triangle by the conjugate slip system; the tensile-axis orientation at this point was determined to be  $[\bar{9} 10 19]$  (Fig. 2.10(d)). Primary twinning after the second inflection point occurs uniformly throughout the whole gauge length (SEM/EBSD images of E1-E3 of Fig. 2.10(c)) rather than in the form of Lüders band as in the case of conjugate twinning in the quinary equiatomic Cr-Mn-Fe-Co-Ni HEA at 77 K [42]. Of interest to note in Fig. 2.10(a) is that strain to failure at room temperature is significantly higher for equiatomic Cr-Co-Ni (370%) than for equiatomic Cr-Mn-Fe-Co-Ni (110%) [42]. In view of the fact that twinning does not occur in the latter at room temperature [42], the activation of twinning in the former seems to be responsible for its enhanced room-temperature tensile ductility.

At 77 K, the CRSS in tension increases significantly to 131 MPa, from 65 MPa at room temperature. The CRSS at 77 K coincides well with that ( $133 \pm 6$  MPa) obtained in compression at 77 K (see earlier section), confirming once again the absence of any significant tension-compression asymmetry in yield stress. The CRSS value at 77 K obtained in the present study is somewhat lower than that (140-160 MPa) obtained in tension by Abuzaid and Patriarca [50]. Stage I (easy glide) with low work-hardening rate occurs up to more than 22% plastic strain, which is larger than that (17%) of the equiatomic Cr-Mn-Fe-Co-Ni HEA at 77 K [42]. The work-hardening rate for Stage II at 77 K is  $G/344$ , which is similar to the value at room temperature.

There is an inflection point in the 77 K tensile stress-strain curve after a large plastic strain of about 150% in stage II. This inflection point was confirmed to correspond to the onset of deformation twinning through repeated microstructure observations during interrupted tests, as shown in Fig. 2.11 and corresponding to points A-C in Fig. 2.11(a). Deformation microstructures examined by OM and SEM with EBSD are summarized in Fig. 2.11(b) and 2.11(c), respectively. The  $(111)[\bar{1}01]$  primary slip system dominates during stage I and stage II with the  $(\bar{1}\bar{1}1)[011]$  conjugate slip system occurring only sporadically up to the inflection point at a strain of about 150%. No evidence for deformation twinning is detected up to point B. Beyond the inflection point, deformation markings of twinning on the conjugate plane can be seen, as shown in the SEM/EBSD images of point C in Fig. 2.11(c). The orientation difference of 60 degrees between the matrix and twin is clearly detected in Fig. 2.11(e) for the C2 region of the SEM/EBSD image in Fig. 2.11(c). As seen in the low-magnification SEM/EBSD images of point C, Fig. 2.11(c), conjugate twinning after the inflection point occurs in the form of Lüders band with its front propagating from the bottom of the gauge section to the top until the whole gauge section is covered with the deformation markings of the conjugate twinning. The inflection point at a strain of about 150% was thus confirmed to correspond to the change of the dominant deformation mode from  $(111)[\bar{1}01]$  primary slip to  $(\bar{1}\bar{1}1)[\bar{1}21]$  conjugate twinning. This is exactly the same as what was previously observed in similarly oriented single crystals of the quinary equiatomic Cr-Mn-Fe-Co-Ni HEA tested at 77 K [42]. Thus, the inflection point corresponds to the end of overshoot of the tensile axis toward  $[\bar{1}01]$ . The tensile-axis orientation at this point was determined to be  $[\bar{1}\bar{2} \ 9 \ 21]$  (Fig. 2.11(d)). The extent of overshoot of the tensile axis is larger at 77 K ( $4.7^\circ$ ) than at

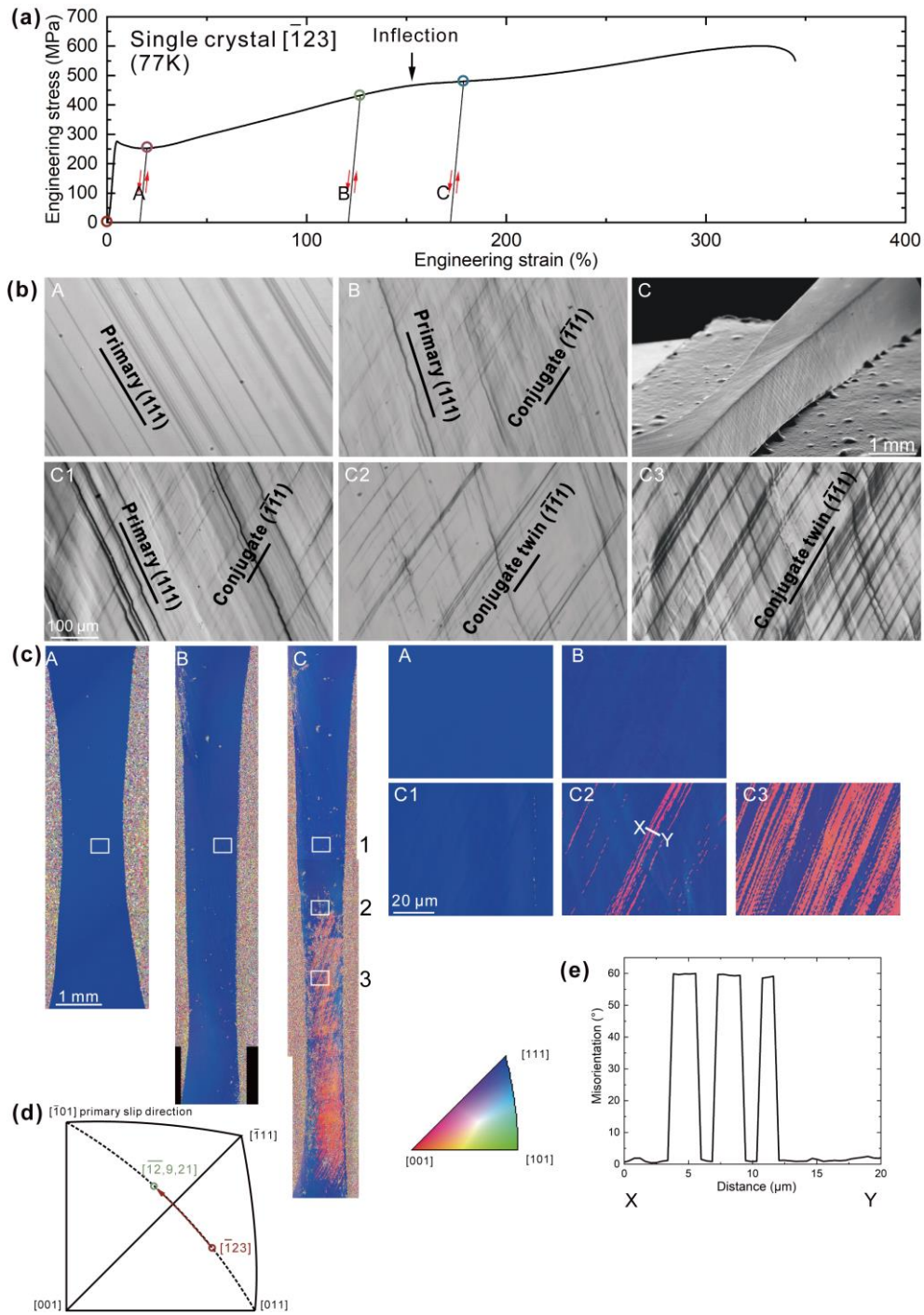


**Fig. 2.11** (a) Stress-strain curve of a  $[\bar{1}23]$ -oriented single crystal of the equiatomic Cr-Co-Ni MEA deformed in tension at 77 K, showing the points A-C at which the test was interrupted for microstructure observations. (b) Microstructures observed by optical microscopy at points A-C on the  $(1\bar{1}1)$  surface. (c) EBSD orientation maps at points A-C with the framed areas shown enlarged on the right-hand side. (d) Tensile-axis rotation during deformation shown in the stereographic projection. (e) Misorientation along the line X - Y in the EBSD map of C2, showing the existence of deformation twins.

room temperature (3.7°) for the ternary equiatomic Cr-Co-Ni MEA and also larger than that for the quinary equiatomic Cr-Mn-Fe-Co-Ni HEA at 77 K (3.7°) [42]. All these observations are consistent with the general belief that the extent of overshoot of the tensile axis is larger for materials with lower stacking fault energies. Of interest to note in Fig. 2.9(a) is that the tensile elongation to failure of equiatomic Cr-Co-Ni is larger at room temperature than at 77 K. While this may be related to the lower strength at room temperature compared to that at 77 K combined with the occurrence of deformation twinning at both temperatures in Cr-Co-Ni, it is opposite to what is observed not only for polycrystals of the equiatomic Cr-Co-Ni MEA [25,32] but also for  $[\bar{1}23]$ -oriented single crystals of the equiatomic Cr-Mn-Fe-Co-Ni HEA [42].

Tensile true stress-true strain curves at room temperature and 77 K were obtained from the engineering stress-engineering strain curves (Fig. 2.9(a)) using standard equations assuming uniform plastic deformation for the entire stage as a first approximation and are shown in Fig. 2.9(b) [42]. This was done to deduce the twinning shear stress for the equiatomic Cr-Co-Ni MEA at room temperature and 77 K, by properly taking into account the considerably reduced cross-section of the specimen when deformation twinning commences after a large amount of plastic strain. Although the Lüders deformation by the conjugate slip was observed at room temperature, the true stress value for the onset of deformation twinning at room temperature is not considered to be affected much by the non-uniform variation of cross section because the Lüders band was confirmed to sweep over the entire gauge section in prior to the second inflection point corresponding to the onset of deformation twinning. The true stress for onset of deformation twinning at room temperature is determined to be 932 MPa (Fig. S2.1(a,c)), which can be converted into a twinning shear stress of 381 MPa with the

Schmid factor (0.409) for  $(111)[\bar{2}11]$  primary twinning at the  $[\bar{9} 10 19]$  tensile-axis orientation. The above twinning shear stress is considerably larger than the previously reported value ( $78 \pm 5$  MPa for  $[110]$ -,  $[111]$ - and  $[123]$ -oriented single crystals of equiatomic Cr-Co-Ni) by Uzer et al. [41]. They claimed that nano-twinning was observed at 4% strain for  $[110]$ -oriented crystals and at 10% strain for  $[123]$ -oriented crystals in tension at room temperature. However, these strain levels are well within stage I where single glide of the primary slip system dominates. Similarly, the twinning shear stress of 482 MPa is obtained from the onset true stress for deformation twinning at 77 K (1113 MPa, Fig. S2.1(b,d)) and the Schmid factor (0.433) for  $(\bar{1}\bar{1}1)[\bar{1}21]$  conjugate twinning at

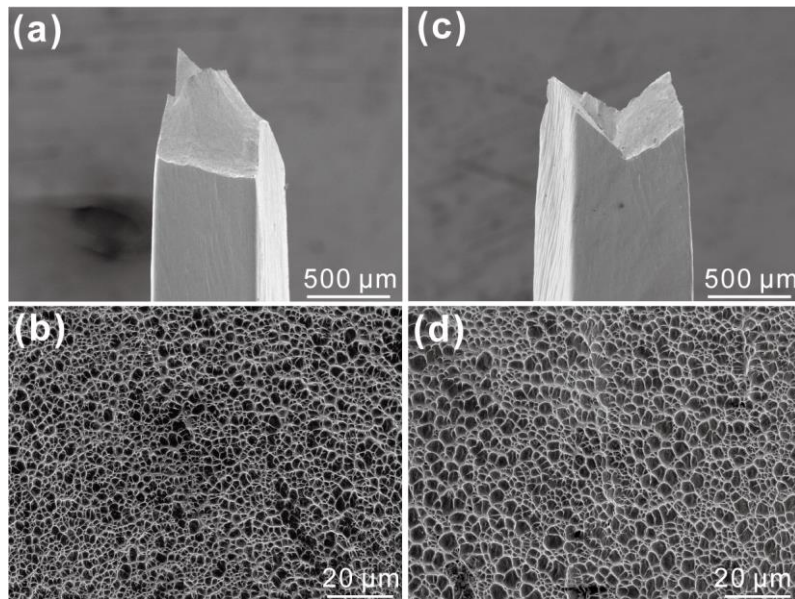


**Fig. 2.12** (a,c) Side and (b,d) top views of fracture surfaces in  $[\bar{1}23]$ -oriented single crystals of the equiatomic Cr-Co-Ni MEA deformed in tension at (a,c) room temperature and (b, d) 77 K.

the  $[\bar{1}2 9 21]$  orientation. The twinning shear stresses obtained at room temperature and 77 K are both considerably higher than that (291 MPa) theoretically estimated by Huang et al. [58]. The twinning shear stress increases significantly from 381 MPa at room temperature to 482 MPa at 77 K. This contrasts with the general belief that twinning is

stress-controlled in many FCC alloys making the twinning stress almost temperature-independent [59]. This will be later in detail in section 2.4.2.

Side and top views of the single-crystal fracture surfaces after failure at room temperature and 77 K are shown respectively in Figs. 2.12(a), (b) and Figs. 12(c), (d). The specimens exhibit apparent necking behavior and the dimple-type fracture surfaces typical for ductile failure at both temperatures.

### 2.3.3.2 Deformation fine structures

Evolution of deformation fine microstructures during deformation twinning in  $[\bar{1}23]$ -oriented single crystals of the equiatomic Cr-Co-Ni MEA at room temperature and 77 K were investigated by TEM/STEM observations with thin foils cut perpendicular to the twinning plane. The thickness and volume fraction of twins (and HCP layers, if present) were investigated by taking TEM dark-field (DF) images with the objective aperture set to the position of a reflection of the  $\{111\}$ -type of the twin for single crystals deformed to 205% strain (after the second inflection point), to failure at room temperature, and to failure at 77 K, as shown in Figs. 2.13(a), (c) and (e), respectively.

Since deformation twinning occurs uniformly on the (111) primary plane at room temperature, evolution of fine microstructures during deformation twinning can be investigated as a function of plastic strain at room temperature. As seen in the SAED pattern of the inset of Fig. 2.13(a), in addition to Bragg reflection spots of the matrix and twin, streaks are observed to run parallel to the (111) primary plane normal, indicating that thin twins are formed randomly. No significant difference is noticed in the SAED pattern of the inset of Fig. 2.13(c) when the strain level is increased to failure. However, both thickness and volume fraction of twins in the corresponding DF images increase

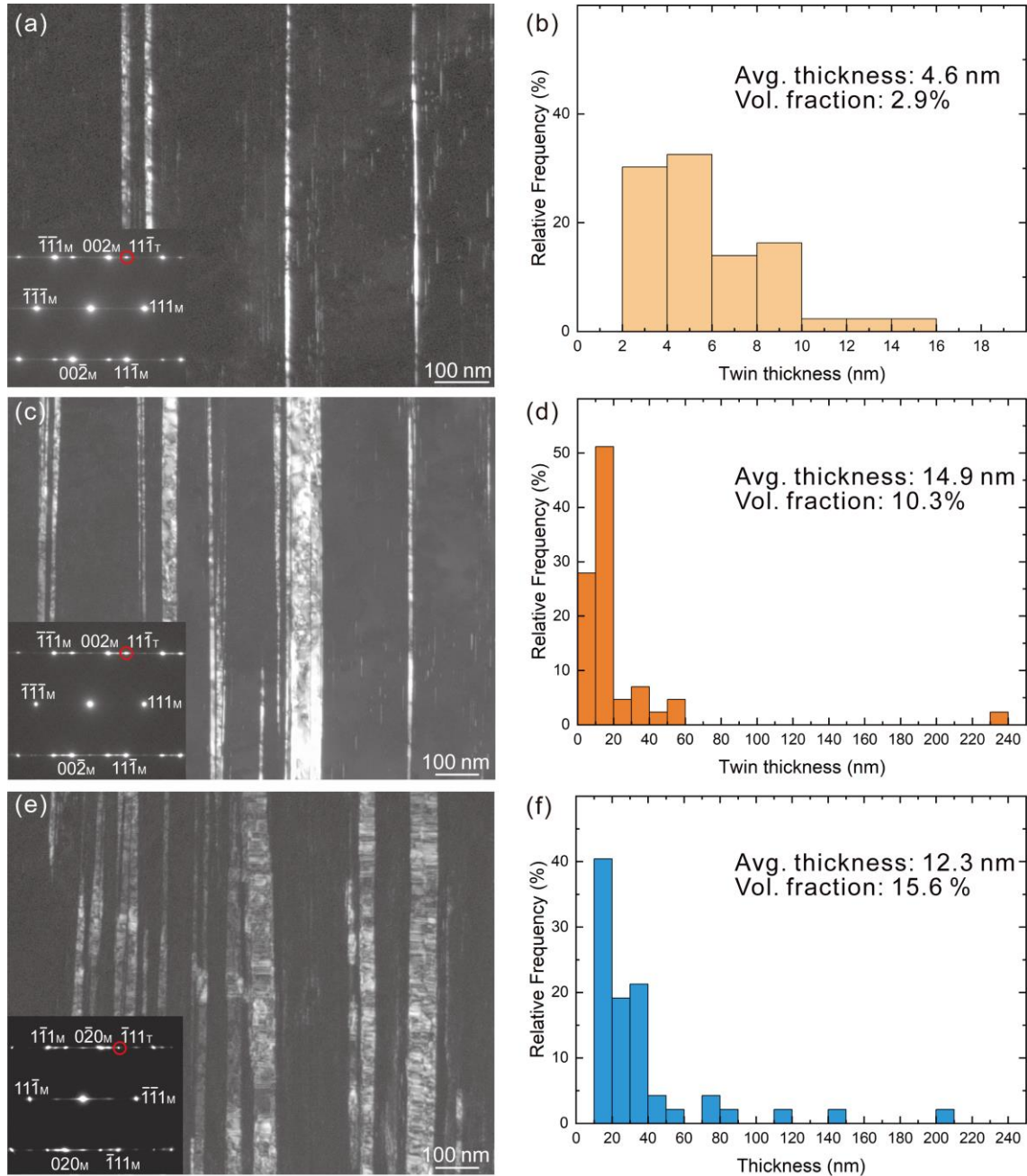


**Fig. 2.13** Deformation twins viewed end-on by dark-filed TEM imaging in  $[\bar{1}23]$ -oriented single crystals of the equiatomic Cr-Co-Ni MEA deformed in tension to different strains: (a) slightly beyond the inflection point, (c) to failure at room temperature and (e) to failure at 77 K. Twin thickness distributions for (a), (c) and (e) are shown in (b), (d) and (f), respectively.

considerably as the strain level is increased, as shown in the histograms of twin thickness distributions of Figs. 2.13(b) and (d). While the average twin thickness and twin volume fraction are estimated respectively to be 4.6 nm and 2.9% in the early stage of deformation

twinning, they both increase respectively to 14.9 nm and 10.3% at failure. This may indicate that when deformation twinning occurs uniformly, twin thickening plays an important role in increasing the twin volume fraction as the strain level increases in single crystals of the Cr-Co-Ni ternary equiatomic MEA.

At 77 K, on the other hand, deformation twinning occurs in the form of Lüders band in the equiatomic Cr-Co-Ni MEA so that localized deformation occurs only in the Lüders front that sweeps from one end of the gauge section to the other. Because of this, only a single crystal deformed to failure was examined, as shown in Figs. 2.13(e) and (f). Although some thick twins are sometimes formed, the average twin thickness at 77 K (12.3 nm) is comparable to that (14.9 nm) at room temperature. However, the twin volume fraction is larger at 77 K (15.6%) than at room temperature (10.3%).

We have noticed that DF imaging generally overestimates the thickness and volume fraction of twins (and HCP layers) because information corresponding not only to a Bragg reflection spot but also to streaking within the objective aperture is included in the image. We therefore further investigated evolution of deformation fine microstructures during deformation twinning in the equiatomic Cr-Co-Ni MEA by atomic-resolution STEM imaging using the same thin foils that were used for Figs. 2.13(a), (c) and (e). Although HCP layers are very difficult to resolve by EBSD mapping in the SEM and TEM DF imaging, thin HCP layers are clearly resolved in the STEM images of Figs. 2.14(a), (d) and (g) with the incidence of the  $\langle 110 \rangle$ -type. Histograms of twin and HCP layer thickness distributions are shown in the second and third columns of Fig. 2.14. Many of the twins are observed to be associated with a thin HCP layer in polycrystals of the equiatomic Cr-Co-Ni MEA (Miao et al., 2017; Niu et al., 2018). The average thickness of thin HCP layers formed next to twins (0.9-1.0 nm; 4-5 atomic layers) does not depend on the strain

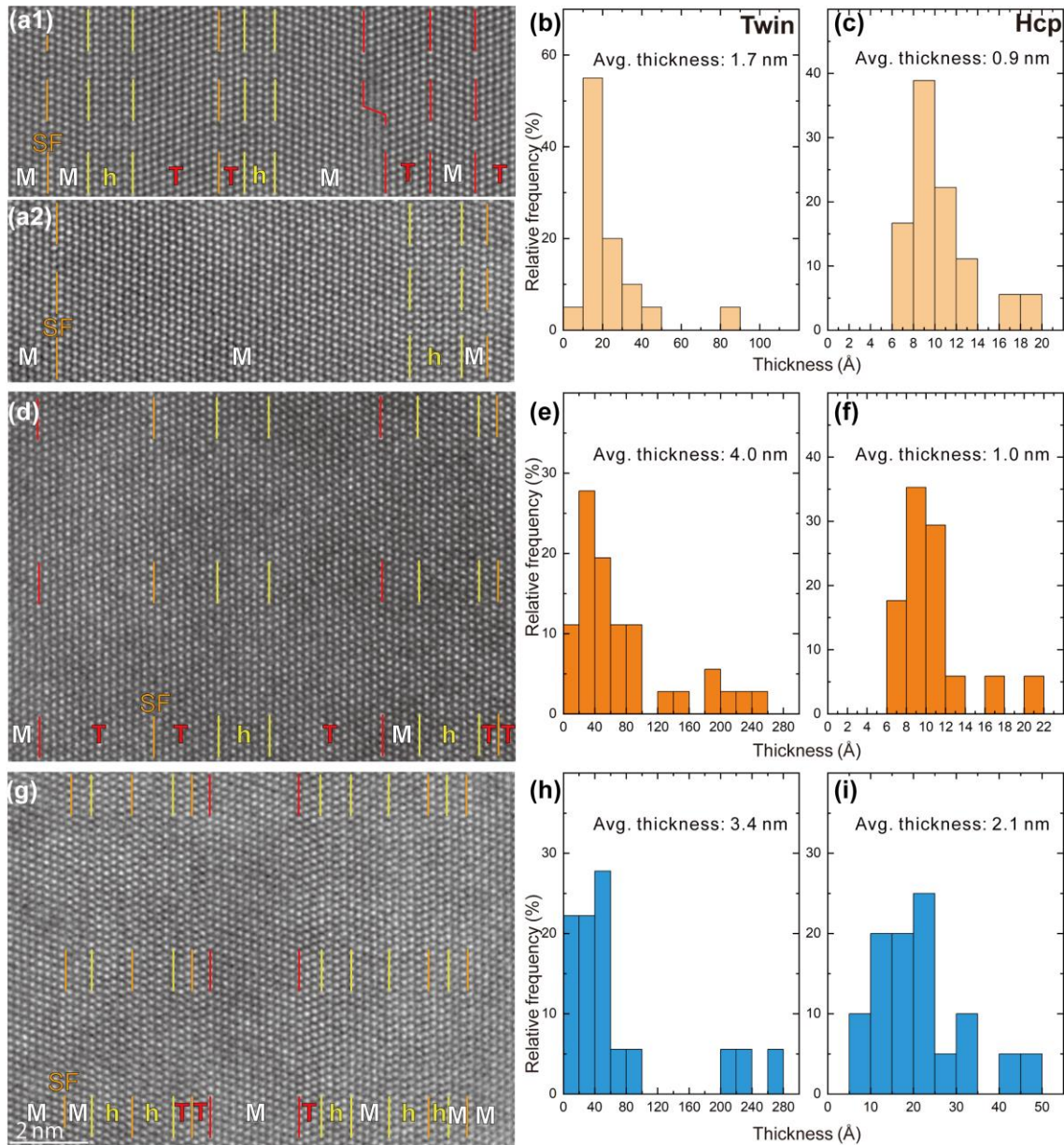


**Fig. 2.14** Atomic-resolution high-angle annular dark-field (HAADF) STEM images of deformation twins viewed end-on for  $[\bar{1}23]$ -oriented single crystals of the equiatomic Cr-Co-Ni MEA deformed in tension to different strains: (a) slightly beyond the inflection point, (d) to failure at room temperature and (g) to failure at 77 K. Twin and hcp-layer thickness distributions for (a), (d) and (g) are shown in (b), (e) and (h), and (c), (f) and (i), respectively.

level at room temperature but it increases to 2.1 nm at 77 K. The increased thickness of HCP layers may reflect the increased phase stability of the HCP structure with respect to the FCC structure at lower temperatures. Some thick HCP layers (2 and 5 nm at room

temperature and 77 K, respectively) are sometimes observed to form in isolated form without any association with twins, as shown by the example in Fig. 2.14(a2). The origin of these thick HCP layers may be different from that of thin HCP layers formed next to twins. This will be discussed in detail later in section 2.4.2. The occurrence of stacking fault within twins and HCP layers is also clearly resolved, making the twin thickness values estimated by STEM imaging considerably smaller than those estimated by TEM DF imaging although the trend is unchanged. The average twin thickness is observed to increase from 1.7 nm to 4.0 nm as the strain level increases at room temperature, while it is a bit smaller at 77 K (3.4 nm) when compared with the value at failure at room temperature.

## **2.4 Discussion**

### **2.4.1 Slip behavior**

#### **2.4.1.1 Anomalies in temperature dependence of CRSS**

The CRSS value obtained in the present study for the  $\{111\} \langle 1\bar{1}0 \rangle$  slip system in single crystals of the equiatomic Cr-Co-Ni MEA does not depend on the sense of applied stress (tension or compression) and increases with decreasing temperature from  $65 \pm 5$  MPa at room temperature to  $133 \pm 6$  MPa at 77 K. A dulling of the temperature dependence of CRSS, which may be due to the inertia effect occurs below 50 K. If this is ignored, and the temperature dependence of CRSS from above 50 K is extrapolated down to lower temperatures, a CRSS value of 225 MPa is obtained at 0 K. This value is considerably higher than that (168 MPa) obtained by similar extrapolation in the quinary

equiatomic Cr-Mn-Fe-Ni-Co HEA [42], and consistent with predictions of solid-solution hardening from theoretical calculations [20,21,23,60], including from MSAD values [20].

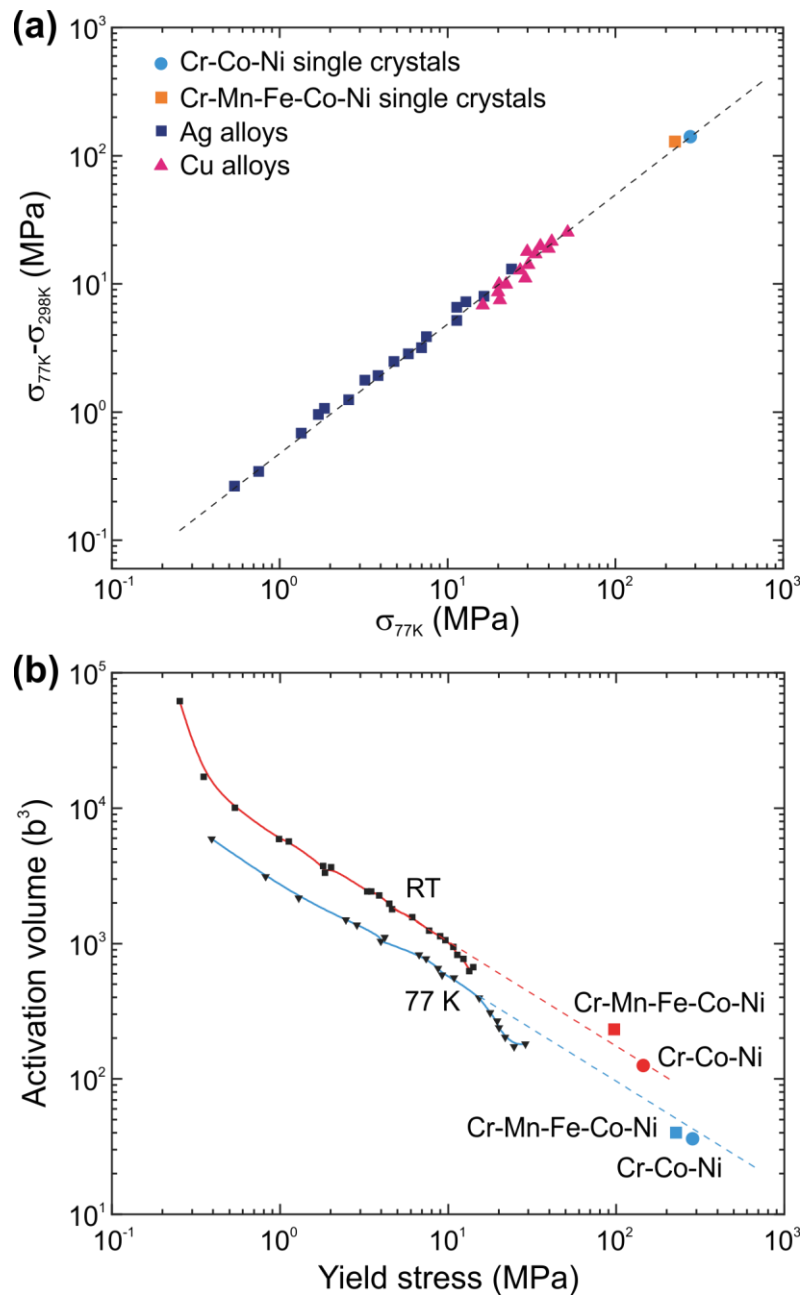


**Fig. 2.15** (a) The difference between the yield strength at 77 K and that at room temperature plotted as a function of the yield strength at 77 K for various FCC solid solutions. The results of Ag alloys and Cu alloys are from [61]. Axial yield stresses (instead of CRSS) are plotted for the Cr-Co-Ni MEA and Cr-Mn-Fe-Co-Ni HEA [42] single crystals. (b) Activation volumes at room temperature and 77 K for the Cr-Co-Ni MEA and Cr-Mn-Fe-Co-Ni HEA [42] single crystals and FCC solid solutions plotted as a function of their yield strength.

Solid-solution hardening is considered to be the main hardening mechanism in the present single crystals of the equiatomic Cr-Co-Ni MEA, because the concept of ‘stress equivalence’ proposed for FCC solid-solution alloys by Basinski et al. [61] holds true, as shown in Figs. 2.15(a) and (b). Although the yield strength of the equiatomic Cr-Co-Ni MEA is much higher than those of conventional binary FCC solid solutions, it falls exactly on the extension of the proportionality line between the yield strength at 77 K and the differential yield strength between room temperature and 77 K for a variety of FCC solid solutions (Fig. 2.15(a)). The values of activation volume measured for the equiatomic Cr-Co-Ni MEA at room temperature and 77 K also fall on their respective master curves together with conventional binary FCC solid solutions if plotted as a function of yield stress (Fig. 2.15(b)). According to Basinski et al. [61], such trends indicate that the thermal activation process for dislocation glide does not vary from one alloy to another and a single mechanism common to all solid-solution alloys is responsible for the thermal activation process.

In order to check this, we estimate the activation enthalpy for deformation in the present single crystals of the equiatomic Cr-Co-Ni MEA using the results of strain-rate jump tests (Fig. 2.4 and Fig. 2.7(a)). The shear stress ( $\tau$ ) dependent activation enthalpy,  $U(\tau)$  can be calculated from the following equation:

$$\dot{\gamma} = C \exp\left[\frac{-U(\tau)}{kT}\right] \quad (2-2)$$

where  $\dot{\gamma}$ ,  $k$  and  $T$  are the same as in equation (1) and  $C$  is a constant called the reference strain rate of the order of  $10^8 \text{ s}^{-1}$  [45,62,63]. To eliminate the constant  $C$ , we take the logarithm of both sides of equation (2) and then differentiate with respect to  $1/T$ ,

$$\begin{aligned}
 U(\tau) &= -k \left[ \frac{\partial \ln \dot{\gamma}}{\partial (1/T)} \right]_{\tau} \\
 &\approx -k \frac{\ln \dot{\gamma}(\tau, T_2) - \ln \dot{\gamma}(\tau, T_1)}{\frac{1}{T_2} - \frac{1}{T_1}}
 \end{aligned} \tag{2-3}$$

Values calculated with equations (2-2) and (2-3) are plotted in Fig. 2.16 with square and circle symbols, respectively. The agreement of the activation enthalpy values calculated with the two equations confirms the validity of choosing  $C=10^8 \text{ s}^{-1}$  in equation (2). In contrast,  $C=10^4 \text{ s}^{-1}$  has been assumed in certain theoretical treatments [22,60,62,63]. The activation enthalpy for the equiatomic Cr-Co-Ni MEA is calculated to be 0.61 eV at

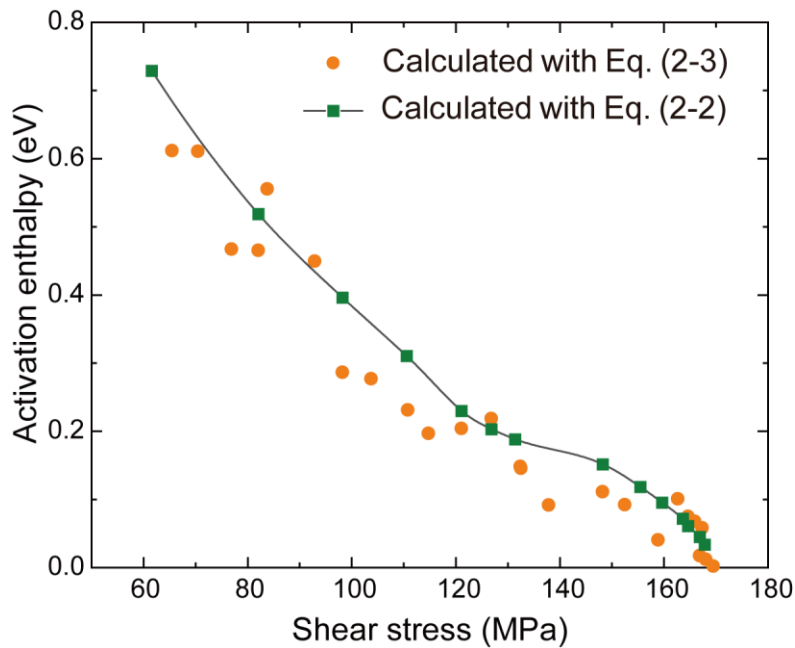


**Fig. 2.16** Shear stress dependence of activation enthalpy for deformation in the equiatomic Cr-Co-Ni MEA calculated using equation (2-2) with  $C=10^8 \text{ s}^{-1}$  and equation (2-3).

room temperature. Of interest to note is that the activation enthalpy of conventional FCC solid-solution alloys at room temperature is known to be roughly constant (around 0.6-0.7 eV), regardless of the type of solvent/solute atoms and their concentrations [45]. This is further evidence that a single mechanism common to all solid-solution alloys,

regardless of whether they are conventional, medium- or high-entropy alloys, is responsible for the thermally activated process of dislocation glide.

## 2.4.2 Twinning behavior

### 2.4.2.1 Twinning shear stress

The twinning shear stress for conventional FCC alloys is known to increase as stacking fault energy increase while it is believed not to depend much on temperature [25,64]. Recently, however, [64] reported the opposite trend in polycrystals, namely that the twinning stress is higher for a Cr-Co-Ni MEA than for a Cr-Mn-Fe-Co-Ni HEA despite the former having a lower stacking fault energy. We have found the same opposite trend in  $[\bar{1}23]$ -oriented single crystals of Cr-Co-Ni (this study) and Cr-Mn-Fe-Co-Ni [42], as shown Fig. 2.17(a), which also includes the twinning (shear) stress values obtained from polycrystals of these alloys [64]. The twinning shear stress evaluated at 77 K for single crystals of Cr-Co-Ni (blue circle) and Cr-Mn-Fe-Co-Ni (orange square) are shown in Fig. 2.17(a) as a function of stacking fault energy. As described in section 2.2.3, the stacking fault energies plotted likely represent their values at room temperature even though specimens deformed at 77 K were used for the measurement (because partial separation distances were measured in TEM foils at room temperature). For both polycrystals and single crystals, the twinning stress decreases with increasing stacking fault energy, which is opposite to what is generally believed for conventional FCC alloys [59]. Additionally, the clear temperature dependence of the twinning shear stress for single crystals of the Cr-Co-Ni MEA shown in Fig. 2.17(b) is also different from what is generally believed for conventional FCC alloys [59], namely that it should be temperature-independent. Since theoretical calculations indicate that the stacking fault

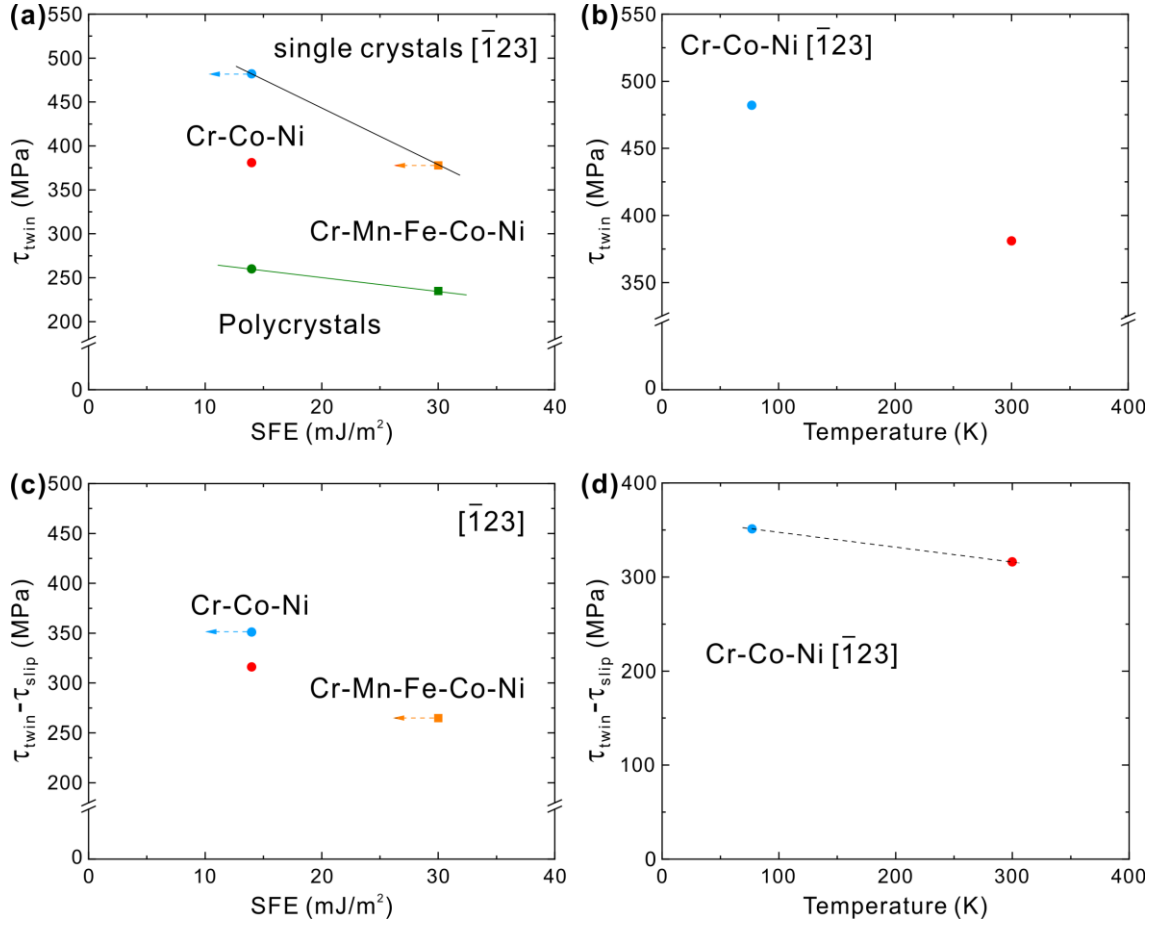


**Fig. 2.17** Dependence of the twinning shear stress for  $[\bar{1}23]$ -oriented single crystals of the equiatomic Cr-Co-Ni MEA on (a) stacking fault energy and (b) temperature. For comparison, data points for  $[\bar{1}23]$ -oriented single crystals of the equiatomic Cr-Mn-Fe-Co-Ni HEA [42] and polycrystals [25] are also shown. The difference between the twinning shear stress and the CRSS for the  $(111)[\bar{1}01]$  slip plotted as a function of (c) stacking fault energy and (d) temperature.

energy of the Cr-Co-Ni MEA decreases with decreasing temperature [30,37,38], Fig. 2.17(b) implies that the twinning stress decreases when stacking fault energy increases. As described in section 2.3.3, large plastic strain has to be accumulated by slip prior to the commencement of deformation twinning as in the case of TWIP steels [65–67]. This causes significantly different twinning shear stress depending on initial crystal orientation. The results of the present investigation on the orientation-dependent twinning behavior will be described in follow-on work to add additional perspective to the results in Fig.

2.17(b). To minimize any effect of the significantly different CRSS values of the Cr-Co-Ni MEA and Cr-Mn-Fe-Co-Ni HEA, the CRSS values were subtracted from the twinning shear stress and the difference plotted in Figs. 2.17(c) and (d) as a function of stacking fault energy and temperature, respectively. While this difference still exhibits a tendency to decrease with increasing stacking fault energy Figs. 2.17(c), it is relatively independent of temperature (Figs. 2.17(d)). The reason for this has yet to be clarified, although the possibility that twinning is indeed stress-dependent cannot be excluded. This will be further investigated with single crystals of other crystal orientations.

Regardless of deformation temperature (room temperature or 77 K), many of the twins are observed to be associated with a thin HCP layer with a thickness of 0.9-1.0 nm and 2.1 nm respectively at room temperature and 77 K. Thin HCP layers associated with twins were also reported by Niu et al.[27] in polycrystals of the Cr-Co-Ni ternary equiatomic MEA. The average thickness of twins formed is also very small; 4.0 and 3.4 nm respectively at room temperature and 77 K in the present study. This is consistent with what is observed in conventional FCC alloys. In these conventional FCC alloys, the twin thickness is known to decrease with decrease in stacking fault energy leading to the disappearance of serrations in stress-strain plots as well as clicking sounds during straining as the stacking fault energy decreases [59]. Although the reason for this has yet to be clarified in conventional FCC alloys, we suspect a possibility is that the formation of thin HCP layer next to twins limits their thickening and the propensity for HCP layer formation increases with decreasing stacking fault energy (i.e., the stability of the FCC structure decreases relative to the HCP structure). Consequently, formation of HCP layer may be more favored than further twin thickening, as Niu et al. [27] suggested. This is currently under survey with molecular dynamic simulations.

In addition to thin HCP layers formed next to twins, some thick HCP layers (2 and 5 nm at room temperature and 77 K, respectively) are sometimes observed to form in isolated form without any association with twins (Fig. 2.14(a2) and Fig.2.14(g)). Although the volume fraction of these isolated HCP layers is much smaller than that of twins, the population of the isolated HCP layers amounts to about 60% of all HCP layers in the early stage of twinning at room temperature and 77 K. This may indicate that the TRIP effect (HCP phase formation) occurs almost concurrently with and at the same stress level as the TWIP effect (twin formation) in the Cr-Co-Ni MEA by the motion of identical Shockley partial dislocations (either on every  $\{111\}$  plane or on every other  $\{111\}$  plane), although the amount of strain carried by the TRIP effect seems not to be large. At room temperature, the population of the isolated HCP layers is reduced to 29% of all HCP layers at failure, indicating the increasing importance of twin thickening in deformation as strain increases.

## 2.5 Conclusions

Bulk single crystals of the equiatomic Cr-Co-Ni MEA were tested in compression and tension at temperatures ranging from 14 to 1373 K and their mechanical response correlated with microstructure evolution across multiple length scales. Based on the present results, the following conclusions are drawn.

(1) The CRSS for  $\{111\}\langle 1\bar{1}0\rangle$  slip at room temperature is  $65 \pm 5$  MPa and it does not depend much on the sense of the applied load (tension or compression). It increases with decrease in temperature from  $65 \pm 5$  MPa at room temperature to  $133 \pm 6$  MPa at 77 K. A dulling of the temperature dependence of CRSS, which may be due to the inertia effect is clearly observed below 50 K. The CRSS at 0 K is estimated to be 225 MPa by

extrapolation of the temperature dependence of CRSS from above 50 K to lower temperatures. This value is ~34 % higher than the 168 MPa CRSS of the quinary equiatomic Cr-Mn-Fe-Ni-Co HEA obtained using a similar procedure. These values are consistent with theoretical predictions of solid-solution hardening, including those using MSAD values.

(2) The increase in CRSS from room temperature to 77 K implies that the concept of ‘stress equivalence’ originally proposed for simpler solid solutions holds true also for the equiatomic Cr-Co-Ni MEA except that the CRSS of the present MEA are significantly higher than those of any conventional FCC alloys. Additionally, the activation enthalpy for room-temperature deformation of the equiatomic Cr-Co-Ni MEA is evaluated to be 0.61 eV, which falls within the relatively narrow range (around 0.6-0.7 eV) of conventional FCC alloys, regardless of the type of solvent/solute atoms or their concentrations. This is clear evidence that a single mechanism common to all FCC solid-solution alloys is responsible for the thermal activation process of dislocation glide, regardless of whether they are conventional, medium- or high-entropy alloys.

(3) Dislocations with  $1/2\langle 110 \rangle$  Burgers vector dissociate into two  $1/6\langle 112 \rangle$  Shockley partials separated by a wide stacking fault. The stacking fault energy estimated from the separation distance is about  $14 \text{ mJm}^{-2}$ , which is sufficiently low to account for the planar nature of the observed dislocations and the occurrence of deformation twinning at 77 K and room temperature.

(5) Deformation twinning occurs both at 77 K and room temperature at a high plastic strain, above 150 and 200%, respectively. At 77 K, twinning occurs on conjugate  $(\bar{1}\bar{1}1)$  planes in the form of Lüders deformation after the tensile axis overshoots to  $[\bar{1}\bar{2} \ 9 \ 21]$  at an onset twinning shear stress of 482 MPa. At room temperature, on the other hand,

twinning occurs on primary (111) planes uniformly throughout the gauge section after primary and subsequent conjugate slip at an onset twinning shear stress of 381 MPa. HCP layer formation is observed in association with twinning both at 77 K and room temperature.

## Supplementary figures

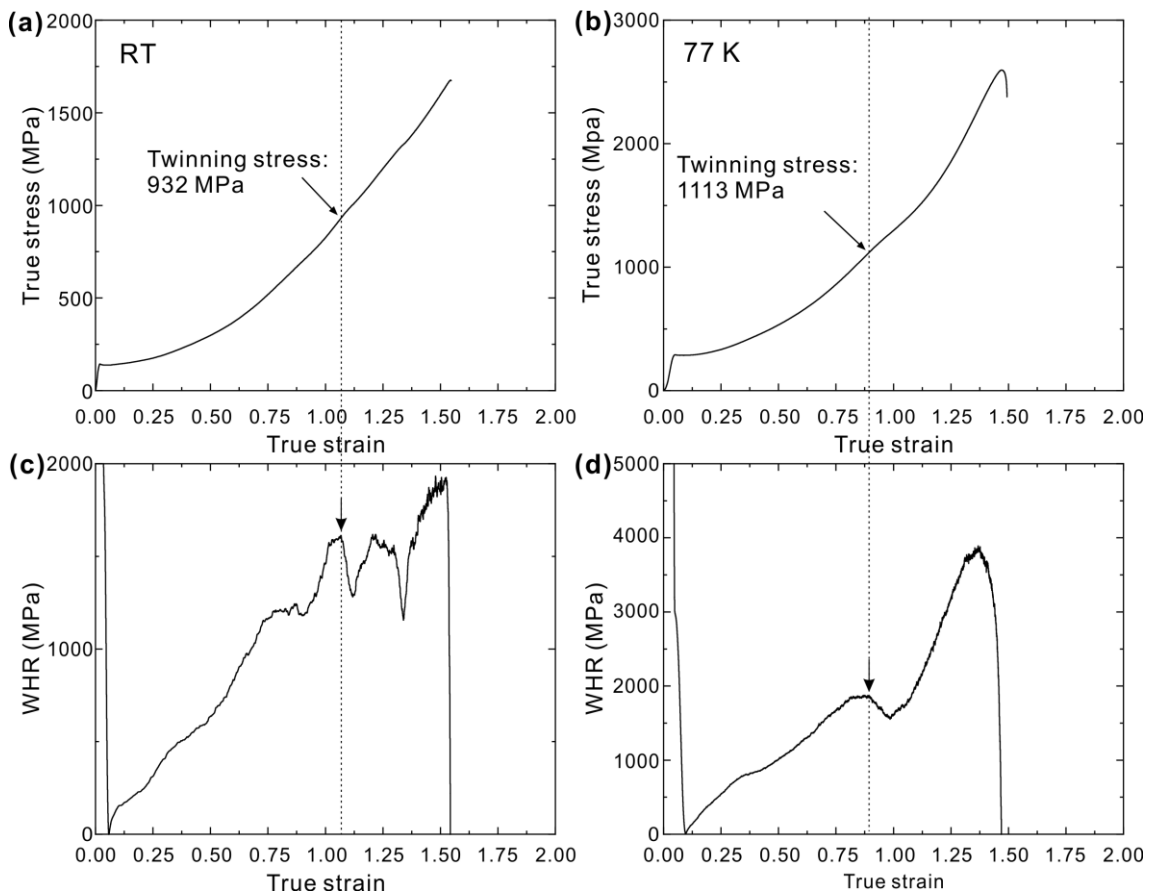


**Fig. S2.1.** (a,b) True stress - true strain curves and (c,d) the corresponding work-hardening rate curves obtained for  $[\bar{1}23]$ -oriented single crystals of the equiatomic Cr-Co-Ni MEA deformed in tension to failure at (a,c) room temperature and (b,d) 77K.

## Reference

- [1] E.P. George, D. Raabe, R.O. Ritchie, High-entropy alloys, *Nat. Rev. Mater.* 4 (2019) 515–534. <https://doi.org/10.1038/s41578-019-0121-4>.
- [2] E.P. George, W.A. Curtin, C.C. Tasan, High entropy alloys: A focused review of mechanical properties and deformation mechanisms, *Acta Mater.* 188 (2020) 435–

474. <https://doi.org/https://doi.org/10.1016/j.actamat.2019.12.015>.
- [3] Z. Li, S. Zhao, R.O. Ritchie, M.A. Meyers, Mechanical properties of high-entropy alloys with emphasis on face-centered cubic alloys, *Prog. Mater. Sci.* 102 (2019) 296–345. <https://doi.org/10.1016/j.pmatsci.2018.12.003>.
- [4] D.B. Miracle, O.N. Senkov, A critical review of high entropy alloys and related concepts, *Acta Mater.* 122 (2017) 448–511. <https://doi.org/10.1016/j.actamat.2016.08.081>.
- [5] F. Otto, Y. Yang, H. Bei, E.P. George, Relative effects of enthalpy and entropy on the phase stability of equiatomic high-entropy alloys, *Acta Mater.* 61 (2013) 2628–2638. <https://doi.org/10.1016/j.actamat.2013.01.042>.
- [6] Z. Wu, H. Bei, F. Otto, G.M. Pharr, E.P. George, Recovery, recrystallization, grain growth and phase stability of a family of FCC-structured multi-component equiatomic solid solution alloys, *Intermetallics.* 46 (2014) 131–140. <https://doi.org/https://doi.org/10.1016/j.intermet.2013.10.024>.
- [7] J. Ding, Q. Yu, M. Asta, R.O. Ritchie, Tunable stacking fault energies by tailoring local chemical order in CrCoNi medium-entropy alloys, *Proc. Natl. Acad. Sci. U. S. A.* 115 (2018) 8919–8924. <https://doi.org/10.1073/pnas.1808660115>.
- [8] D. Hua, Q. Xia, W. Wang, Q. Zhou, S. Li, D. Qian, J. Shi, H. Wang, Atomistic insights into the deformation mechanism of a CoCrNi medium entropy alloy under nanoindentation, *Int. J. Plast.* 142 (2021) 102997. <https://doi.org/10.1016/J.IJPLAS.2021.102997>.
- [9] Q.J. Li, H. Sheng, E. Ma, Strengthening in multi-principal element alloys with local-chemical-order roughened dislocation pathways, *Nat. Commun.* 10 (2019) 1–11. <https://doi.org/10.1038/s41467-019-11464-7>.
- [10] A. Tamm, A. Aabloo, M. Klintonberg, M. Stocks, A. Caro, Atomic-scale properties of Ni-based FCC ternary, and quaternary alloys, *Acta Mater.* 99 (2015) 307–312. <https://doi.org/10.1016/j.actamat.2015.08.015>.
- [11] F.X. Zhang, S. Zhao, K. Jin, H. Xue, G. Velisa, H. Bei, R. Huang, J.Y.P. Ko, D.C. Pagan, J.C. Neufeind, W.J. Weber, Y. Zhang, Local Structure and Short-Range Order in a NiCoCr Solid Solution Alloy, *Phys. Rev. Lett.* 118 (2017) 1–6. <https://doi.org/10.1103/PhysRevLett.118.205501>.
- [12] R. Zhang, S. Zhao, J. Ding, Y. Chong, T. Jia, C. Ophus, M. Asta, R.O. Ritchie, A.M. Minor, Short-range order and its impact on the CrCoNi medium-entropy alloy, *Nature.* 581 (2020) 283–287. <https://doi.org/10.1038/s41586-020-2275-z>.
- [13] A. Gali, E.P. George, Tensile properties of high- and medium-entropy alloys, *Intermetallics.* 39 (2013) 74–78. <https://doi.org/10.1016/j.intermet.2013.03.018>.
- [14] B. Gludovatz, A. Hohenwarter, D. Catoor, E.H. Chang, E.P. George, R.O. Ritchie, A fracture-resistant high-entropy alloy for cryogenic applications, *Science.* 345 (2014) 1153–1158. <https://doi.org/10.1126/science.1254581>.
- [15] B. Gludovatz, A. Hohenwarter, K.V.S. Thurston, H. Bei, Z. Wu, E.P. George, R.O. Ritchie, Exceptional damage-tolerance of a medium-entropy alloy CrCoNi at cryogenic temperatures, *Nat. Commun.* 7 (2016) 1–8. <https://doi.org/10.1038/ncomms10602>.
- [16] Z. Li, K.G. Pradeep, Y. Deng, D. Raabe, C.C. Tasan, Metastable high-entropy dual-phase alloys overcome the strength-ductility trade-off, *Nature.* 534 (2016) 227–230. <https://doi.org/10.1038/nature17981>.
- [17] Z. Li, D. Raabe, Strong and Ductile Non-equiatomic High-Entropy Alloys: Design,

- Processing, Microstructure, and Mechanical Properties, *Jom*. 69 (2017) 2099–2106. <https://doi.org/10.1007/s11837-017-2540-2>.
- [18] F. Otto, A. Dlouhy, C. Somsen, H. Bei, G. Eggeler, E.P. George, The influences of temperature and microstructure on the tensile properties of a CoCrFeMnNi high-entropy alloy, *Acta Mater.* 61 (2013) 5743–5755. <https://doi.org/https://doi.org/10.1016/j.actamat.2013.06.018>.
- [19] Y. Yang, T. Chen, L. Tan, J.D. Poplawsky, K. An, Y. Wang, G.D. Samolyuk, K. Littrell, A.R. Lupini, A. Borisevich, E.P. George, Bifunctional nanoprecipitates strengthen and ductilize a medium-entropy alloy, *Nature*. 595 (2021) 245–249. <https://doi.org/10.1038/s41586-021-03607-y>.
- [20] N.L. Okamoto, K. Yuge, K. Tanaka, H. Inui, E.P. George, Atomic displacement in the CrMnFeCoNi high-entropy alloy—A scaling factor to predict solid solution strengthening, *AIP Adv.* 6 (2016) 125008. <https://doi.org/10.1063/1.4971371>.
- [21] I. Toda-Caraballo, P.E.J. Rivera-Díaz-del-Castillo, P.E.J. Rivera-Díaz-Del-Castillo, Modelling solid solution hardening in high entropy alloys, *Acta Mater.* 85 (2015) 14–23. <https://doi.org/10.1016/j.actamat.2014.11.014>.
- [22] C. Varvenne, G.P.M.M. Leyson, M. Ghazisaeidi, W.A. Curtin, Solute strengthening in random alloys, *Acta Mater.* 124 (2017) 660–683. <https://doi.org/https://doi.org/10.1016/j.actamat.2016.09.046>.
- [23] Y.Y. Zhao, T.G. Nieh, Correlation between lattice distortion and friction stress in Ni-based equiatomic alloys, *Intermetallics*. 86 (2017) 45–50. <https://doi.org/10.1016/j.intermet.2017.03.011>.
- [24] G. Laplanche, A. Kostka, O.M. Horst, G. Eggeler, E.P. George, Microstructure evolution and critical stress for twinning in the CrMnFeCoNi high-entropy alloy, *Acta Mater.* 118 (2016) 152–163. <https://doi.org/https://doi.org/10.1016/j.actamat.2016.07.038>.
- [25] G. Laplanche, A. Kostka, C. Reinhart, J. Hunfeld, G. Eggeler, E.P. George, Reasons for the superior mechanical properties of medium-entropy CrCoNi compared to high-entropy CrMnFeCoNi, *Acta Mater.* 128 (2017) 292–303. <https://doi.org/https://doi.org/10.1016/j.actamat.2017.02.036>.
- [26] J. Miao, C.E. Slone, T.M. Smith, C. Niu, H. Bei, M. Ghazisaeidi, G.M. Pharr, M.J. Mills, The evolution of the deformation substructure in a Ni-Co-Cr equiatomic solid solution alloy, *Acta Mater.* 132 (2017) 35–48. <https://doi.org/10.1016/j.actamat.2017.04.033>.
- [27] C. Niu, C.R. LaRosa, J. Miao, M.J. Mills, M. Ghazisaeidi, Magnetically-driven phase transformation strengthening in high entropy alloys, *Nat. Commun.* 9 (2018) 1–9. <https://doi.org/10.1038/s41467-018-03846-0>.
- [28] C.E. Slone, S. Chakraborty, J. Miao, E.P. George, M.J. Mills, S.R. Niezgod, Influence of deformation induced nanoscale twinning and FCC-HCP transformation on hardening and texture development in medium-entropy CrCoNi alloy, *Acta Mater.* 158 (2018) 38–52. <https://doi.org/10.1016/j.actamat.2018.07.028>.
- [29] Y. Wu, M. Bönisch, S. Alkan, W. Abuzaid, H. Sehitoglu, Experimental determination of latent hardening coefficients in FeMnNiCoCr, *Int. J. Plast.* 105 (2018) 239–260. <https://doi.org/10.1016/j.ijplas.2018.02.016>.
- [30] Z. Zhang, H. Sheng, Z. Wang, B. Gludovatz, Z. Zhang, E.P. George, Q. Yu, S.X. Mao, R.O. Ritchie, Dislocation mechanisms and 3D twin architectures generate exceptional strength-ductility-toughness combination in CrCoNi medium-entropy

- alloy, *Nat. Commun.* 8 (2017) 1–8. <https://doi.org/10.1038/ncomms14390>.
- [31] M. Schneider, E.P. George, T.J. Manescau, T. Zaleski, J. Hunfeld, A. Dlouhy, G. Eggeler, G. Laplanche, T. Zálezák, J. Hunfeld, A. Dlouhý, G. Eggeler, G. Laplanche, Analysis of strengthening due to grain boundaries and annealing twin boundaries in the CrCoNi medium-entropy alloy, *Int. J. Plast.* 124 (2019) 155–169. <https://doi.org/https://doi.org/10.1016/j.ijplas.2019.08.009>.
- [32] Z. Wu, H. Bei, G.M. Pharr, E.P. George, Temperature dependence of the mechanical properties of equiatomic solid solution alloys with face-centered cubic crystal structures, *Acta Mater.* 81 (2014) 428–441. <https://doi.org/https://doi.org/10.1016/j.actamat.2014.08.026>.
- [33] M. Bahramyan, R.T. Mousavian, D. Brabazon, Study of the plastic deformation mechanism of TRIP-TWIP high entropy alloys at the atomic level, *Int. J. Plast.* 127 (2020) 102649. <https://doi.org/10.1016/j.ijplas.2019.102649>.
- [34] B.C. De Cooman, Y. Estrin, S.K. Kim, Twinning-induced plasticity (TWIP) steels, *Acta Mater.* 142 (2018) 283–362. <https://doi.org/10.1016/j.actamat.2017.06.046>.
- [35] O. Grässel, L. Krüger, G. Frommeyer, L.W. Meyer, High strength Fe-Mn-(Al, Si) TRIP/TWIP steels development - properties - application, *Int. J. Plast.* 16 (2000) 1391–1409. [https://doi.org/10.1016/S0749-6419\(00\)00015-2](https://doi.org/10.1016/S0749-6419(00)00015-2).
- [36] X. Lu, J. Zhao, Z. Wang, B. Gan, J. Zhao, G. Kang, X. Zhang, Crystal plasticity finite element analysis of gradient nanostructured TWIP steel, *Int. J. Plast.* 130 (2020) 102703. <https://doi.org/10.1016/j.ijplas.2020.102703>.
- [37] Y.H. Zhang, Y. Zhuang, A. Hu, J.J. Kai, C.T. Liu, The origin of negative stacking fault energies and nano-twin formation in face-centered cubic high entropy alloys, *Scr. Mater.* 130 (2017) 96–99. <https://doi.org/10.1016/j.scriptamat.2016.11.014>.
- [38] S. Zhao, G.M. Stocks, Y. Zhang, Stacking fault energies of face-centered cubic concentrated solid solution alloys, *Acta Mater.* 134 (2017) 334–345. <https://doi.org/10.1016/j.actamat.2017.05.001>.
- [39] W. Abuzaid, L. Patriarca, A study on slip activation for a coarse-grained and single crystalline CoCrNi medium entropy alloy, *Intermetallics.* 117 (2020) 106682. <https://doi.org/10.1016/J.INTERMET.2019.106682>.
- [40] G. Laplanche, M. Schneider, F. Scholz, J. Frenzel, G. Eggeler, J. Schreuer, Processing of a single-crystalline CrCoNi medium-entropy alloy and evolution of its thermal expansion and elastic stiffness coefficients with temperature, *Scr. Mater.* 177 (2020) 44–48. <https://doi.org/10.1016/j.scriptamat.2019.09.020>.
- [41] B. Uzer, S. Picak, J. Liu, T. Jozaghi, D. Canadinc, I. Karaman, Y.I. Chumlyakov, I. Kireeva, On the mechanical response and microstructure evolution of NiCoCr single crystalline medium entropy alloys, *Mater. Res. Lett.* 6 (2018) 442–449. <https://doi.org/10.1080/21663831.2018.1478331>.
- [42] M. Kawamura, M. Asakura, N.L. Okamoto, K. Kishida, H. Inui, E.P. George, Plastic deformation of single crystals of the equiatomic Cr–Mn–Fe–Co–Ni high-entropy alloy in tension and compression from 10 K to 1273 K, *Acta Mater.* 203 (2021) 116454. <https://doi.org/10.1016/j.actamat.2020.10.073>.
- [43] N.L. Okamoto, S. Fujimoto, Y. Kambara, M. Kawamura, Z.M.T. Chen, H. Matsunoshita, K. Tanaka, H. Inui, E.P. George, Size effect, critical resolved shear stress, stacking fault energy, and solid solution strengthening in the CrMnFeCoNi high-entropy alloy, *Sci. Rep.* 6 (2016) 35863.
- [44] D. Zhou, Z. Chen, K. Ehara, K. Nitsu, K. Tanaka, H. Inui, Effects of annealing on

- hardness, yield strength and dislocation structure in single crystals of the equiatomic Cr-Mn-Fe-Co-Ni high entropy alloy, *Scr. Mater.* 191 (2021) 173–178. <https://doi.org/10.1016/j.scriptamat.2020.09.039>.
- [45] H. Suzuki, E. Kuramoto, Thermally activated glide in face-centered cubic alloys, *Trans JIM.* 9. (1968) 697–702.
- [46] R.B. Schwarz, R.D. Isaac, A. V. Granato, Dislocation inertial effects in the plastic deformation of dilute alloys of lead and copper, *Phys. Rev. Lett.* 38 (1977) 554–557. <https://doi.org/10.1103/PHYSREVLETT.38.554>.
- [47] A.S. Tirunilai, T. Hanemann, C. Reinhart, V. Tschan, K.P. Weiss, G. Laplanche, J. Freudenberger, M. Heilmaier, A. Kauffmann, Comparison of cryogenic deformation of the concentrated solid solutions CoCrFeMnNi, CoCrNi and CoNi, *Mater. Sci. Eng. A.* 783 (2020) 139290. <https://doi.org/10.1016/j.msea.2020.139290>.
- [48] K. Sugita, N. Matsuoka, M. Mizuno, H. Araki, Vacancy formation enthalpy in CoCrFeMnNi high-entropy alloy, *Scr. Mater.* 176 (2020) 32–35. <https://doi.org/10.1016/j.scriptamat.2019.09.033>.
- [49] C.W. Tsai, C. Lee, P.T. Lin, X. Xie, S. Chen, R. Carroll, M. Leblanc, B.A.W. Brinkman, P.K. Liaw, K.A. Dahmen, J.W. Yeh, Portevin-Le Chatelier mechanism in face-centered-cubic metallic alloys from low to high entropy, *Int. J. Plast.* 122 (2019) 212–224. <https://doi.org/10.1016/j.ijplas.2019.07.003>.
- [50] W. Abuzaid, H. Sehitoglu, Critical resolved shear stress for slip and twin nucleation in single crystalline FeNiCoCrMn high entropy alloy, *Mater. Charact.* 129 (2017) 288–299. <https://doi.org/10.1016/j.matchar.2017.05.014>.
- [51] Z. Wu, Y. Gao, H. Bei, Thermal activation mechanisms and Labusch-type strengthening analysis for a family of high-entropy and equiatomic solid-solution alloys, *Acta Mater.* 120 (2016) 108–119. <https://doi.org/https://doi.org/10.1016/j.actamat.2016.08.047>.
- [52] D.J.H. Cockayne, M.L. Jenkins, I.L.F. Ray, The measurement of stacking-fault energies of pure face-centred cubic metals, *Philos. Mag.* 24 (1971) 1383–1392. <https://doi.org/10.1080/14786437108217419>.
- [53] W.M. Stobbs, C.H. Sworn, The weak beam technique as applied to the determination of the stacking-fault energy of copper, *Philos. Mag.* 24 (1971) 1365–1381. <https://doi.org/10.1080/14786437108217418>.
- [54] T.M. Smith, M.S. Hooshmand, B.D. Esser, F. Otto, D.W. McComb, E.P. George, M. Ghazisaeidi, M.J. Mills, Atomic-scale characterization and modeling of 60° dislocations in a high-entropy alloy, *Acta Mater.* 110 (2016) 352–363. <https://doi.org/10.1016/j.actamat.2016.03.045>.
- [55] S.F. Liu, Y. Wu, H.T. Wang, J.Y. He, J.B. Liu, C.X. Chen, X.J. Liu, H.T. Wang, Z.P. Lu, Stacking fault energy of face-centered-cubic high entropy alloys, *Intermetallics.* 93 (2018) 269–273. <https://doi.org/10.1016/j.intermet.2017.10.004>.
- [56] M. Shih, J. Miao, M. Mills, M. Ghazisaeidi, Stacking fault energy in concentrated alloys, *Nat. Commun.* 12 (2021) 1–10. <https://doi.org/10.1038/s41467-021-23860-z>.
- [57] P. Haasen, Mechanical properties of solid solutions, in: R.W. Cahn, P. Haasen (Eds.), *Phys. Metall.* (Fourth Ed., Elsevier Science, North-Holland, Amsterdam, 1996: pp. 2009–2073. <https://www.elsevier.com/books/physical-metallurgy/cahn/978-0-444-89875-3>.
- [58] H. Huang, X. Li, Z. Dong, W. Li, S. Huang, D. Meng, X. Lai, T. Liu, S. Zhu, L. Vitos, Critical stress for twinning nucleation in CrCoNi-based medium and high entropy

- alloys, *Acta Mater.* 149 (2018) 388–396. <https://doi.org/https://doi.org/10.1016/j.actamat.2018.02.037>.
- [59] J.W. Christian, S. Mahajan, Deformation twinning, *Prog. Mater. Sci.* 39 (1995) 1–157. [https://doi.org/https://doi.org/10.1016/0079-6425\(94\)00007-7](https://doi.org/https://doi.org/10.1016/0079-6425(94)00007-7).
- [60] C.C. Varvenne, A. Luque, W.A. Curtin, Theory of strengthening in fcc high entropy alloys, *Acta Mater.* 118 (2016) 164–176. <https://doi.org/10.1016/j.actamat.2016.07.040>.
- [61] Z.S. Basinski, R.A. Foxall, R. Pascual, Stress equivalence of solution hardening, *Scr. Metall.* 6 (1972) 807–814. [https://doi.org/https://doi.org/10.1016/0036-9748\(72\)90052-X](https://doi.org/https://doi.org/10.1016/0036-9748(72)90052-X).
- [62] D.L. Olmsted, L.G. Hector, W.A. Curtin, Molecular dynamics study of solute strengthening in Al/Mg alloys, *J. Mech. Phys. Solids.* 54 (2006) 1763–1788. <https://doi.org/https://doi.org/10.1016/j.jmps.2005.12.008>.
- [63] G.P.M. Leyson, W.A. Curtin, L.G. Hector, C.F. Woodward, Quantitative prediction of solute strengthening in aluminium alloys, *Nat. Mater.* 9 (2010) 750–755. <https://doi.org/10.1038/nmat2813>.
- [64] P. Haasen, Mechanical properties of solid solutions, in: R.W. Cahn, P. Haasen (Eds.), *Phys. Metall.*, Fourth Ed., North-Holland, Oxford, 1996: pp. 2009–2073. <https://doi.org/https://doi.org/10.1016/B978-044489875-3/50028-4>.
- [65] H. Idrissi, K. Renard, L. Ryelandt, D. Schryvers, P.J. Jacques, On the mechanism of twin formation in Fe–Mn–C TWIP steels, *Acta Mater.* 58 (2010) 2464–2476. <https://doi.org/10.1016/J.ACTAMAT.2009.12.032>.
- [66] H. Idrissi, K. Renard, D. Schryvers, P.J. Jacques, On the relationship between the twin internal structure and the work-hardening rate of TWIP steels, *Scr. Mater.* 63 (2010) 961–964. <https://doi.org/10.1016/j.scriptamat.2010.07.016>.
- [67] H. Idrissi, K. Renard, D. Schryvers, P.J. Jacques, TEM investigation of the formation mechanism of deformation twins in Fe-Mn-Si-Al TWIP steels, *Philos. Mag.* 93 (2013) 4378–4391. <https://doi.org/10.1080/14786435.2013.832837>.

## Chapter 3 Short-range order in the equiatomic Cr-Co-Ni

### MEA

#### 3.1 Introduction

In recent years, a new class of alloys called high- and medium-entropy alloys (HEAs and MEAs) have attracted the attention of a tremendous number of materials scientists all over the world. Research on HEAs and MEAs has thus become one of the most active areas in materials science today with many review papers published recently [1–8]. This stems from the fact that some solid-solution HEAs and MEAs exhibit extraordinary mechanical properties such as simultaneous achievement of high strength and high ductility, although such extraordinary mechanical properties are not necessarily achieved by all HEAs and MEAs [2,3]. Severely distorted crystal lattices of HEAs and MEAs, which arise from varying atomic sizes of the constituent elements, are thought to play a decisive role in the extraordinary mechanical properties [9,10]. Many early investigations assumed a completely random atomic structure in HEAs and MEAs. In recent years, however, short-range ordering (SRO) that may occur as a result of the mixing enthalpy contribution to the Gibbs free energy [11], has been a focus of intensive studies in HEAs and MEAs [4,12]. Some researchers foresee that further improvement of mechanical properties may be possible by tuning the degree of SRO in HEAs and MEAs [13,14].

SRO is not restricted to HEAs and MEAs. Many conventional alloys, even simple binaries, are known to exhibit non-random atomic structures accompanied by SRO or short-range clustering (SRC) of the constituent elements with the degree of SRO and SRC varying depending on heat treatment [15–22]. SRO in conventional alloys is

demonstrated by x-ray, neutron or electron diffraction [23,24], or by electrical resistivity and specific heat measurements [25,26]. In the last several decades, effects of SRO on strength have been the subject of many investigations, especially in solid-solution alloys with the face-centered cubic (FCC) structure. Many of these investigations employed one (or some) of the above-mentioned methods (with electrical resistivity being the most frequently employed [19,27], sometimes combined with x-ray, neutron or electron diffraction [22,28,29]) to monitor the evolution of SRO and to subsequently correlate it with strength. In the early days, simple theories were proposed to account for SRO strengthening that scaled with  $\gamma_{db}/b$  ( $\gamma_{db}$ : SRO domain-boundary energy,  $b$ : the magnitude of dislocation Burgers vector) on the assumption that the interaction of SRO domain-boundaries and gliding dislocations contributes to strengthening [30,31]. However, Cohen and Fine [32] later concluded that the overall alloy strength is not affected significantly by SRO; rather, they argued, the effects of SRO should be manifested as a yield drop in the stress-strain curve with the magnitude of the yield drop depending on the degree of SRO. This conclusion was based on the consideration that the initial high resistance to dislocation motion arising from SRO is quickly lowered by the passage of the first several dislocations that destroy SRO on the slip plane; subsequent dislocations moving on the same slip plane then experience less resistance resulting in coarse (localized) slip. Consistent with the above notion of Cohen and Fine, Scattergood and Bever [17] reported that, while the magnitude of the yield-drop correlates well with the degree of SRO developed, all other mechanical properties including yield strength do not correlate with SRO in Cu-Al polycrystals. However, many other experimental observations that contradicted Cohen and Fine [32] have been reported from time to time. For example, Büttner and Nembach [18] and Svitak and Asimow [33] reported that

neither the yield strength nor the yield-drop correlate with the degree of SRO in Cu-Au and Ag-Au polycrystals, respectively. On top of that, Büttner and Nembach [18] reported that the yield strength of Cu-Au polycrystals reached a minimum when the degree of SRO reached a maximum. While this contradicted the general belief that strength increases with the degree of SRO developed [30,31] it was subsequently shown to be consistent with elasticity calculations of dislocations in Ag-Al alloys by Patu and Arsenault [34]. Thus, when the entire weight of the evidence is considered, it becomes clear that there is a lack of agreement on how strength varies with SRO, even in conventional alloys.

SRO has been reported in the equiatomic Cr-Co-Ni MEA [11,35,36], as well as in FCC HEAs of the Cr-Mn-Fe-Co-Ni system and its FCC MEA subsystems [13,35,37–47]. Among these, the equiatomic Cr-Co-Ni MEA is the most extensively studied. It is worth noting, however, that SRO in the equiatomic Cr-Co-Ni MEA, as well its effects on mechanical properties, are mostly investigated by theoretical calculations based on density-functional theory (DFT) and simulations [13,14,39,41,44]. A substantial increase in strength associated with SRO has been suggested by DFT calculations due to local fluctuations in stacking fault (SF) energy arising from the non-random atomic structure [13,14,39,41,44]. On the other hand, experimental efforts to demonstrate the presence of SRO in the equiatomic Cr-Co-Ni MEA and to elucidate its effects on mechanical properties are rather limited [43,48]. This is due mainly to the difficulty in experimentally proving the presence of SRO by x-ray and electron diffraction because of the very small difference in atomic scattering factor of the constituent elements, Cr, Co and Ni over a wide range of scattering angles (Fig. S3.1). Although there are some reports of SRO based on electron diffraction and diffraction imaging [37,43], the evidence is not unambiguous. Furthermore, different experimental investigators have drawn opposing conclusions on

the effects of SRO on mechanical properties [43,48]. Zhang [43] reported remarkable strengthening (yield strength increase of 25%) due to SRO in equiatomic Cr-Co-Ni MEA polycrystals after annealing at 1273 K followed by furnace cooling, while Inoue et al. [48] reported no measurable effect of SRO on the yield strength of equiatomic Cr-Co-Ni MEA polycrystals after annealing at 973 K for 384 hours followed by water quenching. Note that neither of these studies quantified the degree SRO responsible for their respective mechanical properties. Therefore, more work is needed to explore the effect of SRO on the strength of the equiatomic Cr-Co-Ni MEA.

In the present study, the following aspects were investigated (1) the evolution of SRO in the equiatomic Cr-Co-Ni MEA by monitoring changes in electrical resistivity, and (2) the effect of the degree of SRO on the mechanical properties of single crystals of the equiatomic Cr-Co-Ni MEA in tension and in compression at room temperature and liquid-nitrogen temperature. In particular, how critical resolved shear stress (CRSS) for  $\{111\}\langle 110\rangle$  slip, onset shear stress for  $\{111\}\langle 112\rangle$  twinning, yield drop, slip localization as well as stacking fault (SF) energy are affected by the development of SRO by monitoring electrical resistivity changes, were investigated.

### **3.2 Materials and experiments**

Ingots of the equiatomic Cr-Co-Ni alloy were prepared by arc-melting high-purity (>99.9%) Cr, Co and Ni in an argon atmosphere. Some of these ingots were homogenized at 1473 K for 168 hours. Rectangular parallelepiped specimens were cut from the homogenized ingots, cold rolled to 50% thickness reduction and then recrystallized at 1273 K for 2 hours, followed by water quenching. Slices with dimensions  $50\times 2\times 0.5$  mm<sup>3</sup> were cut from the recrystallized ingots and then mechanically polished with 1  $\mu$ m

diamond paste. Electrical resistivity measurements were performed on these slices by the four-terminals method at room temperature to monitor the evolution of short-range order after isothermal annealing at various temperatures (573 to 973 K). Some of the arc-melted ingots were used to grow single crystals of the Cr-Co-Ni MEA with an optical floating-zone furnace in flowing Ar gas at a growth rate of 10 mm/h. The single crystals were homogenized at 1473 K for 168 hours followed by water quenching. Then, they were annealed at 573-873 K for 168-504 hours followed by water quenching. After determining crystallographic orientations by the x-ray back-reflection Laue method, single crystal specimens with the  $[\bar{1}23]$  -loading-axis direction were cut by spark-machining for compressive and tensile tests, measuring  $2 \times 2 \times 5 \text{ mm}^3$  in the gage section. Specimen surfaces were polished first mechanically and then electrolytically with a solution of perchloric acid, n-butanol and methanol (7.5:29:63.5 by volume) to obtain a mirror finish. Compression and tensile tests were conducted on an Instron-type testing machine at room temperature (in ambient air) and at 77 K (with the specimen immersed in liquid nitrogen) at an engineering strain rate of  $1 \times 10^{-4} \text{ s}^{-1}$ . For some specimens tested in tension at room temperature, changes in electrical resistivity during deformation were monitored by interrupting tensile tests at various stages of deformation. Deformation markings on specimen surfaces were examined by optical microscopy, scanning electron microscopy (SEM; JEOL JEM-7001FA operated at 20 kV) and atomic force microscopy (AFM; Shimadzu SPM-9600). Dislocation structures were examined by transmission electron microscopy (TEM) with a JEOL JEM-2000FX electron microscope operated at 200 kV. Thin foils for TEM observations were prepared by electro-polishing in a solution of nitric acid, ethylene glycol and methanol (2:5:20 by volume).

TEM and scanning transmission electron microscopy (STEM; JEOL JEM-ARM200F electron microscopes operated at 200 kV) as well as synchrotron x-ray diffraction (SPring-8, BL02B1 beam line) were further utilized to gain information about atomic arrangements in single-crystal specimens subjected to various heat-treatments designed to suppress or promote short-range ordering.

### 3.3 Results

#### 3.3.1 Electrical resistivity

Equiatomic Cr-Co-Ni polycrystals were first quenched from 1473 K and then isothermally annealed for various times at temperatures ranging from 573 to 973 K. Their normalized room-temperature electrical resistivities ( $R/R_0$ ) are plotted in Fig. 3.1(a) as a function of annealing time, where  $R_0 = 0.028161 \pm 0.00006 \text{ } \Omega$  is the electrical resistivity of specimens quenched from 1473 K. While no significant change in electrical resistivity occurs during isothermal annealing at 573 K, it increases gradually and reaches a saturation value at the other temperatures investigated, 673-973 K. The time required to reach the saturation value is shorter at higher temperatures, but the saturation value is higher at lower temperatures. Saturation already occurs after 0.05 hours at 973 K whereas the resistivity (and implied SRO) continues to increase even after 500 hours at 673 K. This behavior is consistent with SRO evolution in many FCC alloys such as Cu-Au [18], Ni-Cr [49] and Cu-Pd [50] alloys. For the equiatomic Cr-Co-Ni polycrystals, the largest saturation value obtained at 673 K is greater than  $R_0$  by  $\sim 4.8\%$ . This increment in electrical resistivity associated with SRO is comparable to those reported for Ni-Cr alloys ( $\sim 3\%$  at 673 K) [49] and Cu-Pd alloys ( $\sim 7\%$  at 523 K) [50] but is larger than that reported

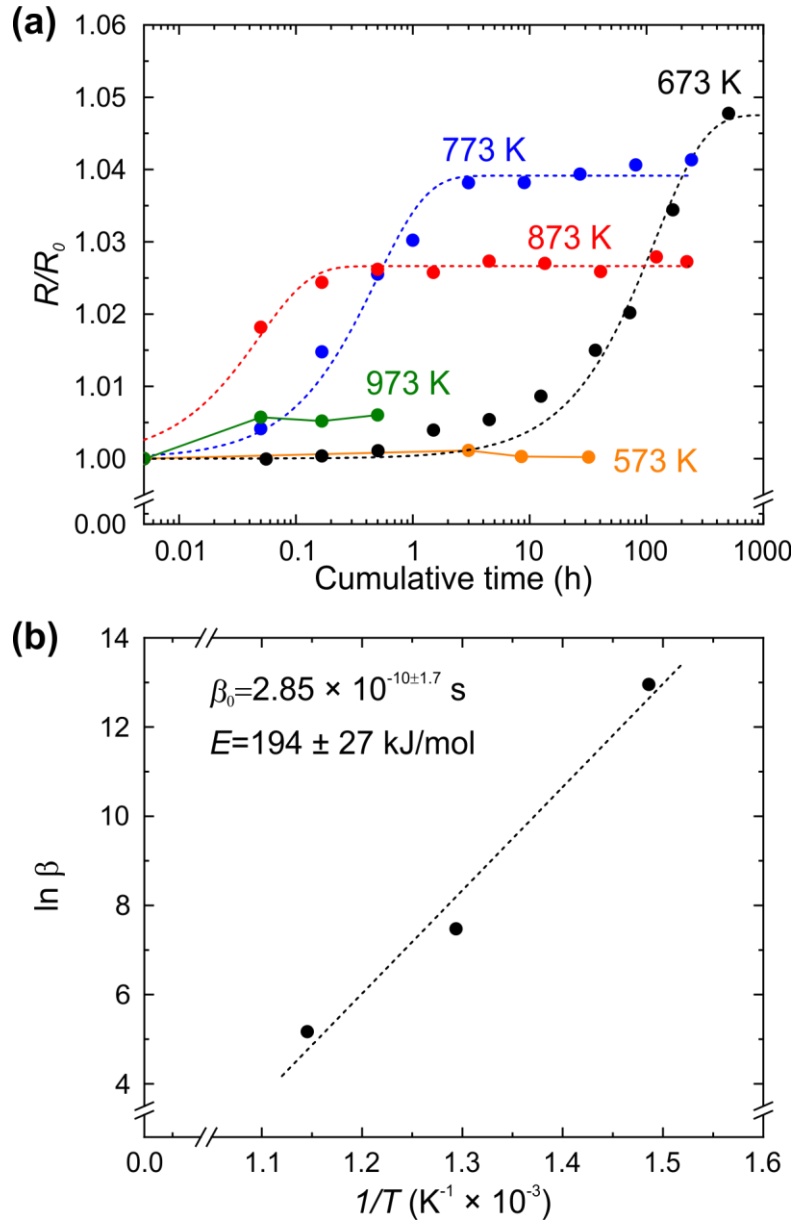


**Fig. 3.1** (a) Variations in electrical resistivity of the equiatomic Cr-Co-Ni polycrystals quenched from 1473 K during isothermal annealing at various temperatures in a range from 573 to 973 K. (b) Arrhenius plot of relaxation time  $\beta$  for resistivity change by isothermal annealing.

for Cu-Au alloys ( $\sim 1\%$  at 423 K) [18]. It is important to note that the increase in electrical resistivity after low-temperature (673-973 K) anneals is fully reversible, that is, the original value can be obtained by annealing at 1473 K followed by quenching. This reversibility strongly suggests that the formation of SRO indeed occurs by low-

temperature annealing and that electrical resistivity is a good way to monitor changes in the degree of SRO.

The time-dependent variation of electrical resistivity after isothermal annealing at 673, 773 and 873 K was fitted with the following equation,

$$R(t) / R_0 = 1 + \delta \{1 - \exp(-t / \beta)\} \quad (3-1)$$

where  $t$  is annealing time and  $\delta$  and  $\beta$  are constants depending on the annealing temperature. The results of fitting are tabulated in Table 3.1.

**Table 1.** Fitting parameters used to describe the equations (3-1) and (3-2).

Annealing temperature (K)	$\delta$	$\beta$ (s)	$\beta_0$ (s)	$E$ (kJ/mol)
673	0.04753	4.25E5		
773	0.03914	1.76E3	$2.85 \times 10^{-10 \pm 1.7}$	$194 \pm 27$
873	0.02663	1.75E2		

When the increase in resistivity reflects the volume of SRO formed and the constant  $\delta$  represents the fractional volume at saturation, eq. (3-1) can be regarded as an Avrami-type equation for the time dependence of SRO with Avrami index  $n = 1$  (needle-like growth). On the assumption that the behavior shown in Fig. 3.1(a) is controlled by atomic diffusion, the temperature dependence of  $\beta$  can be expressed with the following Arrhenius-type equation,

$$\beta = \beta_0 \exp(E / RT) \quad (3-2)$$

where  $\beta_0$  is a pre-exponential factor,  $R$  the ideal gas constant,  $T$  the absolute temperature and  $E$  the activation energy. The natural logarithm of  $\beta$  is plotted in Fig. 3.1(b) as a function of inverse temperature. The activation energy and pre-exponential factor

deduced from Fig. 3.1(b) are  $E=194 \pm 27$  kJ/mol and  $\beta_0=2.85 \times 10^{-10 \pm 1.7}$  s. The activation energy obtained from Fig. 3.1(b) is smaller than those (250-310 kJ/mol [51,52]) usually reported for atomic diffusion in HEAs and MEAs of the Cr-Mn-Fe-Co-Ni system. However, a recent tracer diffusion experiment indicates that atomic diffusion of Co and Ni below 1100 K occurs faster with smaller activation energies (206 and 185 kJ/mol) than what is expected from the extrapolation from high temperatures due presumably to the tendency for SRO formation in a Cr-Mn-Fe-Co-Ni alloy [53]. A similar diffusion behavior may occur also in the Cr-Co-Ni alloys at low temperatures due to SRO.

### **3.3.2 Observation of SRO**

#### **3.3.2.1 Electron and X-ray diffraction**

Selected-area electron diffraction (SAED) patterns with the [111] and [112] incidences taken from the single crystals water-quenched from 1473 K and subsequently annealed at 773 K for 168 hours are shown in Figs. 3.2(a), (b) and Figs. 3.3(a), (b), respectively. These two specimens were selected, based on Fig. 3.1(a), as representatives of the highest and lowest degrees of SRO, respectively. The specimen annealed at 773 K for 168 hours exhibits a greater than 4% increase in electrical resistivity, which is the highest among the curves in Fig. 3.1(a). In FCC solid-solutions, short-range ordering of the L1<sub>2</sub>- or L1<sub>0</sub>-type has been theoretically predicted [40,54,55] and experimentally verified [22,29,40,48] in the Cr-Co-Ni MEA and its related alloys. However, in the present study, no diffuse intensity indicative of SRO of the L1<sub>2</sub>- or L1<sub>0</sub>-type is observed at their superlattice reflection positions (for example at 1 $\bar{1}$ 0-type positions) in the SAED patterns (Figs. 3.2(a), (b) and Figs. 3.3(a), (b)), as seen in the intensity profile between

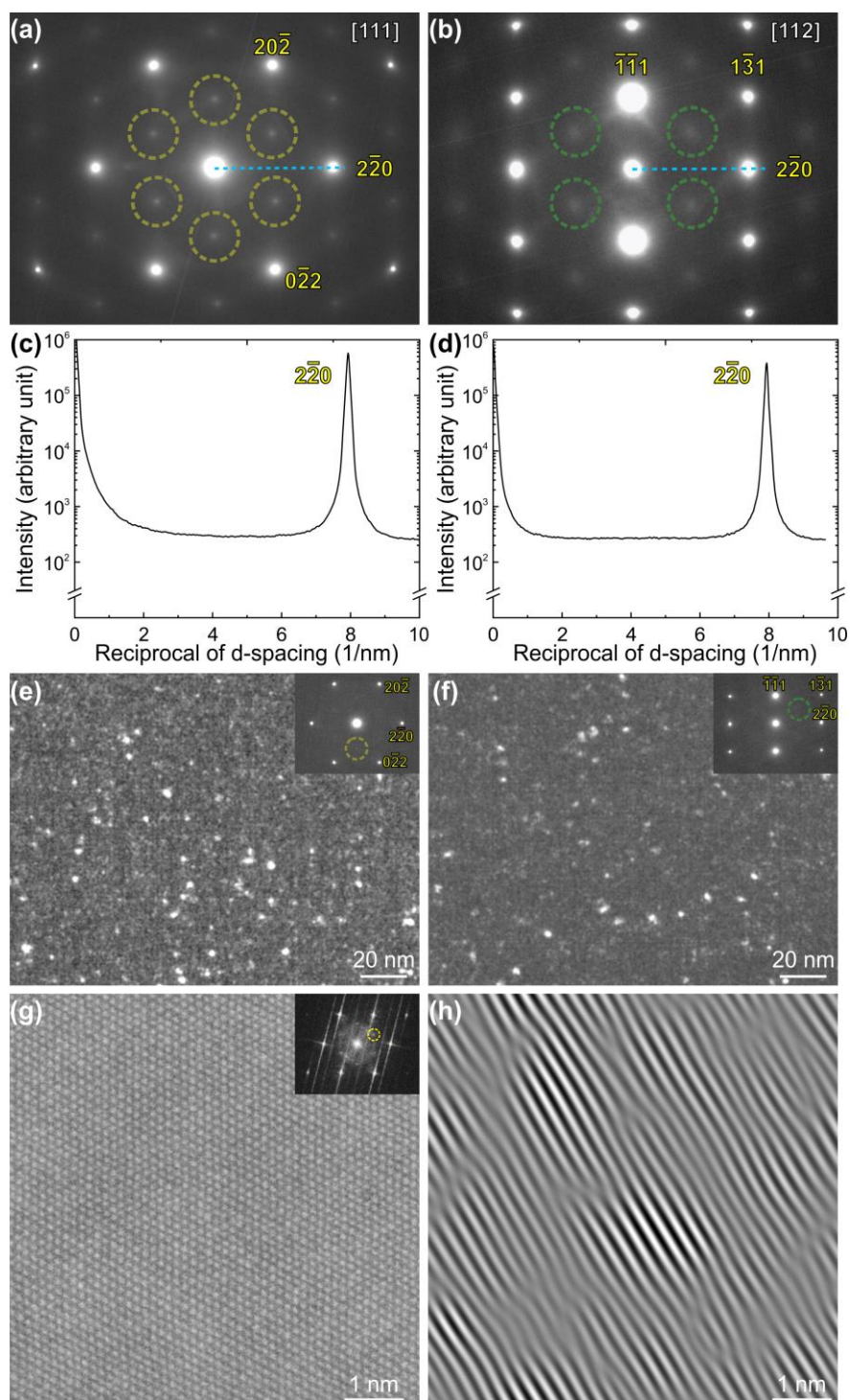


**Fig. 3.2** SAED patterns with the (a) [111] and (b) [112] incidences taken from the single crystals water-quenched from 1473 K. Intensity profile along a line between the transmitted beam and  $2\bar{2}0$  reflection in SAED patterns with (c) [111] and (d) [112] incidences. Dark-field images formed by setting an objective aperture at a position of (e)  $1/3\{422\}$  and (f)  $1/2\{113\}$  (as shown in the inset SAED patterns). (g) Atomic-resolution HAADF-STEM image taken along [111] with FFT diagram (inset). (h) Inverse FFT image formed with the diffuse intensities at  $1/3\{422\}$  position in the FFT diagram.

the transmitted beam and  $\bar{2}20$  reflection for both [111] incidence (Figs. 3.2(c) and Fig. 3.3(c)) and [112] incidence (Figs. 3.2(d) and Fig. 3.3(d)). This, however, does not rule out SRO of the  $L1_2$ - or  $L1_0$ -type in the Cr-Co-Ni MEA, in view of the very small difference in atomic scattering factor of the constituent elements, Cr, Co and Ni. Instead, some diffuse intensity is observed at positions of  $1/3\{422\}$  and  $1/2\{113\}$  respectively in the SAED patterns for [111] and [112] incidences, as marked with dotted circles in Figs. 3.2(a), (b) and Figs. 3.3(a), (b). However, no significant difference in the intensity of such diffuse scattering is observed between the two specimens in which significantly different degrees of SRO are expected. Many previous studies on SRO in FCC solid-solution alloys assume that the diffuse intensity at positions of  $1/3\{422\}$  and  $1/2\{113\}$  is an indication of the occurrence of SRO [37,45,56–58], although this has never been verified. Dark-field imaging by setting an objective aperture at a position of  $1/3\{422\}$  or  $1/2\{113\}$  reveals some small bright regions with sizes of 1~2 nm in diameter, however, without any significant difference between the two specimens (Figs. 3.2(e), (f) and Figs. 3.3(e), (f)).

Figs. 3.2(g) and Fig. 3.3(g) show, respectively, atomic-resolution high-angle annular dark-field (HAADF)-STEM images taken along [111] for single crystals water-quenched from 1473 K and subsequently annealed at 773 K for 168 hours. Although the intensity of each of the imaged atomic columns is known to be proportional to the square of the averaged atomic number of constituent elements in the relevant column, no particular atomic arrangement that may be related to SRO is observed in either specimen. This is understandable given the small difference in atomic numbers of Cr, Co and Ni. Fast Fourier transforms (FFT) of these HAADF-STEM images reveal diffuse intensities at  $1/3\{422\}$  positions (insets in Figs. 3.2(g) and Fig. 3.3(g)), as in the SAED patterns of Figs. 3.2(a) and Fig. 3.3(a). Inverse FFT images formed with these diffuse intensities at  $1/3\{422\}$

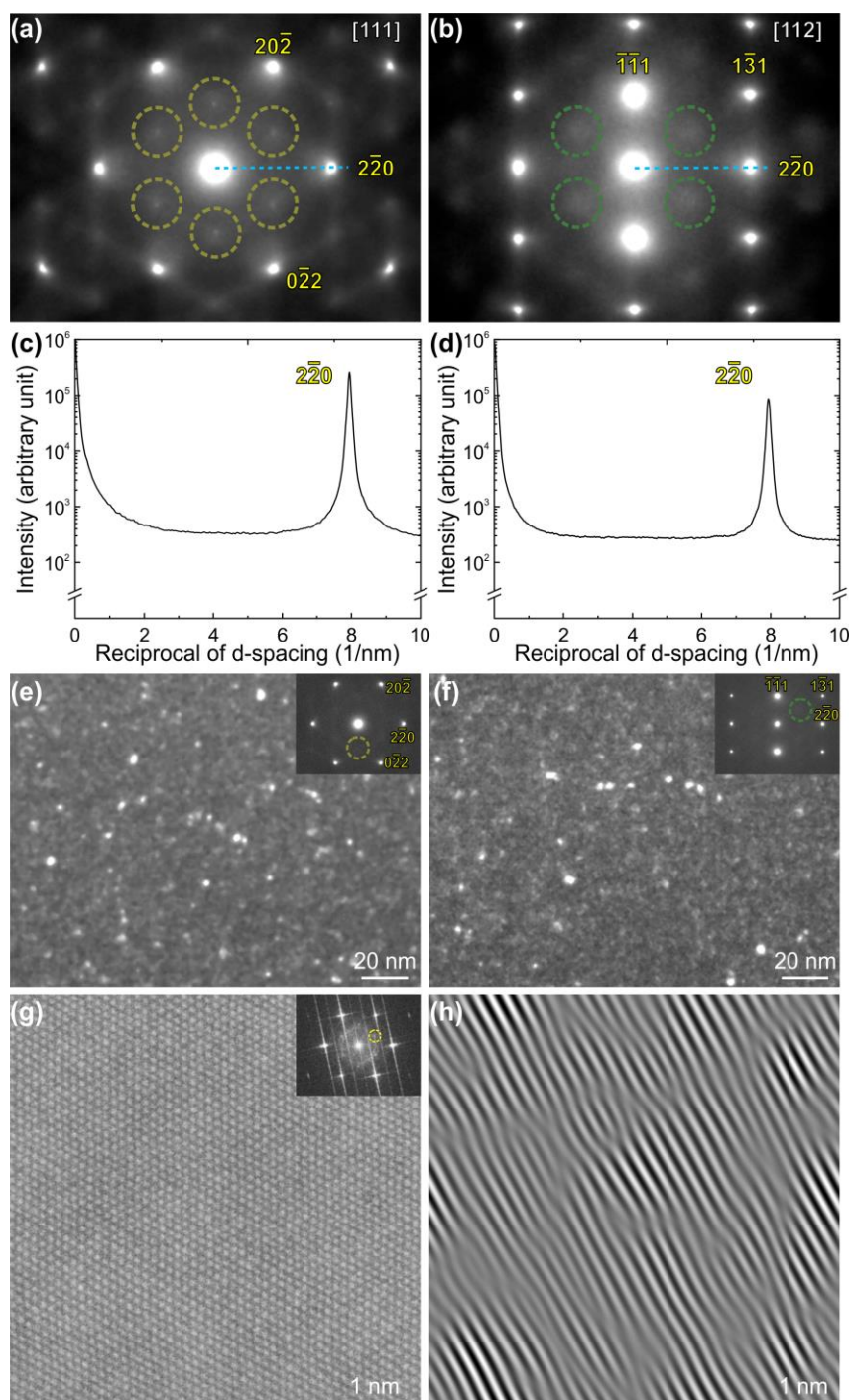


**Fig. 3.3** SAED patterns with the (a) [111] and (b) [112] incidences taken from the single crystals subsequently annealed at 773 K for 168 hours after water-quenching from 1473 K. Intensity profile along a line between the transmitted beam and  $2\bar{2}0$  reflection in SAED patterns with (c) [111] and (d) [112] incidences. Dark-field images formed by setting an objective aperture at a position of (e)  $1/3\{422\}$  and (f)  $1/2\{113\}$  (as shown in the inset SAED patterns). (g) Atomic-resolution HAADF-STEM image taken along [111] with FFT diagram (inset). (h) Inverse FFT image formed with the diffuse intensities at  $1/3\{422\}$  position in the FFT diagram.

positions exhibit scattered small bright regions with sizes of 1~2 nm in diameter but, again, without any significant difference between the two specimens (Figs. 3.2(e), (f) and Figs. 3.3(e), (f)). Zhou et al. [37] claimed that the occurrence of  $1/2\{311\}$  diffuse intensity in the [112] SAED is clear evidence of SRO in Cr-Co-Ni subjected to annealing at 873 K for 1 hour and that the small regions revealed by inverse FFT imaging with such diffuse scattering correspond to short-range ordered domains. Similar claims were made also for Al-Cr-Co-Ni [58], Cr-Mn-Fe-Co [45] and V-Co-Ni [57] MEAs. However, neither the diffuse intensities at positions of  $1/3\{422\}$  and  $1/2\{113\}$  nor the sizes of the small regions revealed by dark-field TEM imaging and by inverse FFT of atomic-resolution HAADF-STEM images (presumed to be short-range ordered domains) vary when the electrical resistivity changes, i.e., they do not depend on the degree of SRO, as seen in Figs. 3.2 and 3.3. This calls into question about the correlation between diffuse intensities at positions of  $1/3\{422\}$  and  $1/2\{113\}$  in diffraction patterns and SRO in the Cr-Co-Ni MEA.

Indeed, even in Cu, a pure FCC element, diffuse intensity is observed at positions of  $1/3\{422\}$  and  $1/2\{113\}$  in SAED patterns with the [111] and [112] incidences (Fig. S3.2(a) and (b)) and dark-field imaging with these diffuse intensities reveals some small bright regions (Fig. S3.2(e) and (f)) not unlike those seen in the Cr-Co-Ni MEA. There is a long history of these diffuse intensities being attributed to factors other than SRO, such as thin film effects ( $\{111\}$  relrod spiking from the first-order Laue zone (FOLZ) into the zero-th layer), surface steps, incorporation of defects on  $\{111\}$  (stacking faults, twins and HCP layers) and so on [59–65]. In view of the very small difference in atomic scattering factor of the constituent elements of the Cr-Co-Ni MEA, it is strongly suspected that the occurrence of diffuse scattering at  $1/3\{422\}$  and  $1/2\{113\}$  positions in the SAED patterns in the Cr-Co-Ni MEA is due mainly to thin film effects ( $\{111\}$  relrod spiking) and surface

steps rather than SRO. In fact, no diffuse intensities are present at these positions in the synchrotron x-ray diffraction patterns (Fig. S3.3). This clearly indicates that the development of SRO in the Cr-Co-Ni MEA cannot be monitored by simple x-ray and electron diffraction experiments.

### **3.3.3 Mechanical properties**

#### **3.3.3.1 Yield stress in compression and tension**

The deformation behavior of single crystals of the equiatomic Cr-Co-Ni alloys changes with electrical resistivity (i.e., the degree of SRO) upon annealing was investigated. Fig. 3.4 shows the temperature and time dependence of the critical resolved shear stress (CRSS) for (111) slip. Values of CRSS were calculated from the yield stresses defined as the 0.2% flow stress multiplied by the Schmid factor (0.467) of the  $[\bar{1}23]$  orientation. CRSS values for (111) slip obtained at room temperature in compression and tension, and at 77 K in compression are plotted in Fig. 3.4(a) as a function of annealing temperature (after first annealing at 1473 K for 168 hours and water quenching). All these specimens were annealed at the indicated temperatures for the same length of time (168 hours), followed by water-quenching prior to mechanical testing. The CRSS values at room temperature and 77 K (65 and 133 MPa, respectively [66]) obtained previously in compression for specimens quenched from 1473 K after annealing for 168 hours are indicated with a dotted line in Fig. 3.4(a). After 168 hours, the degree of SRO is expected to be the largest for the 773 K anneal, followed by the 673 and 873 K anneals, according to the electrical resistivity changes shown in Fig. 3.1(a). However, the CRSS values at both room temperature and 77 K do not change significantly with annealing temperature, furthermore, all the CRSS values are comparable to those of specimens quenched from

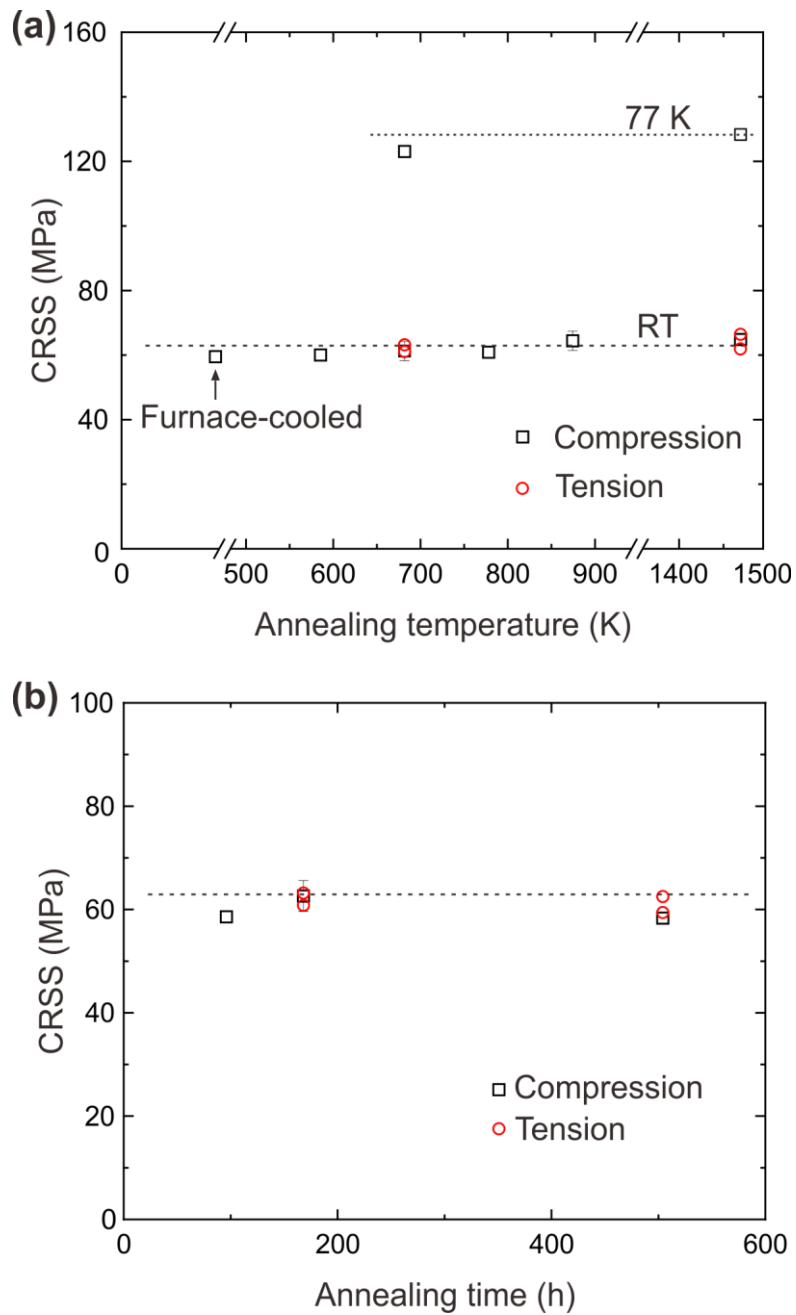


**Fig. 3.4** (a) CRSS values for (111) slip obtained for  $[\bar{1} 23]$ -oriented single crystals of the equiatomic Cr-Co-Ni MEA at room temperature in compression and tension and at 77 K in compression plotted as a function of subsequent annealing temperature (for 168 h) after quenching from 1473 K. (b) CRSS values for (111) slip obtained at room temperature in compression and tension for  $[\bar{1} 23]$ -oriented single crystals of the equiatomic Cr-Co-Ni MEA quenched from 1473 K plotted as a function of isothermal annealing time at 673 K.

1473 K. Note that no significant change in CRSS is observed also for specimens furnace-cooled from 1273 K (at a rate of 100 K/hour). This result is in contrast to an earlier paper

[43] on polycrystalline Cr-Co-Ni that reported a 25% yield stress increase in specimens aged at 1273 K for 120 h and furnace-cooled relative to their unaged and water-quenched counterparts despite the aged specimens having a larger grain size (i.e., lower Hall-Petch strengthening).

Effects of isothermal annealing at 673 K on the CRSS at room temperature both in tension and compression was also investigated, as shown in Fig. 3.4(b). 673 K is employed as the isothermal annealing temperature as there is a large change in electrical resistivity at this temperature and the change occurs very gradually (Fig. 3.1(a)). The dotted line in the figure is the CRSS value obtained in compression for specimens quenched from 1473 K after annealing for 168 hours. The CRSS values obtained in compression and tension at room temperature are, again, all comparable with that for specimens quenched from 1473 K, and they do not change significantly with annealing time at 673 K, although the degree of SRO must change gradually but significantly to the highest level after 504 hours as indicated by the greater than 4% electrical resistivity increase under these conditions (Fig. 3.1(a)).

It is thus concluded that the degree of SRO does not affect significantly the CRSS value for (111) slip in the equiatomic Cr-Co-Ni MEA. This conclusion is consistent with what is observed for Cu-Al [32] and Cu-Au alloys [18,20] and also for the Cr-Mn-Fe-Co-Ni HEA [46] and Cr-Co-Ni MEA [42], but is in contrast to most theoretical predictions [13,14,39,41,44] and to the report by Zhang et al. [43] that the yield strength increased by 25% due to SRO in polycrystals of Cr-Co-Ni after furnace-cooling from 1273 K.

### **3.3.3.2 Dislocation structures**

Dislocation structures revealed by bright-field and weak-beam dark-field imaging in  $[\bar{1}23]$ -oriented single crystals are shown in Figs. 3.5 (a), (b) for specimens water-

quenched from 1473 K, and Figs. 3.5(d), (e) for specimens water quenched and subsequently annealed at 773 K for 68 hours. These two conditions are selected as representatives of the lowest and highest SRO respectively, similar to those used for TEM observations, Figs. 3.2 and 3.3. Both specimens were compressed at room temperature to about 3% plastic strain, and a thin foil was cut parallel to the (111) macroscopic slip plane. In both specimens, typical planar arrays of smoothly curved long dislocations are observed on the (111) slip planes in the bright-field images, Figs. 3.5(a) and (d). Although the dominance of screw dislocations upon SRO strengthening is theoretically predicted [67], no significant change in dislocation alignment along particular orientations was noted after SRO formation in the equiatomic Cr-Co-Ni MEA. The observed planar array of dislocations is consistent with a low stacking fault energy of the alloy, as evident from the large separation distance between paired Shockley partial dislocations in the weak-beam images of Figs. 3.5(b) and (e). The separation distance between paired Shockley partial dislocations was measured as a function of angle  $\theta$  between the Burgers vector and line direction of the perfect dislocations in Figs. 3.5(c) and (f) to deduce the stacking fault energy of the two alloys. Although the dissociation widths in both alloys exhibit scatter, they are in the range of those reported for pure Cu [68], Ag [69] and for the Cr-Mn-Fe-Co-Ni HEA [46,70,71]. On top of that, the magnitude of the scatter is similar for these two alloys (one quenched from 1473 K and the other subsequently annealed at 773 K) and does not change much after annealing at 773 K. This contrasts with what is predicted from theoretical calculation for alloys with SRO, in which a significant variation in dissociation width is predicted in the presence of local SRO [13,14]. From the orientation

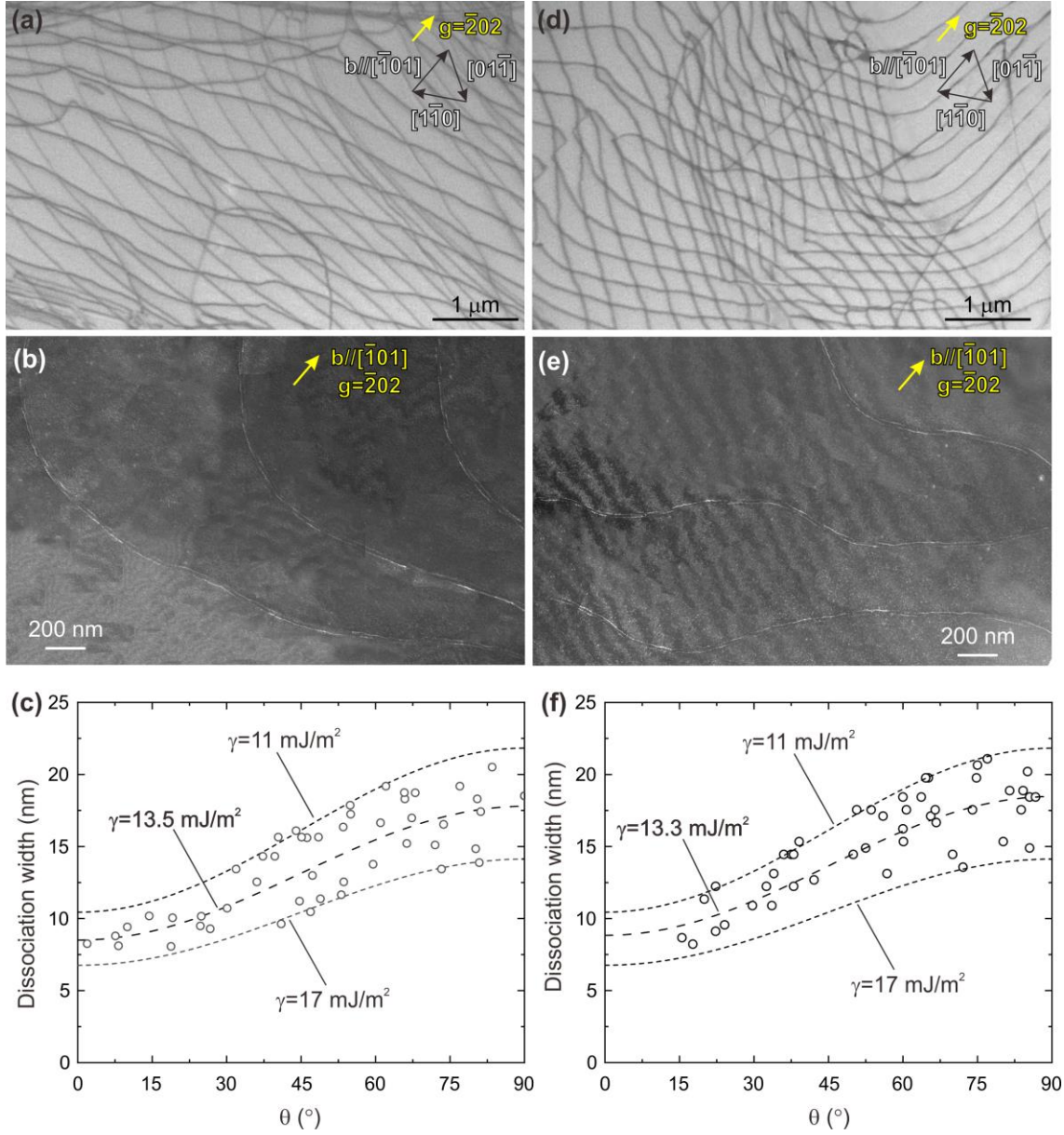


**Fig. 3.5** Dislocation structures revealed by (a), (d) bright-field and (b), (e) weak-beam dark-filed imaging for  $[\bar{1}23]$ -oriented single crystals (a), (b) water-quenched from 1473 K and (d), (e) subsequently annealed at 773 K for 168 hours. Separation distance between paired Shockley partial dislocations were measured as a function of angle  $\theta$  between the Burgers vector and line direction of the perfect dislocations for  $[\bar{1}23]$ -oriented single crystals (c) water-quenched from 1473 K and (f) subsequently annealed at 773 K for 168 hours.

dependence of dissociation width, the stacking fault energy is deduced to be  $13.5\ \text{mJ/m}^2$  for the Cr-Co-Ni MEA water-quenched from 1473 K and  $13.3\ \text{mJ/m}^2$  for the same alloy subsequently annealed at 773 K for 68 hours. This indicates that the stacking fault energy

is virtually unchanged with the development of SRO in the equiatomic Cr-Co-Ni MEA. Our finding here is consistent with the previous finding in Cr-Mn-Fe-Co-Ni [46] but at odds with the paper by Zhang et al. [43] in which the stacking fault energy of the equiatomic Cr-Co-Ni MEA was reported to increase significantly from 8 mJ/m<sup>2</sup> after water quenching to 23 mJ/m<sup>2</sup> after furnace-cooling from 1273 K and attributed to increased SRO in the latter condition.

### **3.3.3.3 Yield drop, electrical resistivity change and slip localization in tension**

In some dilute FCC alloys, a noticeable yield drop is believed to emerge in the tensile stress-strain curve accompanied by localized (coarse and planar) slip bands as a result of SRO [17,32]. This is believed to be due to the quick dissipation of the SRO-induced high resistance to dislocation motion by the passage of the first several dislocations that destroy SRO on the slip plane, so that subsequent dislocations move on the same slip plane experiencing less resistance, thereby forming coarse slip bands [32]. To check whether this is also the case for the equiatomic Cr-Co-Ni MEA, the magnitude of yield drop and slip localization behavior with the use of  $[\bar{1}23]$ -oriented single crystals water-quenched from 1473 K and subsequently annealed at 673 K for 168 or 504 hours were investigated. The increments in electrical resistivity for the latter two specimens are 3.4 and 4.8%, respectively.

Tensile stress-strain curves obtained at room temperature for these specimens are shown in Fig. 3.6(a) up to the end of stage I. Yield drop occurs for all specimens but in a rather wide range of plastic strain (usually exceeding several percent of engineering strain) so that the stress-strain curve in stage I exhibits a concave upward shape without a plateau.

This is different from the behavior observed for some conventional dilute FCC alloys, in which a sharper yield drop occurs (within a few percent of plastic strain), followed by a

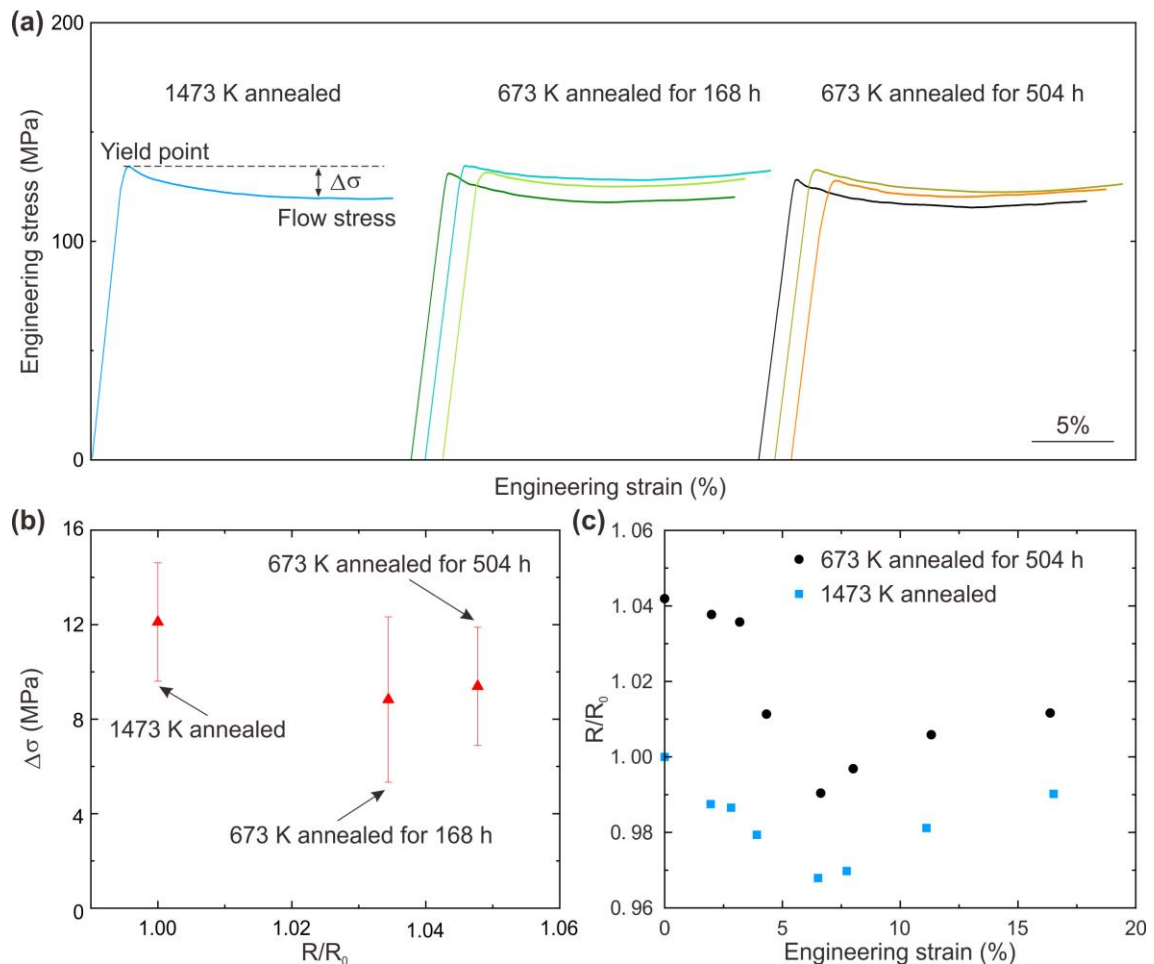


**Fig. 3.6** Tensile stress-strain curves up to the end of stage I obtained at room temperature for  $[\bar{1}23]$ -oriented single crystals water-quenched from 1473 K and subsequently annealed at 673 K for 168 and 504 hours. (b) Magnitude of yield drop measured for these three different specimens from (a). (c) Variations of electrical resistivity for  $[\bar{1}23]$ -oriented single crystals water-quenched from 1473 K and subsequently annealed at 673 K for 504 hours measured as a function of plastic strain in stage I in tensile deformation.

plateau stress [17,18,32,33]. In the present study, the yield drop is defined as the difference between the upper yield stress and lowest flow stress in stage I. The magnitudes of the yield drop estimated from the tensile stress-strain curves in Fig. 3.6(a) are  $12.11 \pm 2.5$ ,  $8.83 \pm 3.5$  and  $9.39 \pm 2.5$  MPa for single crystals water-quenched from 1473 K,

and water-quenched and subsequently annealed at 673 K for 168 and 504 hours, respectively. The degree of SRO (as determined by the increment in electrical resistivity) does not correlate with the extent of yield drop in the equiatomic Cr-Co-Ni MEA (Fig. 3.6(b)). This is consistent with the result reported by Büttner [18] and Kuhlmann [20] for Cu-Au alloys but is in contrast to what is observed for conventional dilute FCC alloys [17,32].

Changes in electrical resistivity during tensile deformation in stage I by conducting interrupted tensile tests at room temperature for  $[\bar{1}23]$ -oriented single crystals water-quenched from 1473 K and subsequently annealed at 673 K for 504 hours were also investigated, as shown in Fig. 3.6(c). As in Fig. 3.1(a), values plotted in Fig. 3.6(c) are all normalized to the value ( $R_0$ ) of electrical resistivity obtained after quenching from 1473 K. That is why the starting value of electrical resistivity is 1.04 for the specimen subsequently annealed at 673 K for 504 hours, while it is 1 for the specimen water-quenched from 1473 K. Because of the dislocations introduced during deformation (and stored in the specimen), the electrical resistivity is generally expected to increase as deformation proceeds. In the equiatomic Cr-Co-Ni MEA, however, the resistivity first decreases, exhibiting a minimum at an engineering strain of 6~7%, followed by an increase at higher strains for both specimens. The strain level for the minimum flow stress almost coincides with that for the minimum electrical resistivity for both specimens. The decrease in electrical resistivity at the minimum is about 3% for the single crystal water-quenched from 1473 K, while it is a bit larger, 4%, for the single crystal subsequently annealed at 673 K for 504 hours. The decrease in electrical resistivity following deformation (i.e., by dislocation introduction) together with the decrease in electrical

resistivity by low-temperature annealing is usually called the K-effect [22,72]. It is usually thought to be caused by a special atom arrangement of the SRO-type [22] where the decrease in electrical resistivity in the early stages of deformation occurs via the destruction of SRO by the motion of dislocations. If this is the case for the equiatomic Cr-Co-Ni MEA, single crystals water-quenched from 1473 K, as well as those subsequently annealed at 673 K for 504 hours, both contain some degree of SRO prior to deformation. Additionally, this SRO is destroyed by the motion of dislocations, and the decrease in the degree of SRO is larger for the single crystal subsequently annealed at 673 K for 504 hours because of its higher initial degree of SRO. However, the initial degree of SRO in the single crystals water-quenched from 1473 K may not be very high since its electrical resistivity is comparable to that of specimens quenched from the liquid state in which the degree of SRO is expected to be minimized.

Step heights of the deformation markings formed in the very early stages of plasticity were investigated by optical and atomic force microscopy to evaluate how the development of SRO affects slip localization behaviors. To that end,  $[\bar{1}23]$ -oriented single crystals water-quenched from 1473 K as well as those subsequently annealed at 673 K for 504 hours were examined, as shown in Fig. 3.7. The specimen geometry for optical and atomic force microscopy observations is depicted in Fig. S3.4. The observations were made (1) at a very small strain level ( $\sim 0.4\%$  plastic strain) corresponding to the peak stress of the upper yield point, and (2) at a strain level corresponding to about 1% additional plastic strain at the same position in both specimens. The densities of slip bands revealed by optical microscopy are almost identical for the two specimens at the same strain levels in spite of the different degrees of SRO. In both

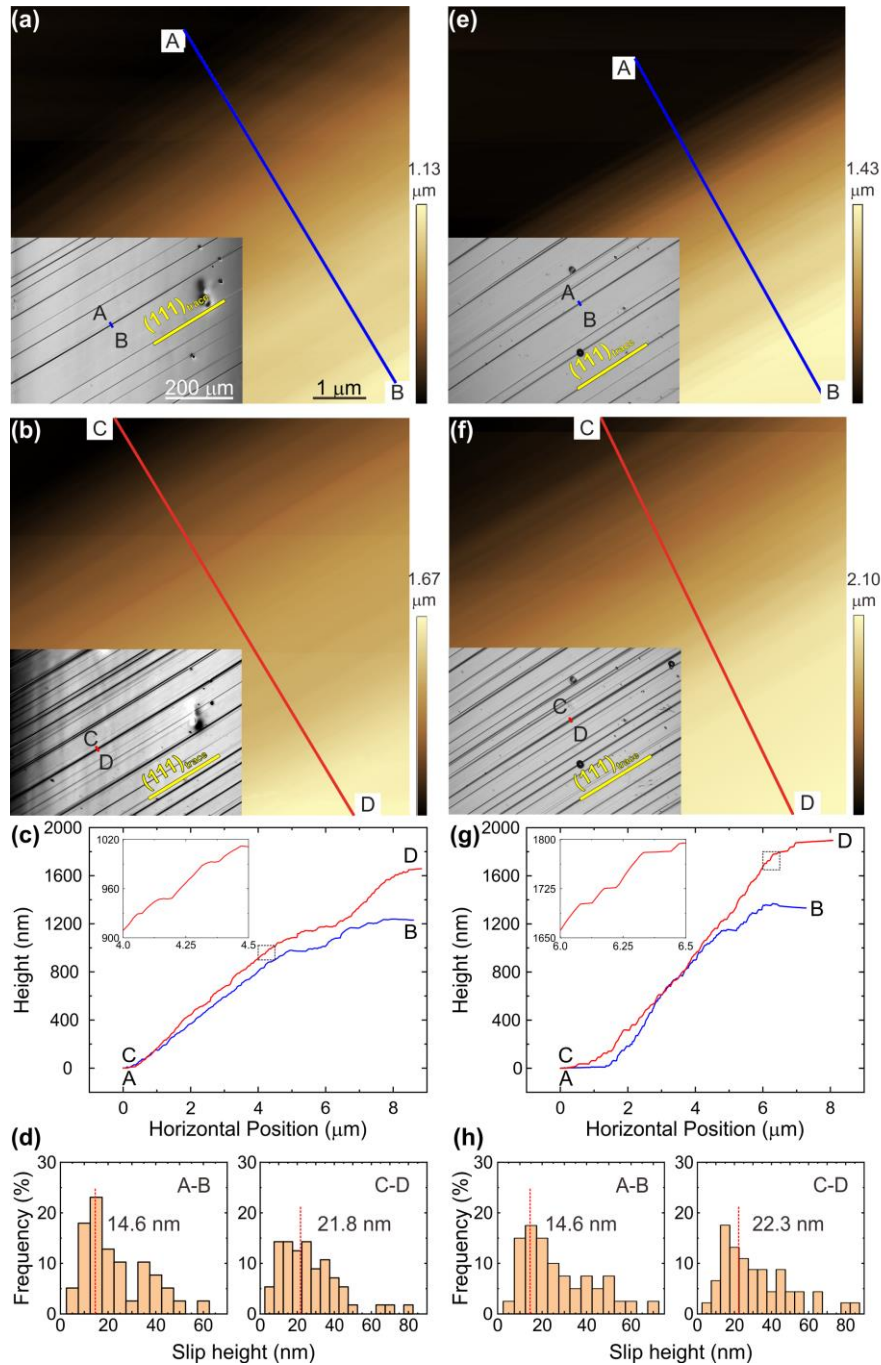


**Fig. 3.7** Deformation markings revealed by optical and atomic force microscopy in the  $(54\bar{1})$  surface of  $[\bar{1}23]$ -oriented single crystals (a), (b) water-quenched from 1473 K and (e), (f) subsequently annealed at 673 K for 504 hours (a), (e) at a very small strain level ( $\sim 0.4\%$  plastic strain) corresponding to the peak stress of upper yielding and (b), (f) at a strain level with about 1% additional plastic strain. Height variation diagrams measure by atomic force microscopy along A-B and C-D and histograms of slip heights formed from the height variation diagrams are shown for (c), (d)  $[\bar{1}23]$ -oriented single crystals water-quenched from 1473 K and for (g), (h) those subsequently annealed at 673 K for 504 hours.

specimens, new slip bands are observed to form between existing slip bands as deformation proceeds, in spite of the decreasing flow stress. This clearly indicates that the emergence of yield drop is not necessarily related to the quick decay of the SRO-induced high resistance to dislocation motion by the passage of the first several dislocations during the formation of a new slip band/line [32]. Atomic force microscopy revealed that a slip band optically observed as a single line actually consists of a number of slip steps parallel to (111), as seen in the height variation diagrams of Figs. 3.7(c) and (g). Comparison of the diagrams along AB and CD in Figs. 3.7(c) and (g) clearly indicates that, in addition to incremental slip at existing slip lines in the band, widening of the slip band also occurs by forming adjacent slip lines in both specimens. From Figs. 3.7(c) and (g), histograms of slip heights can be determined, which are plotted in Figs. 3.7(d) and (h). The averaged slip heights are almost identical for the two specimens at the same strain levels. For both specimens, the average slip height increases from 16 nm to 22 nm during 1% additional plastic strain in stage I. These average slip heights in the Cr-Co-Ni MEA are comparable to those observed in stage I for FCC alloys with a low stacking fault energy (27 nm for Cu-19 at.% Zn and 24 nm Cu-30 at.% Zn [73]). These results indicate that the development of SRO does not significantly affect the slip localization behavior in the Cr-Co-Ni MEA. This is in contrast to what is believed to occur in the presence of SRO in some conventional dilute FCC alloys [17,32,73,74].

#### **3.3.3.4 Deformation at large strain levels in tension**

Fig. 3.8(a) shows engineering stress-strain curves obtained in tension at room temperature for  $[\bar{1}23]$ -oriented single crystals of the Cr-Co-Ni MEA: one water-quenched from 1473 K and the other subsequently annealed at 673 K for 504 hours. The

stress-strain curve for the specimen water-quenched from 1473 K is from the previous study [66] where it was deformed until failure occurred. Two inflection points are evident in the stress-strain curve, following stage II (linear work-hardening). The first inflection point at about 150% strain corresponds to the end of overshooting (i.e., the change in the dominant slip system from the (111)  $[\bar{1}01]$  primary slip system to the  $(\bar{1}\bar{1}1)[011]$  conjugate slip system), and the second point corresponds to the change in the dominant deformation mode from  $(\bar{1}\bar{1}1)[011]$  conjugate slip to (111)  $[\bar{2}11]$  primary twinning [66]. In this study, the tensile test for the single crystal subsequently annealed at 673 K for 504 hours was interrupted at a strain level of 220% immediately after the second inflection point for detailed observations of deformation microstructures. Although the degree of SRO in the two specimens is expected to be significantly different based on their different resistivities, their tensile stress-strain curves are quite similar to each other. The yield stress, length of stage I, the stress and strain levels at which the first and second inflection points occur are all virtually the same for the two specimens despite their different degrees of SRO. This indicates that the deformation behavior does not vary significantly with degree of SRO not only in the early stages of deformation (as described in the previous sections) but also after large strains. In fact, as in the water-quenched single crystal, the second inflection point in the single crystal annealed at 673 K for 504 hours also corresponds to the onset of (111)  $[\bar{2}11]$  primary twinning, Figs. 3.8(d) and (e). The thickness and volume fraction of twins are virtually the same as those of the single crystal water-quenched from 1473 K (Figs. 3.8(b) and (c)), when compared at similar strain levels. The true stresses for the onset of twinning are  $995 \pm 30$  MPa for the single crystal water-quenched from 1473 K and  $991 \pm 70$  MPa for that subsequently annealed at 673 K

for 504 hours. Consequently, the twinning shear stresses calculated using the corresponding Schmid factor (0.409) [66] are also similar,  $407 \pm 12$  MPa and  $405 \pm 29$  MPa. This is a clear indication that the twinning behavior does not vary significantly with the degree of SRO.

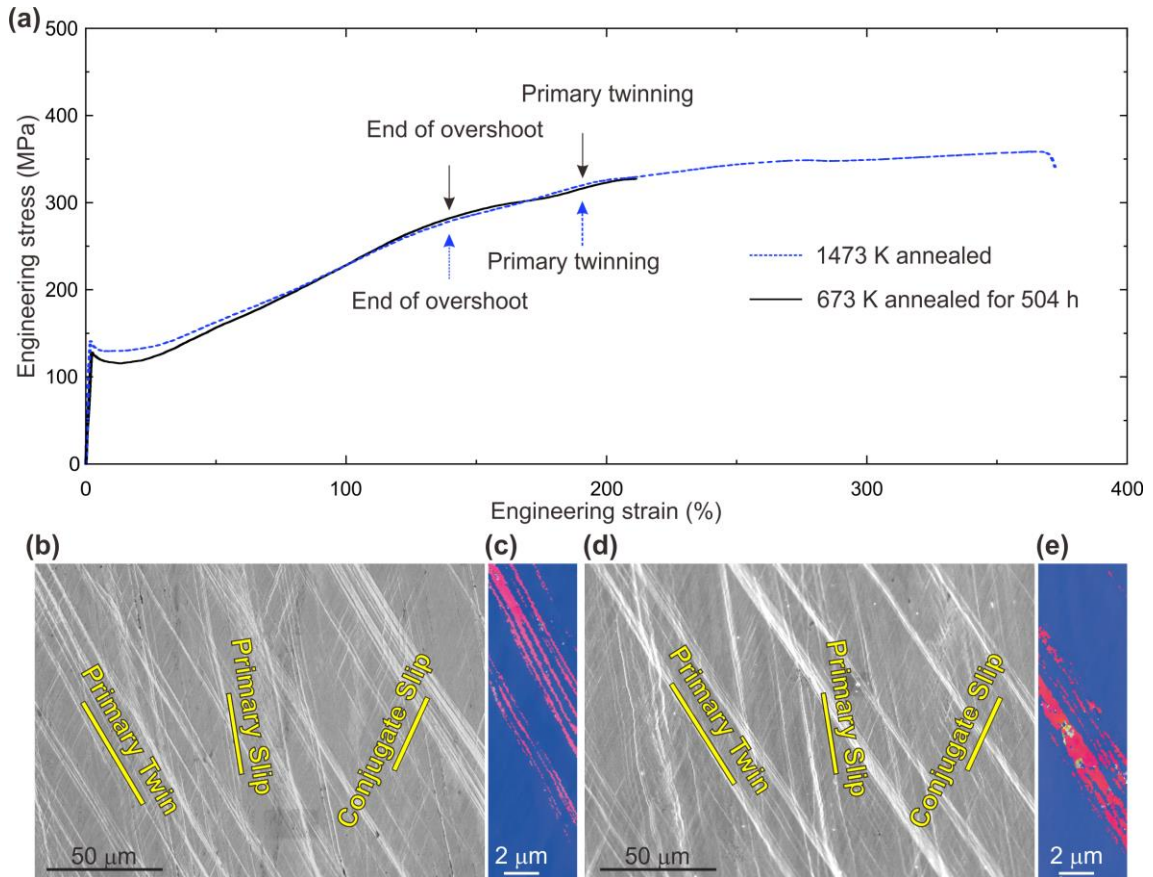


**Fig. 3.8** (a) Tensile stress-strain curves obtained in tension at room temperature for  $[\bar{1}23]$ -oriented single crystals water-quenched from 1473 K and subsequently annealed at 673 K for 504 hours. (b), (d) Optical micrographs and (c), (e) EBSD maps to show deformation twinning are taken from  $[\bar{1}23]$ -oriented single crystals (b), (c) water-quenched from 1473 K and (d), (e) subsequently annealed at 673 K for 504 hours.

## 3.4 Discussion

### 3.4.1 Evidence of the existence of SRO

Using electron diffraction and HAADF-STEM imaging Zhang et al. [43] reported SRO in equiatomic Cr-Co-Ni MEA polycrystals after annealing at 1273 K followed by furnace cooling. They described that SRO in the equiatomic Cr-Co-Ni MEA polycrystals is detected as streaks elongated along the  $\langle 111 \rangle$  directions [43]. On the other hand, Zhou et al. [37] associated SRO in the equiatomic Cr-Co-Ni MEA with diffuse intensity at the  $1/2\{113\}$  positions in SAED patterns with the  $\langle 112 \rangle$  incidence. Here streaks along  $\langle 111 \rangle$  but diffuse intensity at positions of  $1/3\{422\}$  and  $1/2\{113\}$  in the SAED patterns for  $[111]$  and  $[112]$  incidences were observed. However, these diffuse intensities did not change significantly with degree of SRO. Additionally, such diffuse intensities can also be due to other factors such as thin film effects ( $\{111\}$  re-rod spiking) and/or surface steps parallel to  $\{111\}$ . The above factors, along with the very small difference in atomic scattering factors of Cr, Co and Ni, make it very difficult to obtain unambiguous evidence for SRO in the Cr-Co-Ni MEA by x-ray and electron diffraction methods.

In contrast, electrical resistivity measurements seem to offer a suitable way to detect SRO in the equiatomic Cr-Co-Ni MEA in a fairly quantitative manner. Recent kinetic Monte-Carlo calculations using potentials generated by neural networks by Ogata et al. [75] have predicted that the changes in the Warren-Cowley parameters of the equiatomic Cr-Co-Ni MEA upon aging are very similar to the changes in electrical resistivity shown in Fig. 3.1(a) with the saturated Warren-Cowley parameter  $\alpha_{Cr-Co}$  reaching a value of 0.217 at 700 K. Although the degree of SRO is expected to correlate well with changes in electrical resistivity, a linear correlation between the two has yet to

be proven. A lattice contraction is predicted to accompany SRO in some MEAs including the equiatomic Cr-Co-Ni MEA by DFT calculations [44]. And, indeed, a decrease in the lattice constant was observed from 0.35666 nm (for samples quenched from 1473 K) to 0.35662 nm (for those subsequently annealed at 673 K for 168 hours), and then to 0.35648 nm (for those subsequently annealed at 673 K for 504 hours). Interestingly, the lattice constant returns to the original value upon re-annealing at 1473 K, consistent with a similar recovery of electrical resistivity. This is further evidence of SRO in the equiatomic Cr-Co-Ni MEA.

### 3.4.2 Microstructural evolution accompanying SRO

Some alloys like those in the Ni-Cr [49] and Ni-Mo [76] systems are known to exhibit the so-called K-effect [72] that is believed to be closely related to SRO. The increased electrical resistivity during low-temperature annealing is attributed to the formation of small Ni<sub>3</sub>Cr- or Ni<sub>2</sub>Cr-like clusters in Ni-Cr alloys [49] and to the formation of SRO of the L<sub>12</sub>-type in a Ni-Al-Fe alloy [22]. Theoretical calculations have indicated that the increased resistivity after low-temperature annealing in, for example, Ni-Cr [77] and Ni-Mo [76] alloys, is due to the formation of a local atomic arrangement in which a Cr (or Mo) atom is preferentially surrounded by Ni atoms, i.e., Ni<sub>3</sub>Cr cluster of the L<sub>12</sub>-type. It is postulated that the formation of small Ni<sub>3</sub>Cr clusters (or (Ni,Co)<sub>3</sub>Cr clusters in the case of the Cr-Co-Ni MEA) of the L<sub>12</sub>-type causes the increase in electrical resistivity observed after low-temperature annealing in the equiatomic Cr-Co-Ni MEA (Fig. 3.1(a)).

From Fig. 3.1 the size and volume fraction of the small clusters are estimated in which a higher degree of SRO of the (Ni,Co)<sub>3</sub>Cr-type is expected. The preexponential factor  $\beta_0$  ( $2.85 \times 10^{-10 \pm 1.7}$  s) is much longer than the mean time for monoatomic jump

(i.e., atomic jump to the nearest neighbor site, or the inverse of the lattice vibration frequency) of about  $\beta_{mono} = 10^{-13}$  s and can be considered approximately as the cumulative number of atom jumps required for the formation of small clusters with a higher degree of SRO. Then, the ratio  $\frac{\beta_0}{\beta_{mono}} \sim 3000$  corresponds to the total number of atoms in each cluster, which indicates a diameter of about 3~4 nm for each cluster if a spherical shape is assumed. If it is supposed that the specimen subjected to low temperature annealing in the saturated state consists of the as-quenched matrix with resistivity  $\rho_{AQ}$ , plus small clusters with resistivity  $\rho_{SC}$ , the total resistivity  $\rho_{sat}$  can be expressed by the mean approximation as

$$\frac{\rho_{sat}}{\rho_{AQ}} = (1 - V_{SC}) + \frac{\rho_{SC}}{\rho_{AQ}} V_{SC} \quad (3-3)$$

where  $V_{SC}$  is the volume fraction of the small clusters and

$$\frac{\rho_{sat}}{\rho_{AQ}} = \delta + 1 \quad (3-4)$$

where  $\delta$  is the fractional increase of resistivity in eq. (3-1). Theoretical calculation has suggested that the residual resistivity of a Ni-Cr alloy changes by  $\sim 2 \times 10^{-7}$   $\Omega\text{m}$  by preferential formation of a Cr-Ni pair from the random state [77]. If the same resistivity change is assumed for the present Cr-Co-Ni alloy, and a value of  $\rho_{AQ} = 1.02 \times 10^{-6}$   $\Omega\text{m}$

[78] is used,  $\frac{\rho_{SC}}{\rho_{AQ}}$  is calculated to be 1.22. This leads to the relationship  $V_{SC} = \frac{\delta}{0.22}$  from

which the volume fraction of small clusters is calculated to be  $V_{SC} = 0.21$  at  $\delta = 0.047$  (i.e., at 673 K, where the saturation resistivity is the highest in the present study).

Similarly, the volume fraction of small clusters is calculated to be  $V_{SC} = 0.18$  at  $\delta = 0.039$  (773 K) and  $V_{SC} = 0.12$  at  $\delta = 0.027$  (873 K).

The above analyses, though crude, helps us visualize the atomic structures in the SRO states of the equiatomic Cr-Co-Ni MEA as follows. First, although the SRO state is defined by an SRO parameter like Warren-Cowley, the atomic arrangement is not uniform everywhere, i.e., the same degree of SRO is not present throughout the specimen. Rather, the specimen contains some clusters with higher degree of SRO of the  $(\text{Ni,Co})_3\text{Cr}$ -type surrounded by a matrix with lower degree of SRO. Second, the size of these clusters is about 3~4 nm in diameter and their volume fraction is at most only 20%. Third, the boundary between the two different regions (that is, between the clusters and matrix) may be diffuse and not discrete, although further study is needed to clarify this. Finally, the small size of clusters with higher degree of SRO may indicate that these clusters do not grow much in size during isothermal annealing but rather increase in density until the saturation value is reached at the various annealing temperatures.

### **3.4.3 Changes in mechanical properties with SRO**

In contrast to an earlier report [43] of a remarkable 25% increase in yield strength associated with SRO in polycrystalline, equiatomic Cr-Co-Ni after annealing at 1273 K followed by furnace cooling, here it is found essentially no change in the CRSS of single crystals of the equiatomic Cr-Co-Ni subjected to different heat treatments, as well as only a 2% increase in electrical resistivity after furnace cooling (at a rate of 100 K per hour) from 1273 K. A possible reason for this discrepancy may be that Zhang et al. [43] tested large-grained polycrystals (grain sizes of 800  $\mu\text{m}$  and 1000  $\mu\text{m}$  in the water-quenched and aged specimens, respectively). Their relatively small tensile specimens had a thickness of

800  $\mu\text{m}$ , which means that they contained only one grain through the thickness. Unless, by coincidence, the differently heat treated specimens had exactly the same orientation of the through-thickness grains, it is entirely possible that part or all of their yield strength increase (25%) was due to differences in grain orientations. Here, by contrast, the tensile specimens were all oriented for single slip along the  $[\bar{1}23]$  loading axis, which allows us to more precisely determine the effect of SRO on CRSS without any confounding effects of different orientations in different gage sections. Inoue et al. [48] reported no measurable change in the yield strength of polycrystalline, equiatomic Cr-Co-Ni after annealing at 973 K for 384 hours followed by water quenching. The latter results are understandable based on Fig. 3.1(a) because the annealing temperature (973 K) they employed is too high to form significant SRO as the increment in electrical resistivity is small (0.5%).

The electrical resistivity measurements in the present study show that SRO in the equiatomic Cr-Co-Ni MEA occurs in the temperature range of 673-873 K with the saturation value of electrical resistivity being higher at lower temperatures (the increment is 2.7% at 873 K and 4.8% at 673 K, see Fig. 3.1(a)). In spite of changes in electrical resistivity upon annealing in this range, no significant change in the plastic deformation behavior is found for single crystals of the equiatomic Cr-Co-Ni MEA. In the equiatomic Cr-Co-Ni MEA, neither yield strength nor yield drop correlate with the degree of SRO as in Cu-Au [18,20] and Ag-Au [33] polycrystals. This is also the case for the strain localization behavior, dislocation structure and variations in dislocation dissociation width, none of which are significantly affected by the formation of SRO in the equiatomic Cr-Co-Ni MEA. This may mean that even when a finite value of Warren-Cowley

parameter ( $\alpha_{Cr-Co}=0.217$  at the maximum) is obtained, changes in atomic arrangement before and after the formation of SRO are not significant enough in the ternary system to significantly affect the dislocation behavior, as discussed in section 3.4.2.

Most theories that have been proposed to account for the strengthening (but not softening) due to SRO assume, a priori, a uniform atomic arrangement when there is a finite degree of SRO (as expressed by the Warren-Cowley parameter,  $\alpha$ ). When SRO domains are present, an extra external stress will be required for dislocation glide because energetically favored bonds need to be sheared and unfavored ones formed, the extent of which depends on the  $\gamma_{db}$  (in the form of  $\tau=\gamma_{db}/b$ ), as described below [30,31].

$$\gamma_{db} = \frac{2\Delta E}{a^2 \sqrt{3}/4} = \frac{8}{\sqrt{3}} \frac{c_A c_B \alpha}{a^2} kT \ln\left[1 + \frac{\alpha}{c_A c_B (1-\alpha)^2}\right] \quad (3-5)$$

with

$$\Delta E = 2c_A c_B \alpha_{A,B} v^{A,B} \quad (3-6)$$

where  $a$  is the lattice constant,  $c_A$  and  $c_B$  are the atomic fractions of A and B elements,  $\alpha_{A,B}$  is the Warren-Cowley SRO parameter,  $v^{A,B}$  is the energy required to rearrange the lattice to form two A-B bonds from one A-A and one B-B bond estimated by the relation,

$$\frac{\alpha}{(1-\alpha)^2} = c_A c_B \left(\exp \frac{2v^{A,B}}{kT} - 1\right) \quad (3-7)$$

where  $k$  is the Boltzmann constant,  $T$  is the annealing temperature. The stress increment due to the SRO domain hardening is calculated in Fig. 3.9(a) as a function of  $\alpha_{Cr-Co}$  in the range of 0~0.26 with the use of eq. (5). This range of  $\alpha_{Cr-Co}$  was chosen to be consistent with the maximum value calculated previously (0.217 at 700 K [75], 0.16 at 800K and 0.25 at 500 K [11,13]). The shear stress increment due to SRO domain

hardening increases with the increase in  $\alpha_{Cr-Co}$ , amounting to 139 MPa at  $\alpha_{Cr-Co}=0.217$ . The stress increment is basically calculated at 0 K but it may not depend strongly on temperature as the temperature dependence of anti-phase boundary (APB) in many intermetallic compounds of the L1<sub>2</sub>-type is known to be small [79,80].

The above theoretical treatment neglects the fact that SRO will also alter the atomic arrangement which will in turn also cause changes in the lattice distortion. Recently, Antillon et al. [67] proposed for the first time that the strength of solid-solution alloys with a finite degree of SRO consists of two terms: (1) an SRO domain-hardening term as described in eq. (5), and (2) a size-misfit term that is generally used to describe the solid-solution strength. They further proposed that, while SRO domain hardening increases with SRO, the size-misfit term decreases. Antillon et al. [67] used the formula proposed by Varvenne et al. [81] to calculate the size-misfit term. Alternatively, the mean-square atomic displacement (MSAD), which is a measure of the displacement of the constituent atoms from the regular lattice positions, can be used as a scaling factor for the CRSS at 0 K in FCC solid solutions [6,9]. The linear relation  $\sigma_Y(0\text{ K})/\mu = 0.2973(\text{MSAD}^{1/2})/b$  is obtained for polycrystals of equiatomic quinary, quaternary and ternary alloys, when the yield stress at 0 K ( $\sigma_Y(0\text{ K})$ ) and  $\text{MSAD}^{1/2}$  are normalized respectively to  $\mu$  (shear modulus) and  $b$  (Burgers vector) [6]. To estimate the magnitude of the increase (or decrease) in CRSS (i.e., the size-misfit term) due to SRO, the variation of MSAD with the degree of SRO was calculated by utilizing special quasirandom structure (SQS) as Kostiuchenko et al. [82] did. As seen in Fig. 3.9(b), MSAD decreases with increasing  $\alpha_{Cr-Co}$  (i.e., the development of SRO). At  $\alpha_{Cr-Co} = 0.217$  (the previously calculated saturation value at 700 K [75]), the decrease in  $\text{MSAD}^{1/2}$  is 1.39 pm, which corresponds

to a decrease in  $\sigma_Y(0\text{ K})$  of 112.41 MPa. This value is converted into the CRSS at 0 K by dividing by the Taylor factor (3.06). The CRSS for solid-solution alloys is known to vary with temperature as follows.

$$\tau(T) = \tau_{ath} + \tau_{th}(0) \left[ 1 - \left( \frac{T}{T_{ath}} \right)^{1/q} \right]^{1/p} \quad (3-8)$$

where  $\tau_{ath}$  is the athermal stress component,  $\tau_{th}(0)$  is the thermal stress component at 0 K,  $T_{ath}$  is the athermal temperature,  $p$  and  $q$  are fitting parameters depending on the

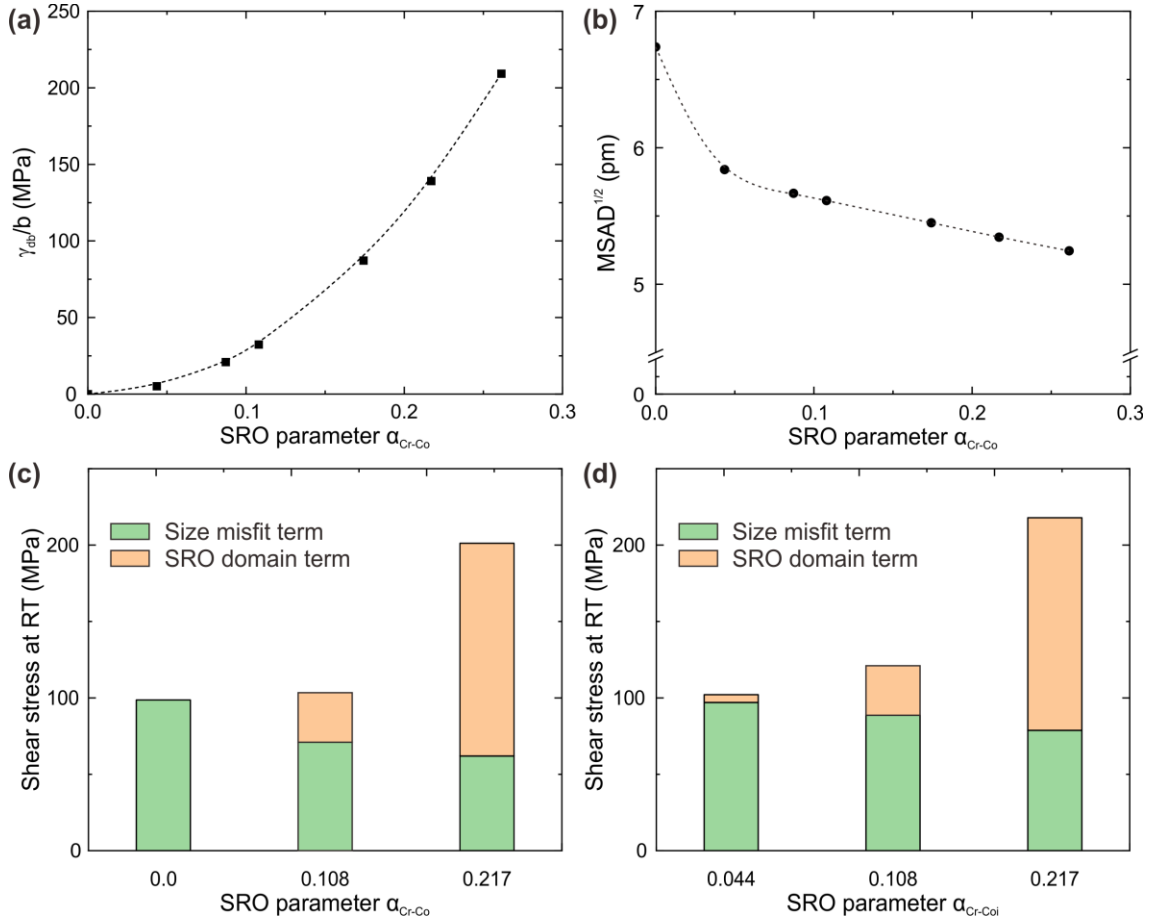


**Fig. 3.9** (a) Shear stress increment due to the SRO domain hardening and (b) variation of MSAD calculated as a function of SRO parameter. Contributions from the SRO domain hardening term and size misfit (MSAD) term on the development of SRO calculated with the two different initial state of SRO ( $\alpha_{Cr-Co}$ ; (c) 0 and (d) 0.044) after quenching from 1473 K.

obstacle type. The  $1/p$  and  $1/q$  values were determined to be 2.38 and 0.9 for the equiatomic Cr-Co-Ni polycrystals [6]. The CRSS at room temperature can be calculated with the use of eq. (3-8), assuming none of the fitting parameters in eq. (3-8) change with the degree of SRO. This is consistent with the present observation that the CRSS at room temperature and 77 K are identical for different specimens with different degrees of SRO (one annealed at 1473 K and another subsequently annealed at 773K for 168 hours) (Fig. 3.4(a)). Then, the CRSS at room temperature can be calculated as a function of the degree of SRO ( $\alpha_{Cr-Co}$ ) as the sum of the SRO domain-hardening term described in eq. (3-5) and the size-misfit term described with the MSAD values. The CRSS at room temperature was calculated as a function of  $\alpha_{Cr-Co}$  (0.108 and 0.217) for the two different initial states of SRO after quenching from 1473 K ( $\alpha_{Cr-Co} = 0$  and 0.044, Figs. 3.9(c) and (d) respectively). A finite value of  $\alpha_{Cr-Co}=0.044$  is taken arbitrarily as the initial SRO state assuming that some degree of SRO is present even after water-quenching as a result of the very high kinetics of the SRO formation. Regardless of the initial state of SRO after quenching from 1473 K, the SRO domain-hardening term increases significantly and the size-misfit term decreases with the development of SRO (i.e., with the increase in  $\alpha_{Cr-Co}$ ). As the SRO domain-hardening dominates, the CRSS at room temperature increases significantly with the increase in  $\alpha_{Cr-Co}$ , amounting to more than 100 MPa at  $\alpha_{Cr-Co} = 0.217$  (the previously mentioned saturation value at 700 K [75]). This is far larger than what is experimentally observed for specimens annealed at 673 K for 504 hours, in which no significant change in CRSS is observed at the saturation value of SRO and requires further discussion.

However, before addressing the unrealistically high domain-hardening term, it is important to note that the concept that strength depends on a SRO domain-hardening term and a size-misfit term allows us to understand how strength can decrease (and not merely increase) due to the size-misfit term. Consistent with this, Büttner and Nembach [18] observed that the yield strength of Cu-Au polycrystals reached a minimum when the degree of SRO reached a maximum. In this study, it can be seen that the CRSS decreases slightly with the development of SRO (i.e., with the decrease in annealing temperature) in Fig. 3.4(a), although the decrease is small and comparable to the experimental scatter. Next it is discussed why the calculated contribution of the SRO domain-hardening term is unrealistically large.

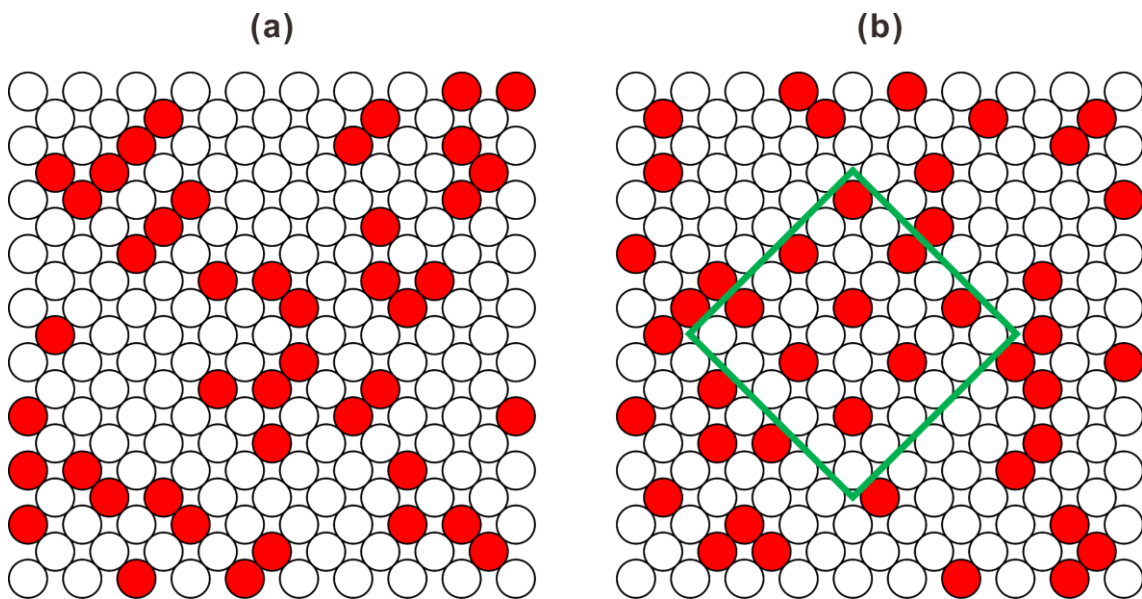


**Fig. 3.10** (a) Statistical SRO throughout the specimen. (b) Heterogeneous SRO occurs in domains [83].

It is believed that it results from the assumption that a uniform atomic arrangement with a finite degree of SRO is formed throughout specimen, as shown in Fig. 3.10 (a). In real crystals with a finite value of SRO parameter, the atomic arrangement may be quite different, as discussed in the previous section. It is postulated that, in the equiatomic Cr-

Co-Ni MEA, SRO occurs by forming some (at most 20% by volume) isolated nm-sized domains with a higher order of SRO in a matrix that has a much lower degree of SRO, as shown in Fig. 3.10 (b). In such a case, the contribution of the SRO domain-hardening term will be decreased significantly. Note that this is also the case for the contribution of the size-misfit term, as MSAD is calculated on the same assumption of a uniform atomic arrangement with a finite degree of SRO throughout the specimen. If a realistic atomic arrangement is taken into account, the decrease in MSAD will be reduced significantly resulting in a corresponding reduction in the decrease of CRSS due to this term. As a result, the change in the strength of solid-solutions upon the formation of SRO will be much reduced when compared to what is expected from theoretical calculations that assume a uniform atomic arrangement with a finite degree of SRO.

### **3.5 Conclusions**

The evolution of SRO in the equiatomic Cr-Co-Ni MEA was investigated by monitoring changes in electrical resistivity and compared it to changes in x-ray and electron diffraction signals. Also investigated are the effects of SRO on the mechanical properties of single crystals of the equiatomic Cr-Co-Ni MEA in tension and in compression at room temperature and liquid nitrogen temperature. Based on the results obtained, the following conclusions can be drawn.

(1) The development of SRO in the Cr-Co-Ni MEA cannot be monitored by simple x-ray and electron diffraction experiments because of the very small difference in atomic scattering factors of the constituent elements. But it can be easily monitored by electrical resistivity measurements.

(2) The electrical resistivity increases gradually and reaches a saturation value during isothermal annealing at a temperature in the range of 673-973 K. While the time required for saturation is shorter at higher temperatures, the saturation value is higher at lower temperatures. This indicates that the degree of SRO is higher at lower temperatures but the kinetics of short-range ordering are slower at lower temperatures.

(3) In spite of changes in electrical resistivity (and the implied changes in degree of SRO) upon annealing at temperatures in the range of 673-973 K, no significant change in the plastic deformation behavior is found at room temperature and at 77 K for single crystals of the equiatomic Cr-Co-Ni MEA. The yield stress as well as the slip localization behavior does not change much as a result of SRO, and the magnitude of yield drop does not correlate with the degree of SRO. The tensile stress-strain curve does not change much with SRO up to high strain levels, giving rise to identical shear stress for the onset of deformation twinning at room temperature in specimens with high and low degrees of SRO. The dislocation structure, variations in dislocation dissociation width and stacking fault energy are also all essentially unchanged.

## Supplementary figures

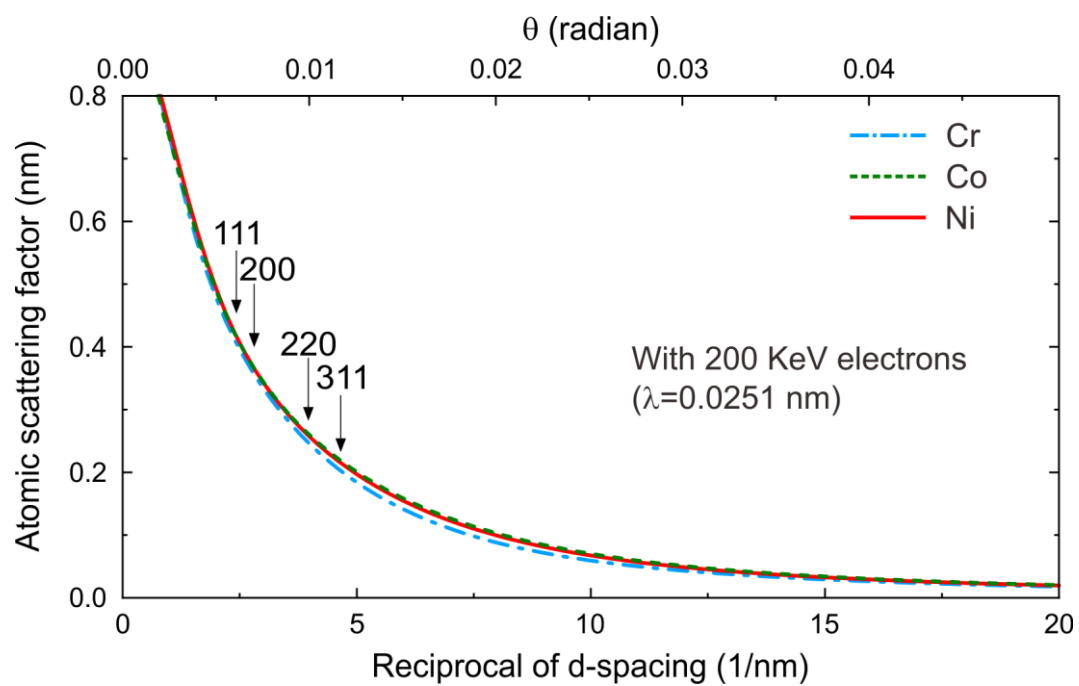


**Fig. S3.1** Atomic scattering factor for Cr, Co and Ni plotted as a function of scattering angle. The scattering angles corresponding to 111, 200, 220, 311 reflections are indicated.

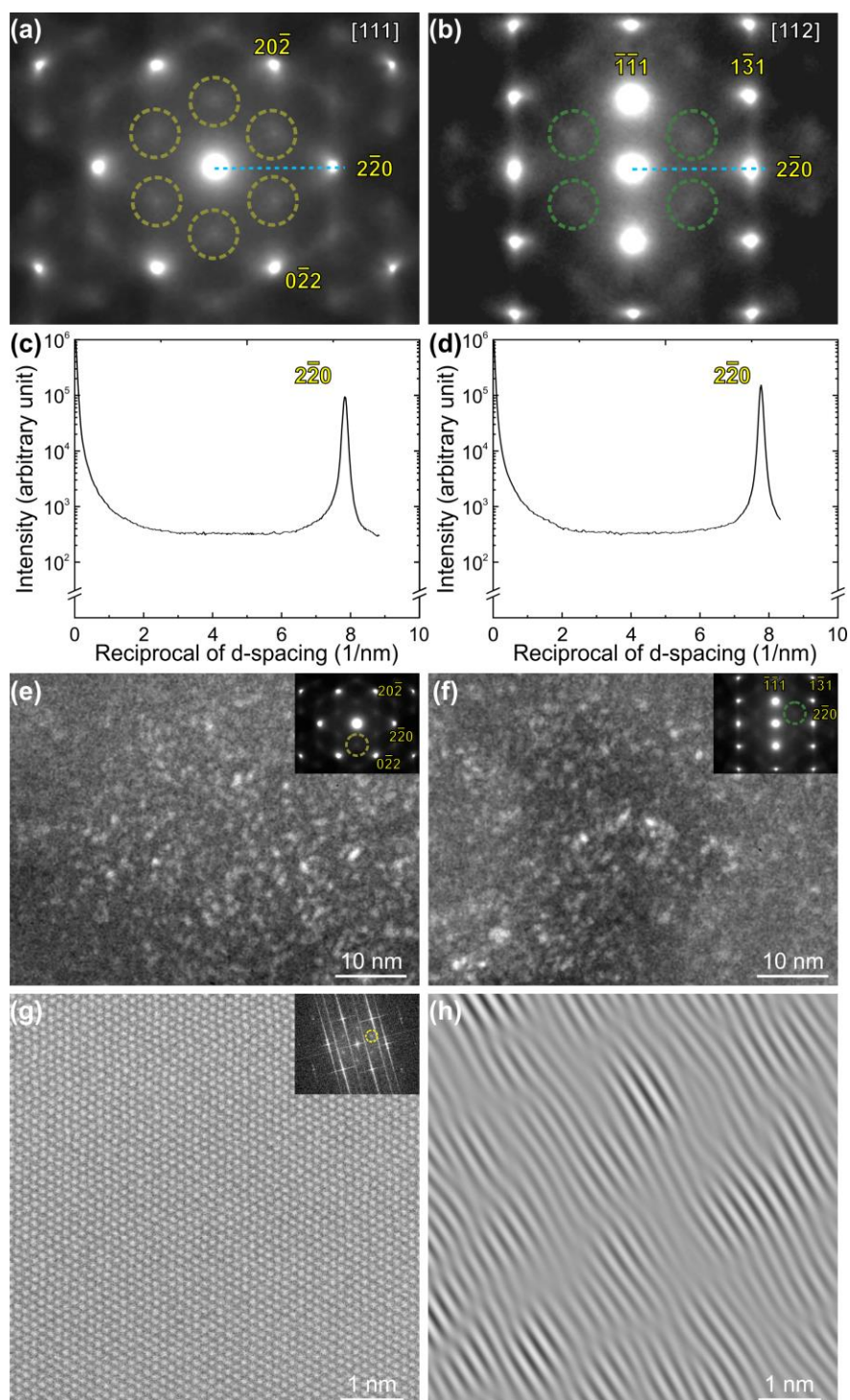


**Fig. S3.2** SAED patterns with the (a) [111] and (b) [112] incidences taken from Cu. Intensity profile along a line between the transmitted beam and  $2\bar{2}0$  reflection in SAED patterns with (c) [111] and (d) [112] incidences. Dark-field images formed by setting an objective aperture at a position of (e)  $1/3\{422\}$  and (f)  $1/2\{113\}$  (as shown in the inset SAED patterns). (g) Atomic-resolution HAADF-STEM image taken along [111] with FFT diagram (inset). (h) Inverse FFT image formed with the diffuse intensities at  $1/3\{422\}$  position in the FFT diagram.

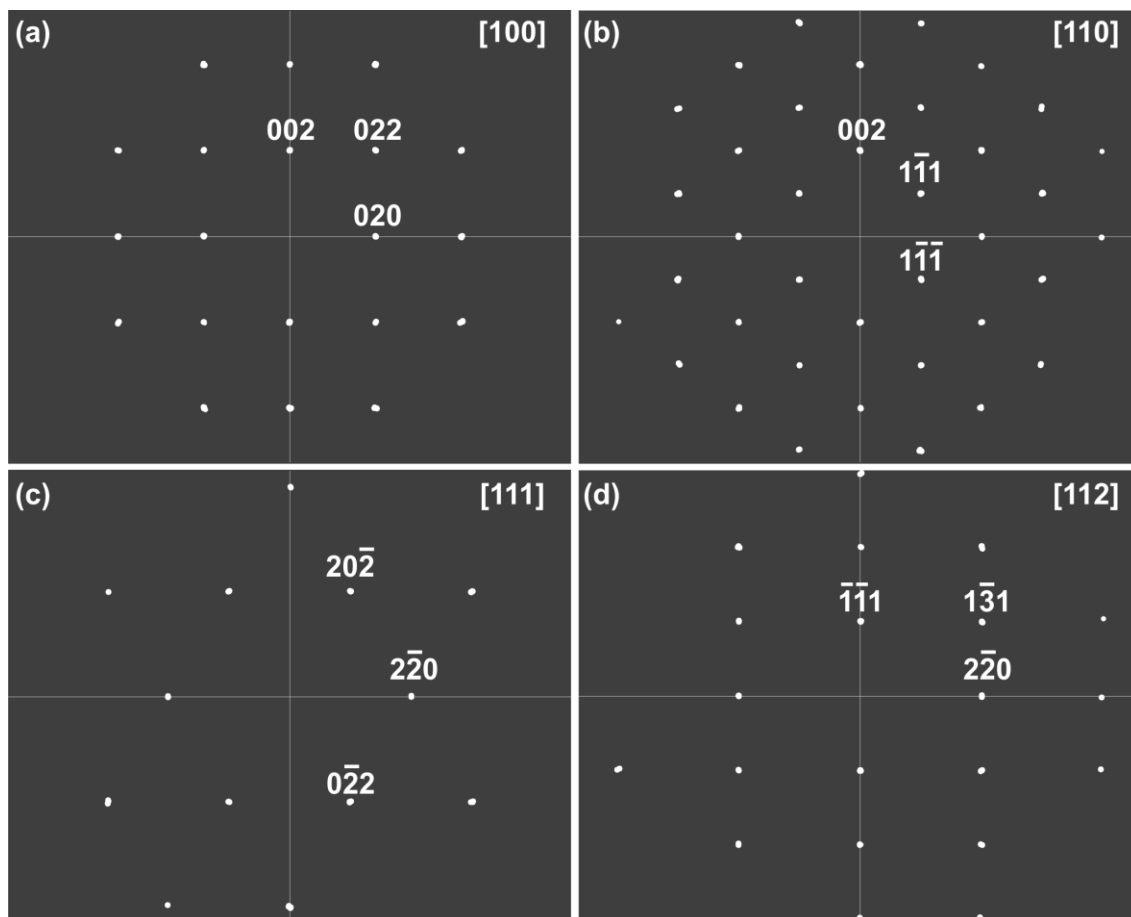


**Fig. S3.3** Synchrotron x-ray diffraction patterns taken along (a)  $[100]$ , (b)  $[110]$ , (c)  $[111]$  and (d)  $[112]$  directions from a single crystal subsequently annealed at 773 K for 168 hours after water-quenching from 1473 K.

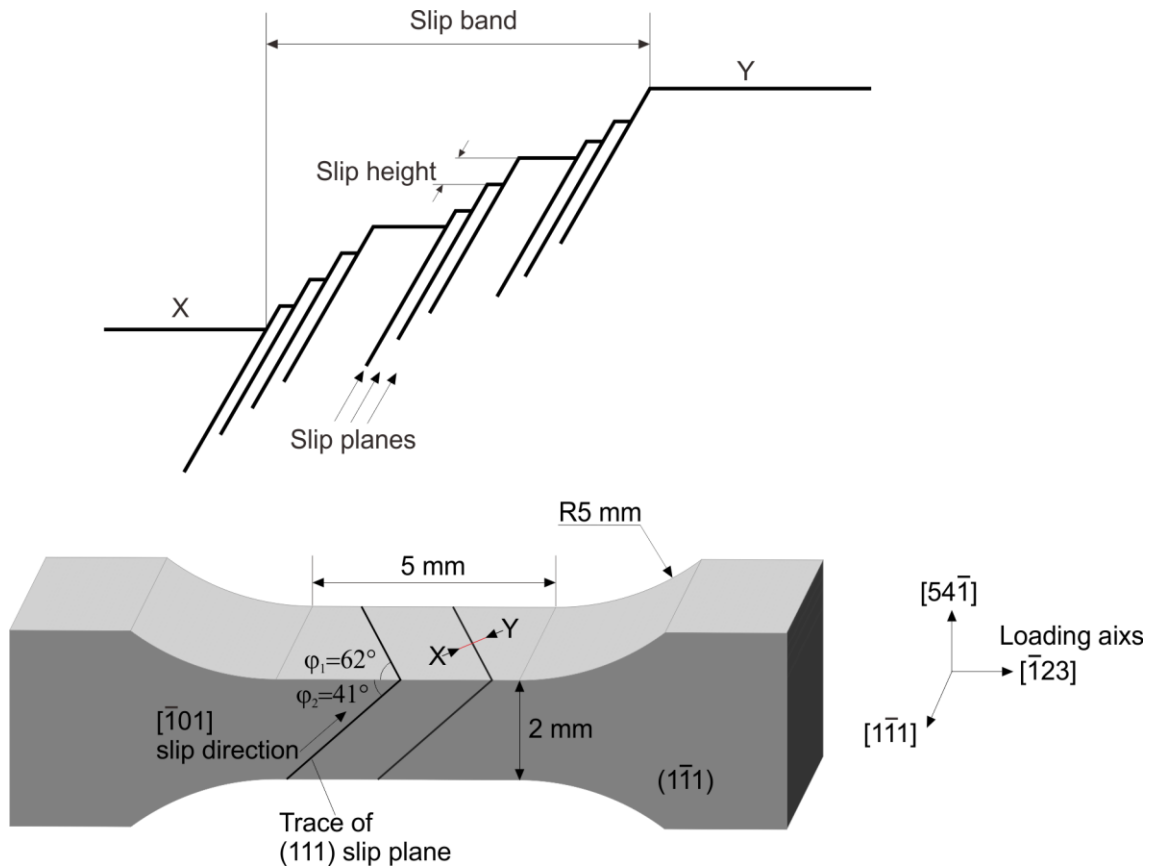


**Fig. S3.4** Specimen geometry for optical and atomic force microscopy observations of slip lines formed on the  $(54\bar{1})$  surface of  $[\bar{1}23]$ -oriented single crystals of the equiatomic Cr-Co-Ni MEA.

## Reference

- [1] D.B. Miracle, O.N. Senkov, A critical review of high entropy alloys and related concepts, *Acta Mater.* 122 (2017) 448–511. <https://doi.org/10.1016/j.actamat.2016.08.081>.
- [2] E.P. George, D. Raabe, R.O. Ritchie, High-entropy alloys, *Nat. Rev. Mater.* 4 (2019) 515–534. <https://doi.org/10.1038/s41578-019-0121-4>.
- [3] Z. Li, S. Zhao, R.O. Ritchie, M.A. Meyers, Mechanical properties of high-entropy alloys with emphasis on face-centered cubic alloys, *Prog. Mater. Sci.* 102 (2019) 296–345. <https://doi.org/10.1016/j.pmatsci.2018.12.003>.
- [4] E. Ma, Unusual dislocation behavior in high-entropy alloys, *Scr. Mater.* 181 (2020) 127–133. <https://doi.org/10.1016/j.scriptamat.2020.02.021>.
- [5] E.P. George, W.A. Curtin, C.C. Tasan, High entropy alloys: A focused review of mechanical properties and deformation mechanisms, *Acta Mater.* 188 (2020) 435–474. <https://doi.org/https://doi.org/10.1016/j.actamat.2019.12.015>.
- [6] H. Inui, K. Kishida, L. Li, A.M. Manzoni, S. Haas, U. Glatzel, Uniaxial mechanical properties of face-centered cubic single- and multiphase high-entropy alloys, *MRS Bull.* 47 (2022) 168-185. <https://doi.org/10.1557/S43577-022-00280-Y>.

- [7] H. Inui, K. Kishida, Z.H. Chen, Recent Progress in Our Understanding of Phase Stability, Atomic Structures and Mechanical and Functional Properties of High-Entropy Alloys, *Mater. Trans.* 63 (2022) 394-401. <https://doi.org/https://doi.org/10.2320/matertrans.MT-M2021234>.
- [8] W.A. Curtin, S.I. Rao, C. Woodward, Progress and challenges in the theory and modeling of complex concentrated alloys, *MRS Bull.* 47 (2022) 151–157. <https://doi.org/10.1557/s43577-022-00306-5>.
- [9] N.L. Okamoto, K. Yuge, K. Tanaka, H. Inui, E.P. George, Atomic displacement in the CrMnFeCoNi high-entropy alloy-A scaling factor to predict solid solution strengthening, *AIP Adv.* 6 (2016) 125008. <https://doi.org/10.1063/1.4971371>.
- [10] Y.Y. Zhao, Z.F. Lei, Z.P. Lu, J.C. Huang, T.G. Nieh, A simplified model connecting lattice distortion with friction stress of Nb-based equiatomic high-entropy alloys, *Mater. Res. Lett.* 7 (2019) 340–346. <https://doi.org/10.1080/21663831.2019.1610105>.
- [11] A. Tamm, A. Aabloo, M. Klintonberg, M. Stocks, A. Caro, Atomic-scale properties of Ni-based FCC ternary, and quaternary alloys, *Acta Mater.* 99 (2015) 307–312. <https://doi.org/10.1016/j.actamat.2015.08.015>.
- [12] Y. Rao, W.A. Curtin, Analytical models of short-range order in FCC and BCC alloys, *Acta Mater.* 226 (2022) 117621. <https://doi.org/10.1016/j.actamat.2022.117621>.
- [13] J. Ding, Q. Yu, M. Asta, R.O. Ritchie, Tunable stacking fault energies by tailoring local chemical order in CrCoNi medium-entropy alloys, *Proc. Natl. Acad. Sci. U. S. A.* 115 (2018) 8919–8924. <https://doi.org/10.1073/pnas.1808660115>.
- [14] Q.J. Li, H. Sheng, E. Ma, Strengthening in multi-principal element alloys with local-chemical-order roughened dislocation pathways, *Nat. Commun.* 10 (2019) 1–11. <https://doi.org/10.1038/s41467-019-11464-7>.
- [15] A.C. Damask, Some resistivity effects of short-range order in  $\alpha$  brass, *J. Appl. Phys.* 27 (1956) 610–616. <https://doi.org/10.1063/1.1722441>.
- [16] R.G. Davies, R.W. Cahn, Short range order in aluminium bronze, *Acta Metall.* 10 (1962) 170–171. [https://doi.org/10.1016/0001-6160\(62\)90062-7](https://doi.org/10.1016/0001-6160(62)90062-7).
- [17] R.O. Scattergood, M.B. Bever, The relation of short-range order to the deformation behaviour of copper-rich copper-aluminium alloys, *Philos. Mag.* 22 (1970) 501–514. <https://doi.org/10.1080/14786437008225840>.
- [18] N. Büttner, E. Nembach, On short-range order hardening in Cu-10 at.% Au, *Acta Metall.* 30 (1982) 83–86. [https://doi.org/10.1016/0001-6160\(82\)90047-5](https://doi.org/10.1016/0001-6160(82)90047-5).
- [19] W. Pfeiler, Investigation of short-range order by electrical resistivity measurement, *Acta Metall.* 36 (1988) 2417–2434. [https://doi.org/10.1016/0001-6160\(88\)90192-7](https://doi.org/10.1016/0001-6160(88)90192-7).
- [20] O. Kuhlmann, H. Rösner, E. Nembach, The effects of order on the critical resolved shear stress of Cu-10 at.% Au single crystals, *Acta Mater.* 45 (1997) 3319–3326. [https://doi.org/10.1016/S1359-6454\(97\)82885-6](https://doi.org/10.1016/S1359-6454(97)82885-6).
- [21] V.G. Gavriljuk, B.D. Shanina, H. Berns, On the correlation between electron structure and short range atomic order in iron-based alloys, *Acta Mater.* 48 (2000) 3879–3893. [https://doi.org/10.1016/S1359-6454\(00\)00192-0](https://doi.org/10.1016/S1359-6454(00)00192-0).
- [22] Y. Wang, D. Jiang, W. Yu, S. Huang, D. Wu, Y. Xu, X. Yang, Short-range ordering in a commercial Ni-Cr-Al-Fe precision resistance alloy, *Mater. Des.* 181 (2019) 1–9. <https://doi.org/10.1016/j.matdes.2019.107981>.
- [23] A. Marucco, B. Nath, Effects of ordering on the properties of Ni-Cr alloys, *J. Mater. Sci.* 23 (1988) 2107–2114.

- [24] A. Marucco, Atomic ordering and  $\alpha'$ -Cr phase precipitation in long-term aged Ni<sub>3</sub>Cr and Ni<sub>2</sub>Cr alloys, *J. Mater. Sci.* 30 (1995) 4188–4194.
- [25] A. Taylor, K.G. Hinton, A study of order disorder and precipitation phenomena in nickel chromium alloys, *J. Inst. Met.* 81 (1952) 169–180.
- [26] N.R. Dudova, R.O. Kaibyshev, V.A. Valitov, Short-range ordering and the abnormal mechanical properties of a Ni-20% Cr alloy, *Phys. Met. Metallogr.* 2009 1086. 108 (2009) 625–633. <https://doi.org/10.1134/S0031918X0912014X>.
- [27] W. Wagner, R. Poerschke, H. Wollenberger, Dependence of electrical resistivity on the degree of short range order in a nickel-copper alloy, *Philos. Mag. B.* 43 (1981) 345–355. <https://doi.org/10.1080/13642818108221904>.
- [28] P. Cenedese, F. Bley, S. Lefebvre, Diffuse scattering in disordered ternary alloys: neutron measurements of local order in a stainless steel Fe<sub>0.56</sub>Cr<sub>0.21</sub>Ni<sub>0.23</sub>, *Acta Crystallogr. Sect. A.* 40 (1984) 228–240. <https://doi.org/10.1107/S0108767384000489>.
- [29] A.Z. Menshikov, C. Dimitrov, A.E. Teplykh, Local atomic redistribution under irradiation in  $\gamma$ -NiFeCr alloys, *J. Phys. III.* 7 (1997) 1899–1908. <https://doi.org/10.1051/jp3:1997231>.
- [30] J.C. Fisher, On the strength of solid solution alloys, *Acta Metall.* 2 (1954) 9–10. [https://doi.org/10.1016/0001-6160\(54\)90087-5](https://doi.org/10.1016/0001-6160(54)90087-5).
- [31] P.A. Flinn, Solute hardening of close-packed solid solutions, *Acta Metall.* 6 (1958) 631–635. [https://doi.org/10.1016/0001-6160\(58\)90156-1](https://doi.org/10.1016/0001-6160(58)90156-1).
- [32] J.B. Cohen, M.E. Fine, Some aspects of short-range order, *J. Phys. Radium.* 23 (1962) 749–762. <https://doi.org/10.1051/jphysrad:019620023010074901i>.
- [33] J.J. Svitak, R.M. Asimow, Solid-solution strengthening in the Ag-Au system, *TRANS MET SOC AIME.* 245 (1969) 209–212.
- [34] S. Patu, R.J. Arsenault, Strengthening due to non-random solid solutions, *Mater. Sci. Eng. A.* 194 (1995) 121–128. [https://doi.org/10.1016/0921-5093\(94\)09674-0](https://doi.org/10.1016/0921-5093(94)09674-0).
- [35] F.X. Zhang, S. Zhao, K. Jin, H. Xue, G. Velisa, H. Bei, R. Huang, J.Y.P. Ko, D.C. Pagan, J.C. Neufeind, W.J. Weber, Y. Zhang, Local Structure and Short-Range Order in a NiCoCr Solid Solution Alloy, *Phys. Rev. Lett.* 118 (2017) 1–6. <https://doi.org/10.1103/PhysRevLett.118.205501>.
- [36] K. Yuge, S. Ohta, Microscopic geometry rules ordering tendency for multicomponent disordered alloys, *J. Phys. Soc. Japan.* 88 (2019) 1–6. <https://doi.org/10.7566/JPSJ.88.054803>.
- [37] L. Zhou, Q. Wang, J. Wang, X. Chen, P. Jiang, H. Zhou, F. Yuan, X. Wu, Z. Cheng, E. Ma, Atomic-scale evidence of chemical short-range order in CrCoNi medium-entropy alloy, *Acta Mater.* 224 (2022) 16–18. <https://doi.org/10.1016/j.actamat.2021.117490>.
- [38] H. Tanimoto, R. Hozumi, M. Kawamura, Electrical resistivity and short-range order in rapid-quenched CrMnFeCoNi high-entropy alloy, *J. Alloys Compd.* 896 (2022) 163059. <https://doi.org/10.1016/j.jallcom.2021.163059>.
- [39] X. Yang, Y. Xi, C. He, H. Chen, X. Zhang, S.T. Tu, Chemical short-range order strengthening mechanism in CoCrNi medium-entropy alloy under nanoindentation, *Scr. Mater.* 209 (2022) 114364. <https://doi.org/10.1016/j.scriptamat.2021.114364>.
- [40] B. Schönfeld, C.R. Sax, J. Zemp, M. Engelke, P. Boesecke, T. Kresse, T. Boll, T. Al-Kassab, O.E. Peil, A. V. Ruban, Local order in Cr-Fe-Co-Ni: Experiment and

- electronic structure calculations, *Phys. Rev. B.* 99 (2019). <https://doi.org/10.1103/PhysRevB.99.014206>.
- [41] F.H. Cao, Y.J. Wang, L.H. Dai, Novel atomic-scale mechanism of incipient plasticity in a chemically complex CrCoNi medium-entropy alloy associated with inhomogeneity in local chemical environment, *Acta Mater.* 194 (2020) 283–294. <https://doi.org/10.1016/j.actamat.2020.05.042>.
- [42] B. Yin, S. Yoshida, N. Tsuji, W.A. Curtin, Yield strength and misfit volumes of NiCoCr and implications for short-range-order, *Nat. Commun.* 11 (2020) 2507. <https://doi.org/10.1038/s41467-020-16083-1>.
- [43] R. Zhang, S. Zhao, J. Ding, Y. Chong, T. Jia, C. Ophus, M. Asta, R.O. Ritchie, A.M. Minor, Short-range order and its impact on the CrCoNi medium-entropy alloy, *Nature.* 581 (2020) 283–287. <https://doi.org/10.1038/s41586-020-2275-z>.
- [44] W.R. Jian, Z. Xie, S. Xu, Y. Su, X. Yao, I.J. Beyerlein, Effects of lattice distortion and chemical short-range order on the mechanisms of deformation in medium entropy alloy CoCrNi, *Acta Mater.* 199 (2020) 352–369. <https://doi.org/10.1016/j.actamat.2020.08.044>.
- [45] J.B. Seol, J.W. Bae, J.G. Kim, H. Sung, Z. Li, H.H. Lee, S.H. Shim, J.H. Jang, W.S. Ko, S.I. Hong, H.S. Kim, Short-range order strengthening in boron-doped high-entropy alloys for cryogenic applications, *Acta Mater.* 194 (2020) 366–377. <https://doi.org/10.1016/j.actamat.2020.04.052>.
- [46] D. Zhou, Z. Chen, K. Ehara, K. Nitsu, K. Tanaka, H. Inui, Effects of annealing on hardness, yield strength and dislocation structure in single crystals of the equiatomic Cr-Mn-Fe-Co-Ni high entropy alloy, *Scr. Mater.* 191 (2021) 173–178. <https://doi.org/10.1016/j.scriptamat.2020.09.039>.
- [47] N. Hanasaki, M. Oda, K. Niitsu, K. Ehara, H. Murakawa, H. Sakai, H. Nitani, H. Abe, H. Sagayama, H. Uetsuka, T. Karube, H. Inui, Element dependence of local disorder in medium-entropy alloy CrCoNi, *AIP Adv.* 11 (2021) 125216. <https://doi.org/10.1063/5.0072766>.
- [48] K. Inoue, S. Yoshida, N. Tsuji, Direct observation of local chemical ordering in a few nanometer range in CoCrNi medium-entropy alloy by atom probe tomography and its impact on mechanical properties, *Phys. Rev. Mater.* 5 (2021) 1–7. <https://doi.org/10.1103/PhysRevMaterials.5.085007>.
- [49] A.M. Rana, A.F. Khan, A. Abbas, M.I. Ansari, Electrical resistivity behavior in Ni-25 at.% Cr alloy, *Mater. Chem. Phys.* 80 (2003) 228–231. [https://doi.org/10.1016/S0254-0584\(02\)00468-6](https://doi.org/10.1016/S0254-0584(02)00468-6).
- [50] A.Y. Volkov, A.E. Kostina, E.G. Volkova, O.S. Novikova, B.D. Antonov, Microstructure and Physicomechanical Properties of a Cu-8 at % Pd Alloy, *Phys. Met. Metallogr.* 118 (2017) 1236–1246. <https://doi.org/10.1134/S0031918X1712016X>.
- [51] M. Vaidya, S. Trubel, B.S. Murty, G. Wilde, S. V. Divinski, Ni tracer diffusion in CoCrFeNi and CoCrFeMnNi high entropy alloys, *J. Alloys Compd.* 688 (2016) 994–1001. <https://doi.org/10.1016/j.jallcom.2016.07.239>.
- [52] M. Vaidya, K.G. Pradeep, B.S. Murty, G. Wilde, S. V. Divinski, Bulk tracer diffusion in CoCrFeNi and CoCrFeMnNi high entropy alloys, *Acta Mater.* 146 (2018) 211–224. <https://doi.org/10.1016/j.actamat.2017.12.052>.
- [53] D. Gaertner, J. Kottke, Y. Chumlyakov, F. Hergemöller, G. Wilde, S. V. Divinski, Tracer diffusion in single crystalline CoCrFeNi and CoCrFeMnNi high-entropy

- alloys: Kinetic hints towards a low-temperature phase instability of the solid-solution?, *Scr. Mater.* 187 (2020) 57–62. <https://doi.org/10.1016/j.scriptamat.2020.05.060>.
- [54] C. Niu, A.J. Zaddach, A.A. Oni, X. Sang, J.W. Hurt, J.M. Lebeau, C.C. Koch, D.L. Irving, Spin-driven ordering of Cr in the equiatomic high entropy alloy NiFeCrCo, *Appl. Phys. Lett.* 106 (2015). <https://doi.org/10.1063/1.4918996>.
- [55] T. Fukushima, H. Katayama-Yoshida, K. Sato, M. Ogura, R. Zeller, P.H. Dederichs, Local energies and energy fluctuations - Applied to the high entropy alloy CrFeCoNi, *J. Phys. Soc. Japan.* 86 (2017) 1–7. <https://doi.org/10.7566/JPSJ.86.114704>.
- [56] Y.S. Kim, W.Y. Maeng, S.S. Kim, Effect of short-range ordering on stress corrosion cracking susceptibility of Alloy 600 studied by electron and neutron diffraction, *Acta Mater.* 83 (2015) 507–515. <https://doi.org/10.1016/j.actamat.2014.10.009>.
- [57] X. Chen, Q. Wang, Z. Cheng, M. Zhu, H. Zhou, P. Jiang, L. Zhou, Q. Xue, F. Yuan, J. Zhu, X. Wu, E. Ma, Direct observation of chemical short-range order in a medium-entropy alloy, *Nature.* 592 (2021) 712–716. <https://doi.org/10.1038/s41586-021-03428-z>.
- [58] J. Wang, P. Jiang, F. Yuan, X. Wu, Chemical medium-range order in a medium-entropy alloy, *Nat. Commun.* 13 (2022) 1–6. <https://doi.org/10.1038/s41467-022-28687-w>.
- [59] D.W. Pashley, M.J. Stowell, Electron microscopy and diffraction of twinned structures in evaporated films of gold, *Philos. Mag.* 8 (1963) 1605–1632. <https://doi.org/10.1080/14786436308207327>.
- [60] D. Cherns, Direct resolution of surface atomic steps by transmission electron microscopy, *Philos. Mag.* 30 (1974) 549–556. <https://doi.org/10.1080/14786439808206580>.
- [61] D. Cherns, The surface structure of (111) gold films sputtered in the high voltage electron microscope a theoretical model, *Philos. Mag.* 36 (1977) 1429–1444. <https://doi.org/10.1080/14786437708238526>.
- [62] J.C. Heyraud, J.J. Métois, Anomalous 1/3 422 diffraction spots from {111} flat gold crystallites: (111) surface reconstruction and moiré fringes between the surface and the bulk, *Surf. Sci.* 100 (1980) 519–528. [https://doi.org/10.1016/0039-6028\(80\)90419-7](https://doi.org/10.1016/0039-6028(80)90419-7).
- [63] J. Reyes-Gasga, A. Gómez-Rodríguez, X. Gao, M. José-Yacamán, On the interpretation of the forbidden spots observed in the electron diffraction patterns of flat Au triangular nanoparticles, *Ultramicroscopy.* 108 (2008) 929–936. <https://doi.org/10.1016/j.ultramic.2008.03.005>.
- [64] C. Miller, R. Field, M. Kaufman, The Presence of Higher-Order Laue Zone Intensities and the Relrod Effect in Cubic Metals in the Transmission Electron Microscope, *Microsc. Microanal.* 21 (2015) 1665–1666. <https://doi.org/10.1017/s1431927615009101>.
- [65] C. Fernando-Marquez, G. Mondragón-Galicia, L. Bazán-Díaz, J. Reyes-Gasga, Particle size and convergent electron diffraction patterns of triangular prismatic gold nanoparticles, *Rev. Mex. Física.* 67 (2021) 1–8. <https://doi.org/10.31349/revmexfis.67.041005>.
- [66] L. Li, Z. Chen, S. Kuroiwa, M. Ito, K. Kishida, H. Inui, E.P. George, Tensile and compressive plastic deformation behavior of medium-entropy Cr-Co-Ni single

- crystals from cryogenic to elevated temperatures, *Int. J. Plast.* 148 (2022) 103144. <https://doi.org/10.1016/J.IJPLAS.2021.103144>.
- [67] E. Antillon, C. Woodward, S.I. Rao, B. Akdim, T.A. Parthasarathy, Chemical short range order strengthening in a model FCC high entropy alloy, *Acta Mater.* 190 (2020) 29–42. <https://doi.org/10.1016/j.actamat.2020.02.041>.
- [68] W.M. Stobbs, C.H. Sworn, The weak beam technique as applied to the determination of the stacking-fault energy of copper, *Philos. Mag.* 24 (1971) 1365–1381. <https://doi.org/10.1080/14786437108217418>.
- [69] D.J.H. Cockayne, M.L. Jenkins, I.L.F. Ray, The measurement of stacking-fault energies of pure face-centred cubic metals, *Philos. Mag.* 24 (1971) 1383–1392. <https://doi.org/10.1080/14786437108217419>.
- [70] N.L. Okamoto, S. Fujimoto, Y. Kambara, M. Kawamura, Z.M.T. Chen, H. Matsunoshita, K. Tanaka, H. Inui, E.P. George, Size effect, critical resolved shear stress, stacking fault energy, and solid solution strengthening in the CrMnFeCoNi high-entropy alloy, *Sci. Rep.* 6 (2016) 35863.
- [71] M. Kawamura, M. Asakura, N.L. Okamoto, K. Kishida, H. Inui, E.P. George, Plastic deformation of single crystals of the equiatomic Cr–Mn–Fe–Co–Ni high-entropy alloy in tension and compression from 10 K to 1273 K, *Acta Mater.* 203 (2021) 116454. <https://doi.org/10.1016/j.actamat.2020.10.073>.
- [72] H. Thomas, Über Widerstandslegierungen, *Zeitschrift Für Phys.* 129 (1951) 219–232. <https://doi.org/10.1007/BF01333398>.
- [73] H. Neuhäuser, Slip-line formation and collective dislocation motion, in: F.R.N. Nabarro (Ed.), *Dislocations Solids Vol. 6*, North-Holland, 1983: pp. 319–440.
- [74] J. Plessing, C. Achmus, H. Neuhäuser, B. Schönfeld, G. Kostorz, Short-range order and the mode of slip in concentrated Cu-based alloys, *Zeitschrift Fuer Met. Res. Adv. Tech.* 88 (1997) 630–635.
- [75] J.P. Du, P. Yu, S. Shinzato, F. Meng, Y. Sato, Y. G. Li, Y. W. Fan and S. Ogata. “Chemical domain structure and its formation kinetics in CrCoNi medium-entropy alloy”, submitted.
- [76] D.M.C. Nicholson, R.H. Brown, Electrical resistivity of Ni<sub>0.8</sub>Mo<sub>0.2</sub>: Explanation of anomalous behavior in short-range ordered alloys, *Phys. Rev. Lett.* 70 (1993) 3311–3314. <https://doi.org/10.1103/PhysRevLett.70.3311>.
- [77] S. Lowitzer, D. Ködderitzsch, H. Ebert, P.R. Tulip, A. Marmodoro, J.B. Staunton, An ab initio investigation of how residual resistivity can decrease when an alloy is deformed, *Epl.* 92 (2010). <https://doi.org/10.1209/0295-5075/92/37009>.
- [78] K. Jin, B.C. Sales, G.M. Stocks, G.D. Samolyuk, M. Daene, W.J. Weber, Y. Zhang, H. Bei, Tailoring the physical properties of Ni-based single-phase equiatomic alloys by modifying the chemical complexity, *Sci. Rep.* 6 (2016) 1–10. <https://doi.org/10.1038/srep20159>.
- [79] A. Korner, G. Schoeck, The temperature dependence of the antiphase boundary energy in Ni<sub>3</sub>Fe I. The equilibrium value, *Philos. Mag. A Phys. Condens. Matter, Struct. Defects Mech. Prop.* 61 (1990) 909–915. <https://doi.org/10.1080/01418619008234950>.
- [80] T. Kruml, B. Viguier, J. Bonneville, J.L. Martin, Temperature dependence of dislocation microstructure in Ni<sub>3</sub>(Al,Hf), *Mater. Sci. Eng. A.* 234–236 (1997) 755–757. [https://doi.org/10.1016/s0921-5093\(97\)00391-2](https://doi.org/10.1016/s0921-5093(97)00391-2).

- [81] C.C. Varvenne, A. Luque, W.A. Curtin, Theory of strengthening in fcc high entropy alloys, *Acta Mater.* 118 (2016) 164–176. <https://doi.org/10.1016/j.actamat.2016.07.040>.
- [82] T. Kostiuchenko, A. V. Ruban, J. Neugebauer, A. Shapeev, F. Körmann, Short-range order in face-centered cubic VCoNi alloys, *Phys. Rev. Mater.* 4 (2020) 113802. <https://doi.org/10.1103/PHYSREVMATERIALS.4.113802/FIGURES/7/MEDIUM>.
- [83] L.R. Owen, H.Y. Playford, H.J. Stone, M.G. Tucker, A new approach to the analysis of short-range order in alloys using total scattering, *Acta Mater.* 115 (2016) 155-166. <https://doi.org/10.1016/j.actamat.2016.05.031>.

## Chapter 4 Strengthening mechanisms in HEA/MEAs

### 4.1 Introduction

The most attractive feature of FCC high- and medium-entropy alloys, a promising class of versatile materials, is their excellent mechanical properties [1–8]. The prototype of FCC HEA, the quinary equiatomic Cr-Mn-Fe-Co-Ni, exhibits extraordinary strength-ductility combinations at ambient and cryogenic temperatures, high temperature-dependence of yield strength, and strength and tensile ductility enhancement with decreasing temperature. Subsequent systematic work [3,9] on Cr-Mn-Fe-Co-Ni and its subsets has revealed that neither the equiatomic composition nor the number of constituent elements is essentially responsible for their good mechanical behaviors. A huge number of studies has been motivated to further improve the strength and/or ductility by developing new non-equiatomic HEAs with different constituent elements. Although in early research the excellent mechanical behaviors of HEA/MEAs are assumed to benefit from the unexpected synergies upon a multi-principle-component mixture (the so-called cocktail-effect), they are not really unprecedented and comparable to those of some conventional solid solution FCC alloys. This suggests that similar strengthening mechanisms may dominate in HEA/MEAs and conventional solid solution alloys, and it is possible to quantitatively determine the mechanical properties of HEAs based on those conventional models.

In dilute binary solid solution alloys, the solid-solution strengthening (SSS) mechanisms have been well-established through the solute-dislocation interaction in terms of atomic size and elastic modulus misfit between solute and solvent atoms [10-15].

Typically, the Fleisher model treats solute atoms as isolated pinning points of dislocations in very dilute alloys (less than 1 at.%), while Labusch considered the statistic distribution of solute-dislocation interaction forces to deal with the spatially dispersed solute atoms in a wider concentration regime (several at.%). Subsequently, the Labusch model was extended to multi-component solid solutions by Gypen and Deruyttere [12,13]. The main assumption of the work was that solutes do not interact with each other or the interaction force was very small compared with solute-dislocation interaction. Then, the size and modulus misfit of each kind of solute were calculated as in the binary system. The model has been successfully applied for the prediction of SSS in FCC Pb-In-Tl alloys up to Pb-12. at% In -23 at.% Tl at 77 K, and in BCC Nb-Hf-Mo at 300 and 77 K.

In FCC HEA/MEAs, the high yield strengths are also mainly attributed to significant SSS effect, excepting for some argument that chemical SRO may also play a role. Toda-Caraballo [16] extended the Gypen and Deruyttere model to HEA/MEAs. Although no clear definition of solute and solvent was involved in the model, each constituent element was actually treated as a kind of solute with respect to the solvent composed of other  $n-1$  element in a  $n$ -component HEA/MEA. The main assumption is that the interatomic distance between element  $i$  and  $j$  is independent for the local environment and the concentration of  $i$  and  $j$ . Based on Embedded Atom Method potential, Varvenne and Curtin [17,18] proposed a predictive theory of yield strength in FCC HEA/MEAs. The HEA/MEAs were simplified into a homogeneous mono-element matrix of average properties (effective matrix) with each constituent element embedded in the effective matrix, which actually treat HEA/MEAs as pseudo-binary alloys. Excepting for these Labusch-type models, an alternative approach to describe SSS in HEA/MEAs arises from their severely distorted crystal lattice due to the interaction of multi-principal elements

with difference atomic sizes. The mean-square atomic displacement (MSAD) was then proposed to quantitate the extent of lattice distortion in HEA/MEAs [19]. The MSAD model does not require to distinguish the solute and solvent elements and exhibits a concise linearly relationship to the SSS in HEA/MEAs. Of important to note is that these mechanisms concern only for the rigid process that the dislocation overcomes the pinning effect of obstacles at 0 K. The real-world yield stress of alloys exhibits temperature and strain-rate dependences, both of which indicate the dislocation motion is thermally activated.

The excellent tensile ductilities of some FCC HEA/MEAs have been attributed to the activation of deformation mechanisms in addition to perfect dislocation glide along with the plastic deformation proceeding, such as the deformation twinning and martensitic transformation, known as the twinning-induced plasticity (TWIP) and transformation-induced plasticity (TRIP) effect [6,8]. In FCC alloys, a low stacking fault energy has been widely accepted as the crucial parameter of TWIP/TRIP effects. A common belief is that the propensity of deformation twinning increase with the decrease of SFE. The critical shear stress for deformation twinning has long believed to monotonically decrease with intrinsic SFE ( $\gamma_{isf}$ ) in FCC metals and alloys since the review by J. A. Venables [20,21], N. Narita [22] and J. W. Christian [23]. De Cooman [24] summarized the empirically critical  $\gamma_{isf}$  values for the occurrence of perfect dislocation glide, deformation twinning and martensitic transformation in review paper of some FCC Fe-Mn-C and Cr-Ni-Fe steels. However, M. J. Szczerba [25] reported that deformation twinning only occurred within an intermedium regime of  $\gamma_{isf}$  and the twinning shear stress increased with the decrease of  $\gamma_{isf}$  in single crystals of a series Cu-

Al alloys. The negative correlation between twinning shear stress and SFE has also been revealed in both polycrystals and single crystals of Cr-Mn-Fe-Co-Ni and Cr-Co-Ni by experimental work [6,8]. In addition, S. Kibey [26,27] reported the critical stress for twinning does not solely depends on the  $\gamma_{isf}$  but on the generalized planer fault energy in FCC metals. H. Huang [28] also reported similar results in Cr-Mn-Fe-Co-Ni, Cr-Mn-Co-Ni, Cr-Co-Fe-Ni and Cr-Co-Ni by theoretical calculations. These results actually reflect the long controversy that the critical stress for twinning is determined either by the nucleation process or the growth process.

On the other hand, the  $\gamma_{isf}$  exhibits significant composition dependence in conventional FCC alloys. Generally, the  $\gamma_{isf}$  decreased upon the addition of most elements in Ni-base and Cu-base binary alloys [29,30]. The valence electron concentration,  $e/a$  ( $e$ : number of valence electrons;  $a$ : number of atoms), was then found to negatively correlate to the  $\gamma_{isf}$  in these FCC binary alloys [20]. The change of  $\gamma_{isf}$  indicates the change in FCC phase stability with respect to HCP phase upon the addition of different elements in binary systems, the extent of which may depends on the electron configuration of these pure metals. In HEA/MEAs, however, it is unclear that whether a specific element will stabilize or unstable the FCC phase under the con-currently alloying of other elements with very high concentrations. For example, Mn is found to effectively decrease the  $\gamma_{isf}$  of Ni-Mn alloys [29] but the  $\gamma_{isf}$  increase with Mn concentration in  $Fe_{80-x}Mn_xCo_{10}Cr_{10}$  MEA [5]. While it is promising to tune the  $\gamma_{isf}$  by tailoring the chemical compositions of the FCC HEAs/MEAs, a definite relationship between  $\gamma_{isf}$  and chemical compositions is still required.

In this chapter, the plastic deformation behavior of single crystals of the equiatomic Cr-Fe-Co-Ni and Fe-Co-Ni MEAs both in tension and in compression as a function of temperature over a wide range 10-300 K, are investigated. The previous results of quinary Cr-Mn-Fe-Co-Ni and ternary Cr-Co-Ni are also included to provide a systematic insight into the SSS effect, Labusch-type thermal activation process, SFE and twinning behavior in FCC HEA/HEAs.

## 4.2 Materials and methods

Button-shaped ingots of the equiatomic Cr-Mn-Fe-Co-Ni, Cr-Fe-Co-Ni, Cr-Co-Ni and Fe-Co-Ni were prepared from high-purity (>99.9%) metals by arc-melting in Ar. All of the ingots were flapped over by 5 time for re-melting to increase the homogeneity and finally combined into rods. Single crystals of Cr-Mn-Fe-Co-Ni were grown from the polycrystalline rods in an alumina crucible in Ar atmosphere at growth rate of 40 mm/h, while single crystals of other three Mn-free alloys were prepared with an optical floating-zone furnace in flowing Ar at a growth rate of 10 mm/h. For subsequent procedures please refer to section 2.2.

For MSAD calculation, the special quasirandom structures (SQS) with a  $3\times 3\times 3$  extension of FCC unit cell were constructed and optimized by the first and second nearest pair correlation functions for all the subsets. The SQS structures were then relaxed until the residual forces became less than  $10^{-3}$  eV/Å.

## 4.3 Results

### 4.3.1 Compression deformation behavior

The temperature dependence of CRSS obtained from  $[\bar{1}23]$ -oriented single crystals of Cr-Fe-Co-Ni and Fe-Co-Ni at a strain rate of  $1 \times 10^{-4} \text{ s}^{-1}$  are plotted between 9-300 K in Fig. 4.1. At room temperature, the CRSS of Cr-Fe-Co-Ni and Fe-Co-Ni are 45.7 MPa and 49 MPa, while at 77 K they increased to 101.9 MPa and 95.3 MPa, respectively. This suggests a higher temperature dependence of CRSS in Cr-Fe-Co-Ni than in Fe-Co-Ni. Similar to that of the Cr-Mn-Fe-Co-Ni [31] and Cr-Co-Ni [32], the values of 0 K CRSS of are Cr-Fe-Co-Ni and Fe-Co-Ni fitted by eq.(3-8) after excluding the results due to the possible inertial effect. The fitted 0 K CRSS and fitting parameters of the present single crystals, together those obtained from [3], are tabulated in Table 4.1.

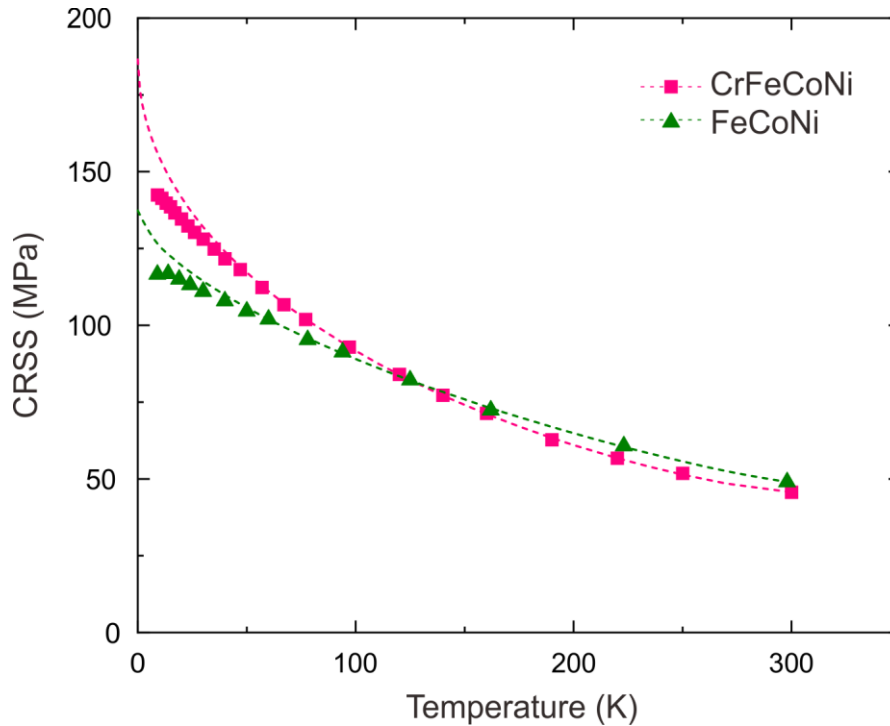


**Fig. 4.1** Temperature dependence of CRSS for  $(111)[\bar{1}01]$  slip in the Cr-Fe-Co-Ni and Fe-Co-Ni.

**Table 4.1** The 0 K CRSS and fitting parameter  $p$  and  $q$  for HEA and MEAs of the Cr-Mn-Fe-Co-Ni system.

	$\tau_0$ /MPa	$p$	$q$
Cr-Mn-Fe-Co-Ni	168	0.26	1.15
polycrystals	172	0.43	1.15
Cr-Fe-Co-Ni	187	0.76	1.98
polycrystals	209	0.37	1.17
Cr-Co-Ni	225	0.51	1.56
polycrystals	215	0.42	1.11
Fe-Co-Ni	137	0.87	1.56
polycrystals	133	0.47	1.08

From Table 4.1, the  $p$  and  $q$  values are closed 1/2 and 3/2, respectively, which implies the size misfit is the main resistance mechanism of dislocation motion according to Ashby et al [33]. Note that the obtained CRSS at 0 K of single crystals are somewhat comparable to those of polycrystals excepting for the Cr-Fe-Co-Ni.

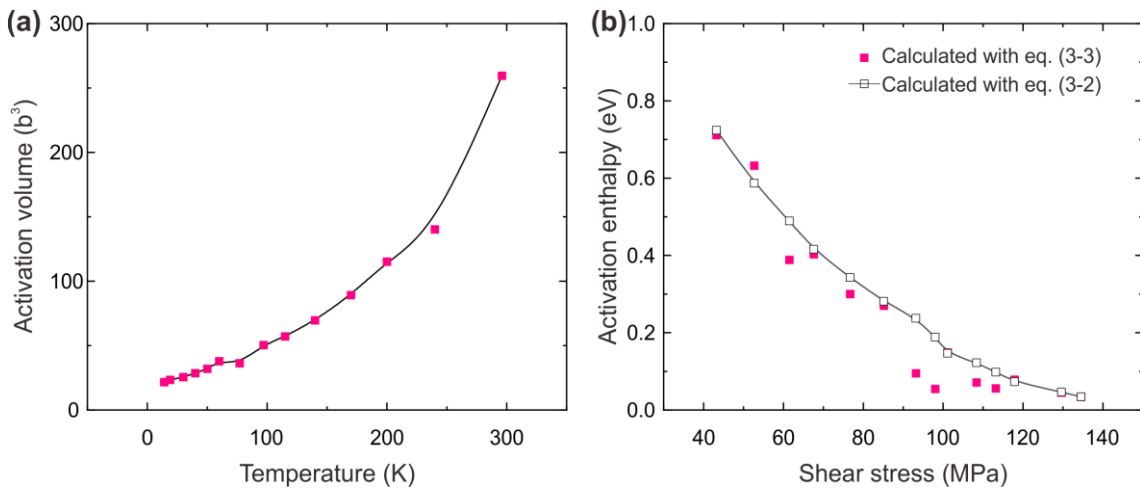


**Fig. 4.2** Shear stress dependence of activation enthalpy for deformation in the Cr-Fe-Co-Ni MEA calculated using equation (3-2) with  $C=10^8 \text{ s}^{-1}$  and equation (3-3).

The activation volume and activation enthalpy of deformation in the Cr-Fe-Co-Ni are shown in Fig. 4.2(a) and Fig. 4.2(b), respectively. The activation volume is  $40 b^3$  at 77 K and increases to  $260 b^3$  at room temperature. While the activation volume at 77 K is comparable to those of Cr-Mn-Fe-Co-Ni ( $40 b^3$ ) and Cr-Co-Ni ( $36 b^3$ ), it is quite different at room temperature (Cr-Mn-Fe-Co-Ni  $233 b^3$  [31], Cr-Co-Ni  $130 b^3$  [32]). This suggests that the Cr-Fe-Co-Ni has a relatively low temperature dependence of CRSS thus relatively larger activation volumes when compared with the Cr-Mn-Fe-Co-Ni and Cr-Co-Ni. The calculated activation enthalpy at the shear stress 45.7 MPa (300 K, strain rate  $1 \times 10^{-4} \text{ s}^{-1}$ ) is 0.70 eV, comparable to that (0.61 eV) of Cr-Co-Ni [32], both are consistent with the generally belief that conventional FCC solid-solution alloys have a roughly constant activation enthalpy (around 0.6-0.7 eV) at room temperature.

### 4.3.2 Tensile deformation behavior

Engineering stress-strain curves of the Cr-Fe-Co-Ni and Fe-Co-Ni single crystals tested at a constant engineering strain rate of  $1 \times 10^{-4} \text{ s}^{-1}$  at room temperature are shown in Fig. 4.3(a), the true stress-strain and corresponding work hardening rate (WHR) curves are plotted in Fig. 4.3(b) and 4.3(c), respectively. At room temperature, no significant inflection point is observed in the stress-strain curves for two MEAs, which is similar to that of the Cr-Mn-Fe-Co-Ni HEA [31] but different with the Cr-Co-Ni [32]. No sudden WHR drop occurs in the curves until fracture, which suggest that no additional deformation mechanism was activated during the tensile deformation. The EBSD examinations in Fig. 4.3(d) for Cr-Fe-Co-Ni and 4.3(e) for Fe-Co-Ni after fracture also confirmed that no deformation twinning occurred. At room temperature, the total elongation of Cr-Fe-Co-Ni is about 175%, which is significant higher than that (115%)

of the Fe-Co-Ni. Correspondingly, the WHR of the former is higher within the plastic deformation range. Since there is no deformation twinning in these two specimen, it should be attributed to the difference in cross-slip frequency, which will affect the dislocation pile-ups and densities.

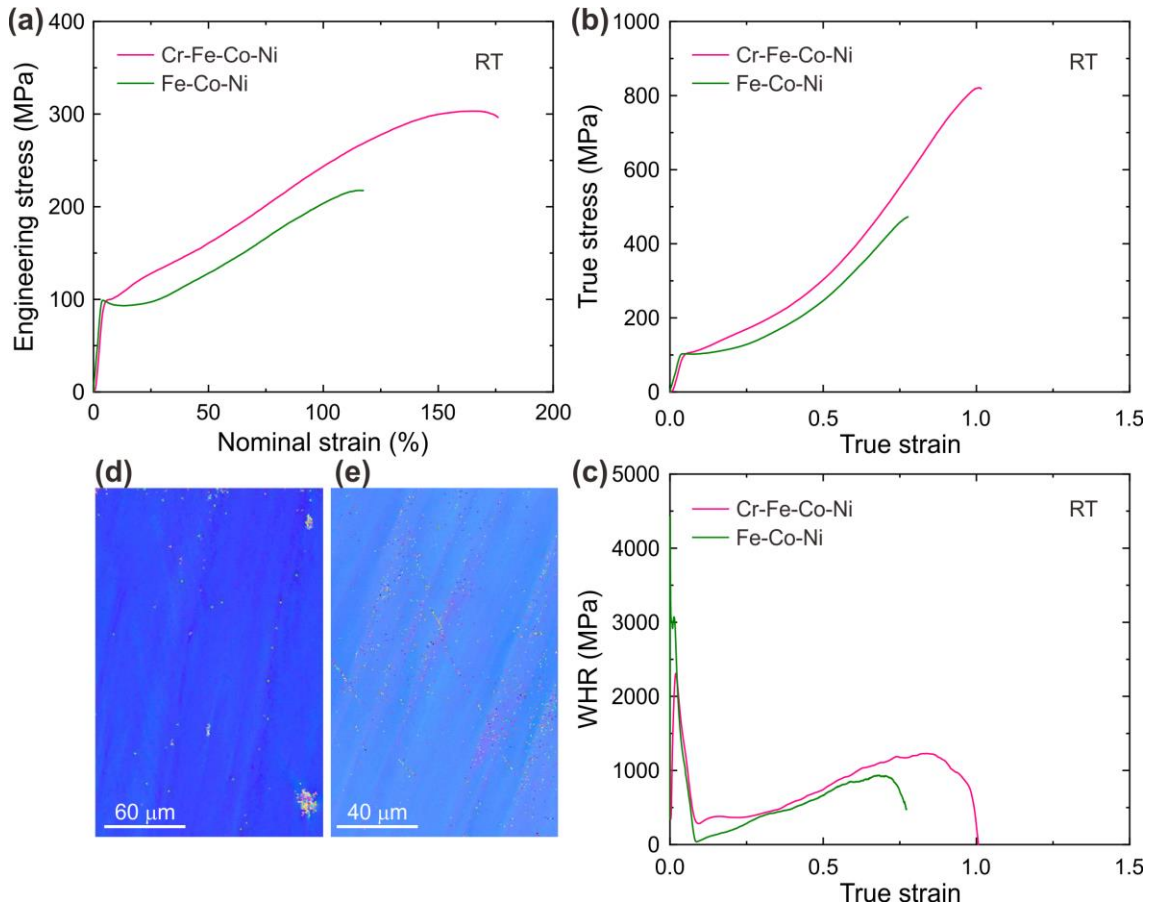


**Fig. 4.3** (a) Engineering stress-engineering strain curves, (b) true stress-true strain curves and (c) work hardening rate obtained for  $[\bar{1}23]$ -oriented single crystals of the Cr-Fe-Co-Ni and Fe-Co-Ni MEA deformed in tension to failure at room temperature. EBSD results of (d) Cr-Fe-Co-Ni and (e) Fe-Co-Ni did not detect deformation twins.

At 77 K, for Fe-Co-Ni, still no inflection point is observed on the stress-strain curves, but the total elongation increased from 115% at RT to 150%, which should also be attributed to the slightly higher WHR at 77 K although still no deformation twinning occurred until fracture, as shown in the EBSD image in Fig. 4.4(e). The increased WHR

may also be related to the decrease in the frequency of cross-slip at 77 K, since cross slip is a thermally activated process. For Cr-Fe-Co-Ni, the total elongation increased dramatically from 150% at RT to 230% at 77 K. The EBSD examination confirmed the occurrence of deformation twinning in the specimen after fracture (Fig. 4.4 (d)). An obvious inflection point is observed at the engineering strain level of 108%, which corresponds to the sudden WHR drop at a true strain level 0.73. The twinning stress is

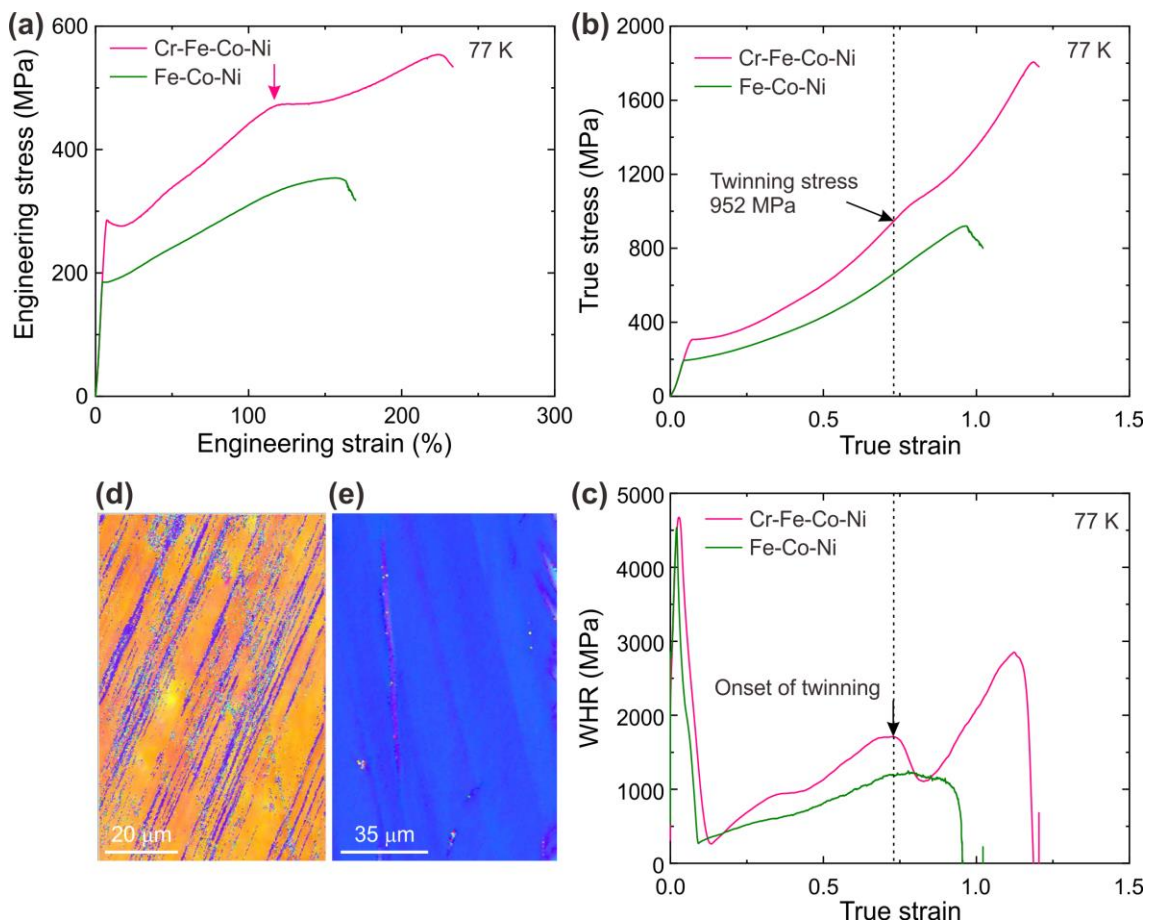


**Fig. 4.4** (a) Engineering stress-engineering strain curves, (b) true stress-true strain curves and (c) work hardening rate obtained for  $[\bar{1}23]$ -oriented single crystals of the Cr-Fe-Co-Ni and Fe-Co-Ni MEA deformed in tension to failure at 77 K. Deformation twinning occurred in the Cr-Fe-Co-Ni (d) but not in Fe-Co-Ni.

thus determined to be 952 MPa. According to the previous work [34], the load axis direction where twinning occurred was  $[\bar{1}\bar{3} \ 12 \ 25]$ , the Schmid factor for  $(\bar{1} \ \bar{1} \ 1)[\bar{1} \ 21]$  conjugate twinning is 0.405, so the twinning shear stress is 386 MPa.

## 4.4 Discussion

### 4.4.1 Solid solution strengthening in HEA/MEAs

In Labusch model [11], the SSS  $\tau_{SS}$  can be expressed as

$$\tau_{SS} = \mu \varepsilon_i^{4/3} c_i^{2/3} Z \quad (4-1)$$

where  $\mu$  is the shear modulus of the alloy,  $c_i$  is the atomic fraction of element  $i$ ,  $Z$  is a fitting parameter,  $\varepsilon_i$  is the mismatch parameter accounts for modulus misfit  $\eta'_i$  and size misfit  $\xi_i$  as

$$\varepsilon_i = (\eta_i'^2 + \omega^2 \xi_i^2)^{1/2} \quad (4-2)$$

where

$$\eta'_i = \frac{\eta_i}{1 + 0.5\eta_i}; \eta_i = \frac{d\mu}{dc_i} \frac{1}{\mu}; \xi_i = \frac{da}{dc_i} \frac{1}{a} \quad (4-3)$$

$a$  is the lattice parameter of the alloy and  $\omega$  describes the difference of the interaction force between screw and edge dislocation with the foreign atoms. Then, the overall SSS in HEAs is

$$\tau_{SS} = \sum_{i=1}^n \left[ (\mu \varepsilon_i^{3/4} Z)^{3/2} c_i \right]^{2/3} \quad (4-4)$$

To estimate the SSS at HEAs, the size and modulus misfit parameters are necessary. For modulus misfit parameter,  $\eta_i$  can be estimated as

$$\eta_i = 2 \frac{\mu_i - \mu_{HEA}}{\mu_i + \mu_{HEA}} \quad (4-5)$$

For size misfit, the lattice parameter of a binary alloy can be calculated by [35]

$$a_{bin} = \left( a^3 + 4\pi r^3 c_i \frac{n}{\mathcal{G}} \zeta A \right)^{1/3} \left( \frac{n_i \mathcal{G}}{n \mathcal{G}_i} \right)^{1/3} \quad (4-6)$$

where  $r$  is the Wigner-Seitz atomic radius,  $n$  is number of atoms in a unit cell,  $\mathcal{G}$  depends on crystal structure ( $\mathcal{G} = 1$  for cubic lattices).  $\zeta$  and  $A$  are constant defined as

$$\zeta = 1 + \frac{4\mu}{3\kappa}; \zeta_i = 1 + \frac{4\mu_i}{3\kappa_i}; A = \frac{1}{\zeta_i} \frac{r_i - r}{r} \quad (4-7)$$

Note that the lattice parameter of a binary alloy can also be estimated by

$$a_{bin} = \frac{s_{bin}^{ave}}{f_p} \quad (4-8)$$

where  $s^{ave}$  is the average interatomic distance,  $f_p$  is the packing factor. According to Moreen, the average interatomic distance  $s^{ave}$  can be expressed as

$$s_{bin}^{ave} = s_{ii} c_i^2 + 2s_{ij} c_i (1 - c_i) + s_{jj} (1 - c_i)^2 \quad (4-9)$$

Here,  $s_{ii}$ ,  $s_{ij}$  and  $s_{jj}$  denotes the interatomic distance for solute-solute, solute-solvent and solvent-solvent, respectively. The  $s_{ii}$  and  $s_{jj}$  are assumed to be the interatomic distance of the pure metals. Combined eq. (4-7) and (4-8), the interatomic distance of all the binaries can be estimated, and then the average interatomic distance of the HEAs is

$$s_{HEA}^{ave} = \sum_{i=1}^n \sum_{j=1}^n s_{ij} c_i c_j \quad (4-10)$$

Toda-Caraballo [16] propose a sampler way to calculate the  $s_{ij}$  as

$$s_{ij} = \frac{\Delta s}{2} + s_{ii}; \Delta s = \frac{s_{bin}^{ave} - s_{ii}}{1 - c_i} \quad (4-11)$$

The necessary parameters at room temperature for the modulus and size misfit parameters are tabulated in Table 4.2. It should be clarified here that all the above calculations are considered at 0 K. Even though some of the parameters themselves (like lattice parameter and shear modulus) in Table 4.2 exhibit weak temperature dependence, the composition dependence of these parameters is supposed to temperature-independent.

**Table 4.2** Crystal structure, lattice parameter, Wigner-Seitz atomic radii ( $r$ ), shear modulus and bulk modulus for Cr, Mn, Fe, Co, Ni at room temperature

Element	Lattice	$\frac{a}{c}$ (Å)	$r$ (Å)	$\mu$ (GPa)	$\kappa$ (GPa)
Cr	BCC	2.8850	1.4205	115	160.0
Mn	Cubic	8.9140	1.4286	81	120.0
Fe	BCC	2.8665	1.4114	82	163.0
Co	HCP	2.5071	1.3827	75	186.0
		4.0686			
Ni	FCC	3.5240	1.3772	76	185.5

The main assumption in the above analytical calculation is that the interatomic distance  $s_{ij}$  does not depend on the composition of the alloy. For example, the  $s_{Cr-Ni}$  is assumed to be the same (or very small variation) in all of the HEAs that contain Cr and Ni, which equals to the  $s_{Cr-Ni}$  calculated by the above equations in Cr-50 at. % Ni binary alloy. However, whether this assumption still holds true or not in HEAs is unclear considering the severe and ubiquitous lattice distortion in HEAs. Previous work has shown that the lattice distortion of FCC HEAs varies significantly depending on the local environment, i.e. the element combination of the alloys.

An alternative way to calculate the size misfit parameter is quite straightforward as

$$\xi_i = \frac{da}{dc_i} \frac{1}{a} = \frac{a_{HEA+i} - a_{HEA}}{c_i} \frac{1}{a_{HEA+i}} \quad (4-12)$$

This equation directly calculates the variation of lattice parameter due to the addition of one new constituent element  $i$  with the concentration  $c_i$ . For example, the lattice

**Table 4.3** The calculated lattice parameter for equiatomic binary, ternary, quaternary and quinary HEA/MEAs.

Alloys	a (Å)
CrFe	3.52163
CrCo	3.51588
CrNi	3.54596
MnFe	3.46746
MnCo	3.46455
MnNi	3.49535
FeCo	3.44397
FeNi	3.47532
CoNi	3.47782
CrMnFe	3.51137
CrMnCo	3.50886
CrMnNi	3.52724
CrFeCo	3.49226
CrFeNi	3.51097
CrCoNi	3.50966
MnFeCo	3.45784
MnFeNi	3.47839
MnCoNi	3.47764
FeCoNi	3.46561
CrMnFeCo	3.49190
CrMnFeNi	3.50582
CrMnCoNi	3.50582
CrFeCoNi	3.49378
MnFeCoNi	3.47004
CrMnFeCoNi	3.49395

parameters of equiatomic Cr-Co, Cr-Ni and Co-Ni are  $a_{Cr-Co}$ ,  $a_{Cr-Ni}$ , and  $a_{Co-Ni}$ , respectively. After the addition of Ni, Co and Cr, the equiatomic Cr-Co-Ni possesses a new lattice parameter  $a_{Cr-Co-Ni}$ . Then, the size misfit upon the solid solution of Ni, Co and Cr can be calculated by eq. (4-12). Therefore, to estimate the size misfit of all the constituent elements, the lattice parameters of all the binary, ternary, quaternary subsets are necessary. Since some of these subsets do not possess FCC structure and even not single phase, the lattice parameters of all the subsets are estimated by first principle calculation. The lattice parameters are tabulated in Table 4.3. There are several advantages to estimate the size misfit by first principle calculation. Firstly, all the lattice parameters are obtained at 0 K thus it is not necessary to assume the temperature-independence of size misfit. Second, interatomic distance of each binaries, which may not be exactly the same in all HEAs, is not required as an intermedia variable to calculate the lattice parameters of HEAs. The main concern is that a fixed global FCC lattice is assumed for all the SQS structures. Even though the calculations were terminated when the convergence of total energy was reached, it does not mean that the alloy is most stable with the assumed FCC structure.

The calculated mismatch parameter  $\varepsilon_i$  by eq.(4-2) is shown in Fig. 4.5. Note that the vertical axes of contribution are with arbitrary unit and only the relative values are meaningful. In the case of edge-dislocation dominated strengthening ( $\omega=16$ , Fig. 4.5 (a)), the size misfit predominates the SSS in all of the HEAs. For those HEAs contains Cr, the modulus misfit contribution is of minor significance but increases with the Cr concentration. For those HEAs contains Mn but without Cr (MnFeCoNi, MnCoNi, MnFeNi), the modulus misfit rarely contribute to the SSS. In addition, assuming an edge- and screw-dislocation jointly dominating by setting  $\omega=10$ , the contribution of modulus

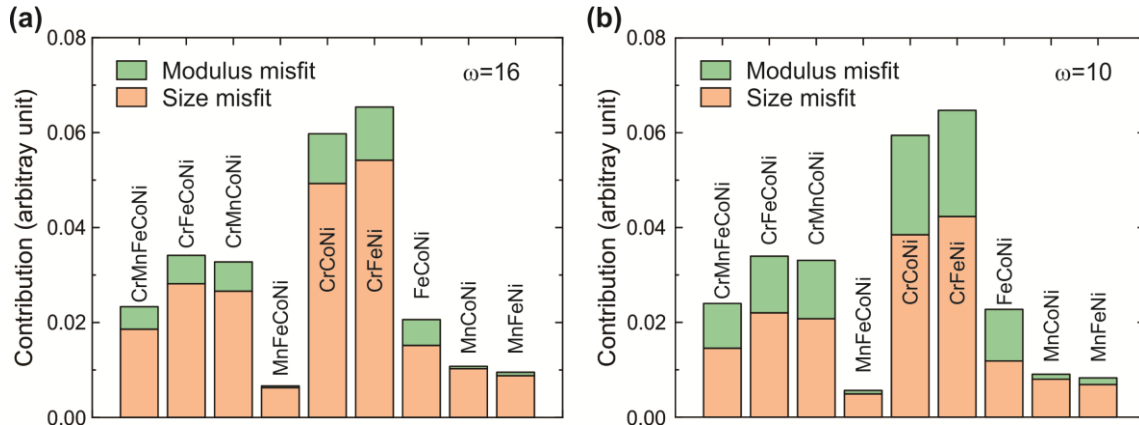


**Fig. 4.5** The contribution of size and modulus misfit to SSS in FCC HEA/MEAs with (a)  $\omega=16$  and (b)  $\omega=10$ .

misfit becomes significant and nonnegligible for most of the FCC HEAs, as shown in Fig. 4.5 (b). According to P. Haasen [36], for screw dislocation  $\omega=3$ , which implies that modulus misfit may overwhelm the size misfit and contribute to the SSS most significantly in screw dislocation dominated solid solution.

Furthermore, the contribution to SSS of each element can also be quantitatively described in terms of size and modulus misfit. Fig. 4.6 shown the contribution of each element for the present four HEA/MEAs. Here  $\omega$  is set to be 16 for edge-dislocation dominating. A noticeable feature is that Cr is of great significance to SSS in size misfit term in the three Cr-containing HEA/MEAs, being consistent with the results of Fig. 4.5 (a). In addition, the Cr also affect the modulus misfit term remarkably, which may be related to the change of isotropic elastic coefficients upon the Cr addition. Table 4.4 lists the Cauchy pressure of some HEA/MEAs and pure metals [37-40]. The decrease of Cauchy pressure is believed to imply the tendency to form directional bonding even in solid solutions [40,41]. This will influence the anisotropy of the alloy and thus the modulus misfit interaction. It requires more investigation.

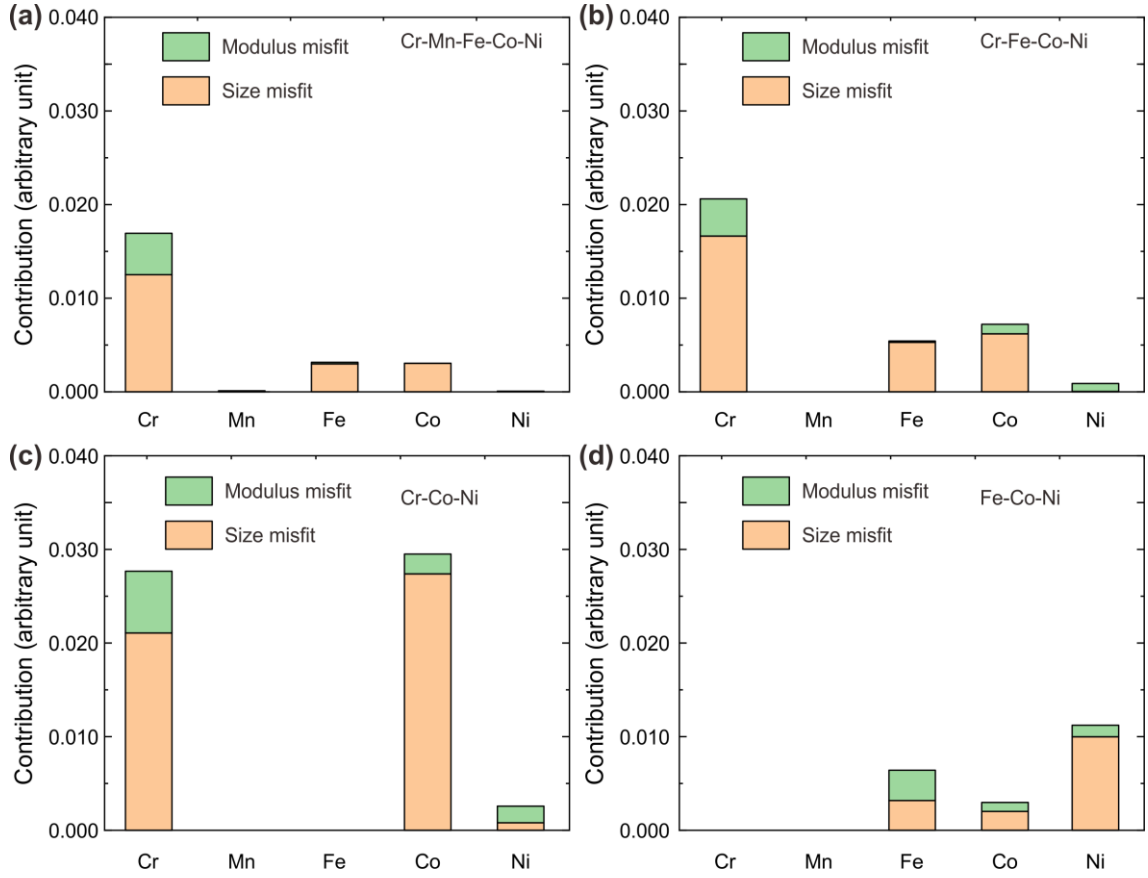


**Fig. 4.6** The contribution of size and modulus misfit to SSS for each element in FCC HEA/MEAs (a) Cr-Mn-Fe-Co-Ni, (b) Cr-Fe-Co-Ni, (c) Cr-Co-Ni and (d) Fe-Co-Ni.

**Table 4.4** The isotropic elastic coefficients of the four HEA/MEAs [37-40].

	$C_{11}$ (GPa)	$C_{12}$ (GPa)	$C_{44}$ (GPa)	$\mu$ (GPa)	$C_{12}-C_{44}$ (GPa)
Cr-Mn-Fe-Co-Ni	192.1	117.6	122.3	76.1	-4.8
Cr-Fe-Co-Ni	257	85	86	86	-1
Cr-Co-Ni	251	148	152.3	87	-4.3
Fe-Co-Ni	227	91	68	68	23
Cr	380	161	77	115	84
Co	260	165	102	75	63
Ni	262	155	122	76	33

Using the size and modulus misfit parameter, the  $\tau_{SS}$  of the four HEA/MEAs are calculated by eq. (4-4) and plotted against the CRSS at 0 K ( $\tau_0$ ) of single crystals obtained in this work, as shown in Fig. 4.7. Since there is no clear definition of a “base” metal in HEA/MEAs, the predicted CRSS cannot be easily obtained. However, the calculated SSS  $\tau_{SS}$  are still comparable to the experimental 0 K CRSS, indicating that the traditional Labusch-type SSS theory may be also applicable in HEA/MEAs. Deviation may come from the calculation of lattice constants of each subsets with a fixed FCC structure.

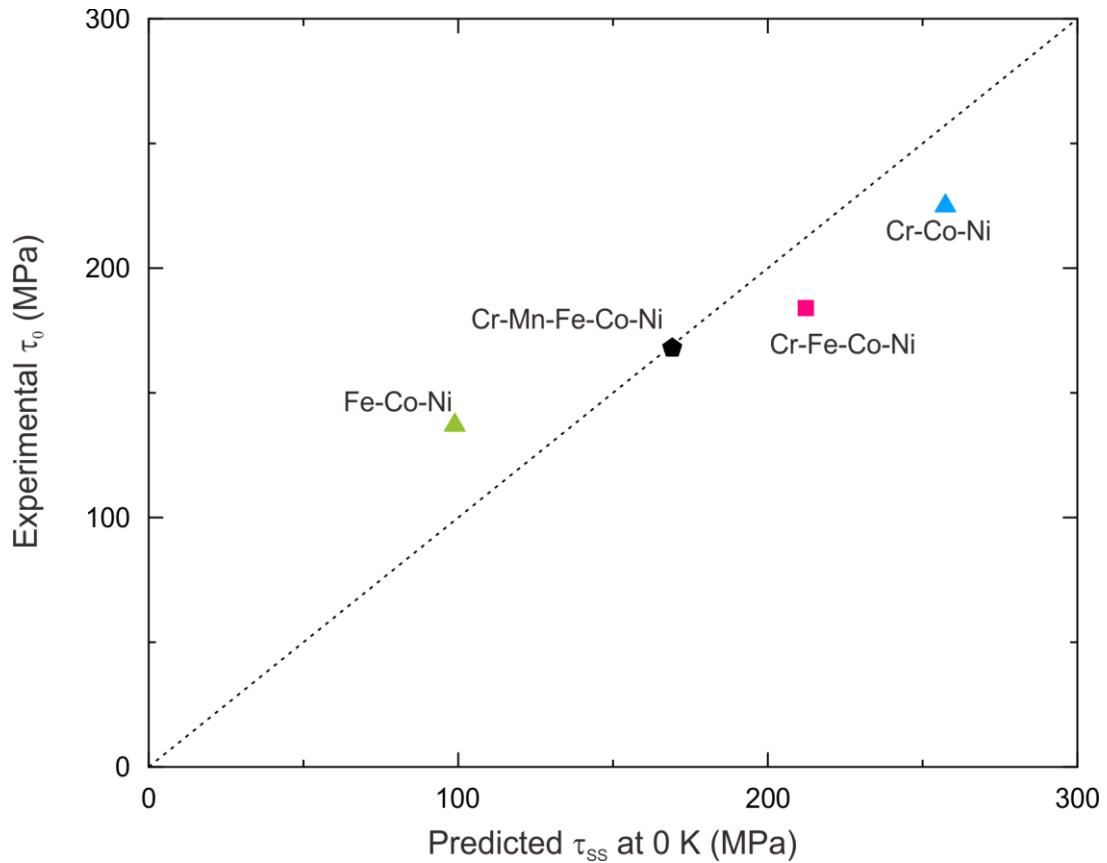


**Fig. 4.7** The deduced CRSS at 0 K of single crystals plotted against the SSS calculated by Labusch-type theory for each element in FCC HEA/MEAs.

#### 4.4.2 Mean-square atomic displacement

The SSS in HEA/MEAs of the Cr-Mn-Fe-Co-Ni system is also evaluated by the MSAD model. The MSADs for Cr, Mn, Fe, Co and Ni atoms obtained from SQSs of the four HEA/MEAs are listed in Table 4.5, and the CRSS at 0 K (seen in Table 4.1) normalized by shear modulus are plotted as a function of the square root of MSAD normalized by Burgers vector  $b$  in Fig. 4.8. Basically, the SSS increase with the normalized MSAD values. The deviation of the Fe-Co-Ni may be related to the strong magnetic effect of Fe, Co and Ni which is taken into account for the MSAD calculation. The Cr and Mn exhibit bigger MSAD values among these five elements and Cr is of the greatest significance to the average MSAD, which indicates that Cr is the crucial element in SSS in these HEA/MEAs. While this is consistent with the Labusch-type SSS calculation, the role of Mn in these two models is completely different. In the Labusch-type model, Mn is of minor significance even less than Fe and Co, while in MSAD model the contribution of Mn is only less than Cr. More results of Cr/Mn contained HEA/MEAs are required to make a definite conclusion.

**Table 4.5** The MSADs (in pm<sup>2</sup>) for Cr, Mn, Fe, Co and Ni atoms obtained from SQSs of the four HEA/MEAs.

	Cr	Mn	Fe	Co	Ni	Ave.
Cr-Mn-Fe-Co-Ni	72.5	43.3	31.3	16.1	8.2	34.3
Cr-Fe-Co-Ni	78.5	-	36.2	20.6	12	36.9
Cr-Co-Ni	86.2		-	30.4	19.6	45.4
Fe-Co-Ni	-	-	22.3	11.9	a	12.7

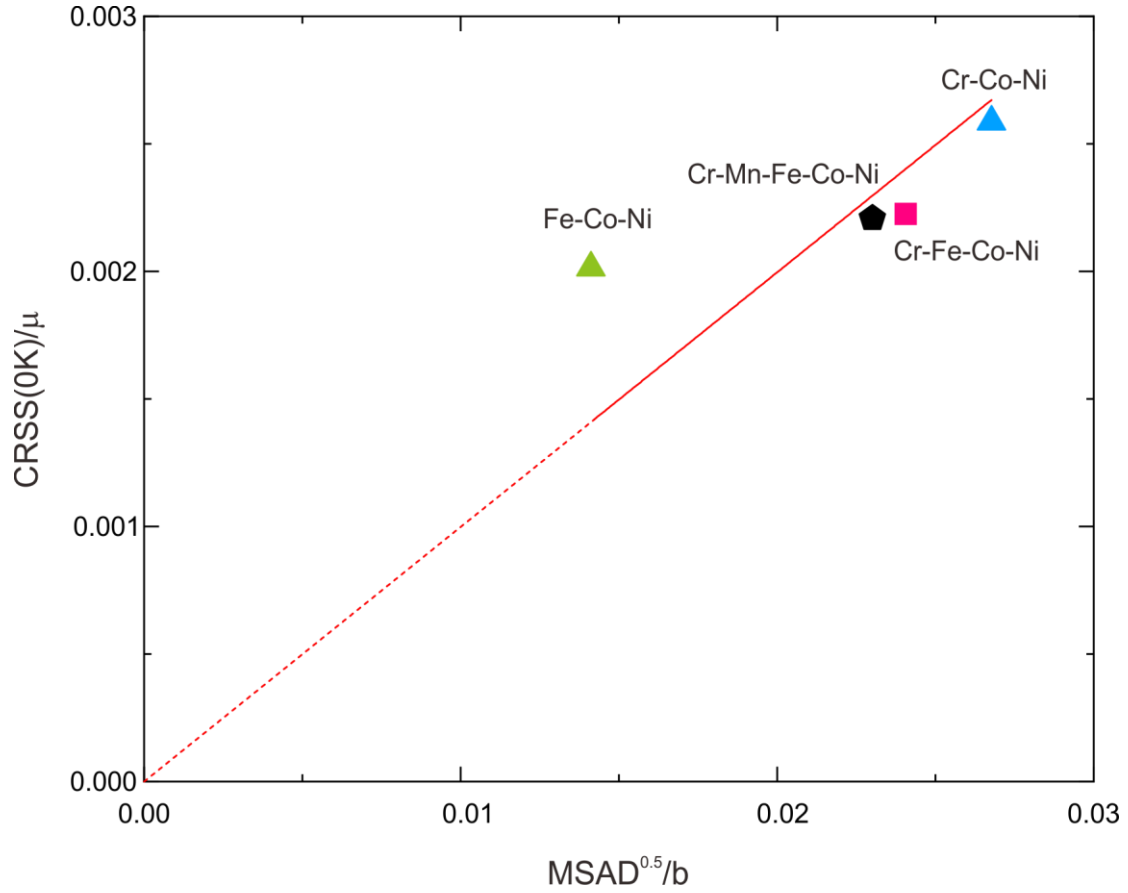


**Fig. 4.8** The CRSS at 0 K of single crystals normalized by shear modulus as a function of the MSAD<sup>0.5</sup> normalized by Burgers vector.

To further elucidated the contribution of Cr and Mn in these HEA/MEAs, the binding energy of an edge-dislocation segment and solute atoms, the activation volume at 0 K are estimated. According to Butt [14,15], the temperature dependence of CRSS of solid solutions can also be expressed as

$$\tau = \tau_0 \exp(-mkT / W_0) \quad (4-13)$$

where  $k$  is the Boltzmann constant,  $T$  is the deformation temperature,  $W_0$  is the binding energy of an edge-dislocation segment with the solute atoms close to it.  $m$  is a constant and can be calculated by

$$m = \ln \frac{\dot{\gamma}_0}{\dot{\gamma}} \quad (4-14)$$

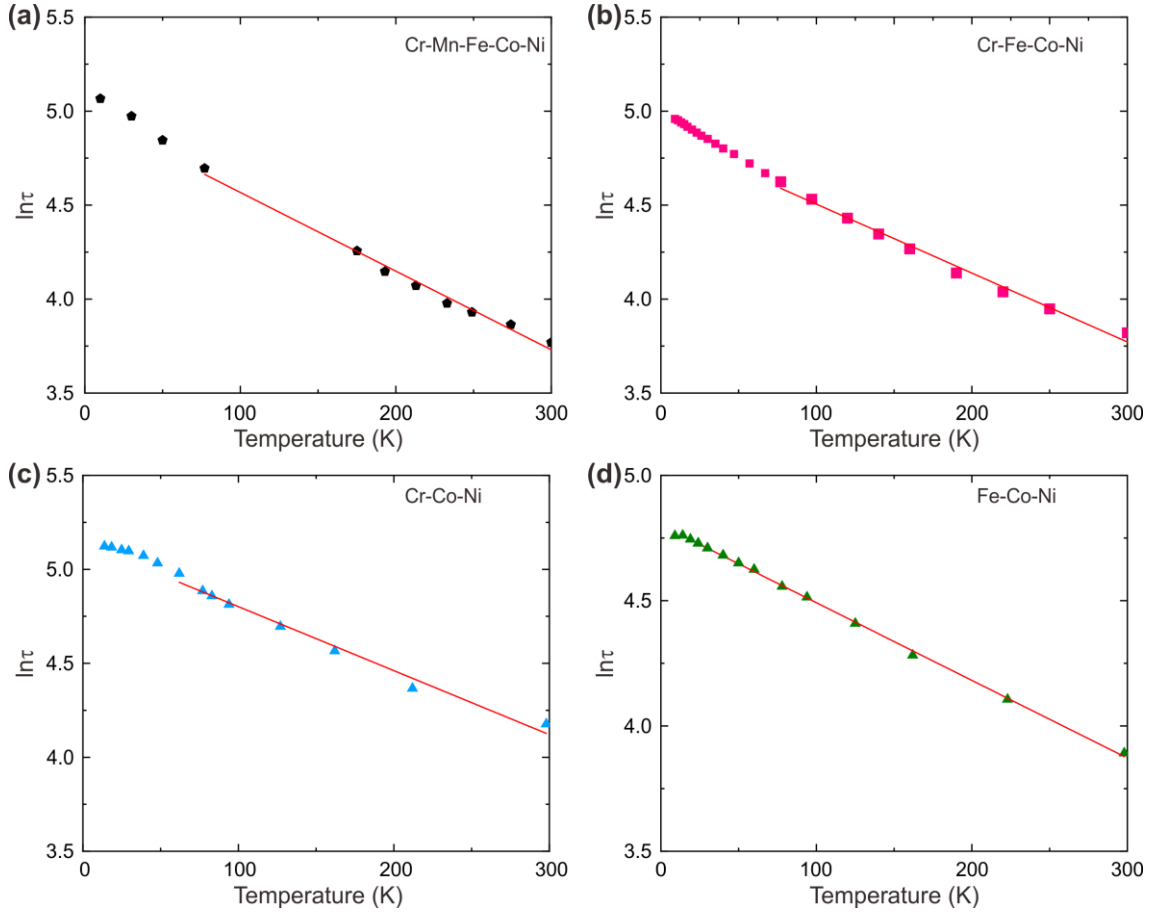


**Fig. 4.9** The logarithm of CRSS plotted as a function of deformation temperature for (a) Cr-Mn-Fe-Co-Ni, (b) Cr-Fe-Co-Ni, (c) Cr-Co-Ni and (d) Fe-Co-Ni. Possible inertial effect is excluded from the fitting.

Here  $\dot{\gamma}$  is the experimental strain rate,  $\dot{\gamma}_0$  is the reference strain rate which can be taken as  $10^8 \text{ s}^{-1}$  or estimated from the following equation [42]

$$\dot{\gamma}_0 = \frac{2\pi\tau \nu b}{\mu l} \quad (4-15)$$

Here  $\nu$  is activation volume,  $l$  is the typical dislocation slip distance which can be estimated from the activation volume.

Following eq. (4-13)-(4-15), the logarithm of the CRSS are plotted as the function of deformation temperatures of the four HEA/MEAs, as shown in Fig. 4.9. The binding

energy  $W_0$  is calculated from the slopes of the fitting curves. In addition, Butt [14,15] also suggested that for a specific alloy, the activation volume depends on the CRSS so that

$$W_0 = \tau_0 \nu_0 = \tau \nu \quad (4-16)$$

By eq. (4-16) the activation volume at 0 K can also be estimated. All these parameters are tabulated in Table 4.6.

**Table 4.6** The Cr/Mn concentrations, activation volume and CRSS at 0 K and binding energy between edge dislocation and solutes for four HEA/MEAs.

	Cr-Mn-Fe-Co-Ni	Cr-Fe-Co-Ni	Cr-Co-Ni	Fe-Co-Ni
$c_{Cr}$	0.2	0.25	0.33	0
$c_{Mn}$	0.2	0	0	0
$\tau_0$ (MPa)	168	187	225	137
$W_0$ (eV)	0.575	0.655	0.743	0.786
$\nu_0$ (b <sup>3</sup> )	33.3	47.6	33.2	57.2

#### 4.4.3 SFE and ductility of HEA/MEAs

The tensile stress-strain curves of  $[\bar{1}23]$ -oriented single crystals of the four alloys deformation at 77 K are summarized in Fig. 4.10. The total elongation is Cr-Co-Ni > Cr-Fe-Co-Ni > Cr-Mn-Fe-Co-Ni > Fe-Co-Ni, although the difference between Cr-Fe-Co-Ni and Cr-Mn-Fe-Co-Ni is not significant. The increase in total elongation should be attributed to the activation of additional deformation mechanisms along with the decrease of SFE, as illustrated in Fig. 4.11. This is similar to that in TWIP steels reviewed by De Cooman [24], although there is not definitely critical  $\gamma_{isf}$  values for each stage since the results are insufficient.  $\gamma_{isf}$  is an effective material parameter to tailor the deformation performance also in HEA/MEAs.

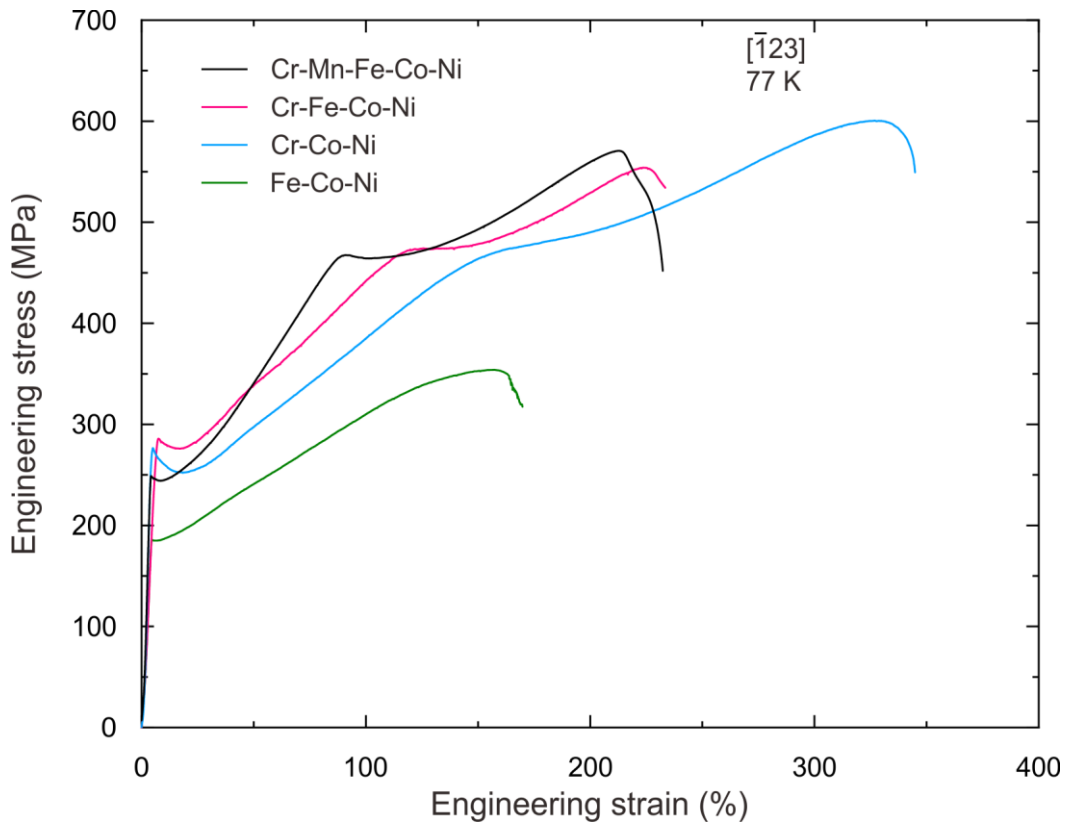


**Fig. 4.10** Engineering stress-engineering strain curves obtained for  $[\bar{1}23]$ -oriented single crystals of the Cr-Mn-Fe-Co-Ni, Cr-Fe-Co-Ni, Cr-Co-Ni and Fe-Co-Ni MEA deformed in tension to failure at 77 K.

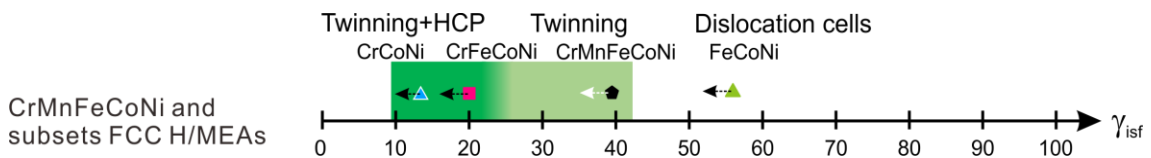


**Fig. 4.11** Rough ranges of the intrinsic stacking fault energy SFE for dislocation glide, deformation twinning and phase transformation in FCC HEA/ MEAs at 77 K. The dashed arrows indicate the possible SFE at 77 K.

There is a long belief that the  $\gamma_{isf}$  of solid solutions is closely related to the valence electron to atom ratio. In HEA/MEAs, the valence electron concentration (VEC) is used and may be related to  $\gamma_{isf}$ . The  $\gamma_{isf}$  of several HEA/MEAs including binary Fe-Ni, Co-Ni and pure Ni are plotted as the function of their VEC in Fig. 4.12(a). There is no clear correlation between  $\gamma_{isf}$  and VEC in these alloys. Roughly, the  $\gamma_{isf}$  increase with the

VEC, which is opposite to the trend in some conventional binary alloys. In Fig. 4.12(b), the  $\gamma_{isf}$  of these alloys are fitted linearly with their compositions as the following equation

$$\gamma_{isf} = -74c_{Cr} + 22c_{Mn} + 74c_{Fe} - 34c_{Co} + 126c_{Ni} \quad (4-17)$$

The fitting exhibits a good agreement with the  $\gamma_{isf}$  in this work or from literature results. Although the physical meaning of eq. (4-17) is not clear yet, it remains a use tool to control the  $\gamma_{isf}$  by tailoring the chemical composition.

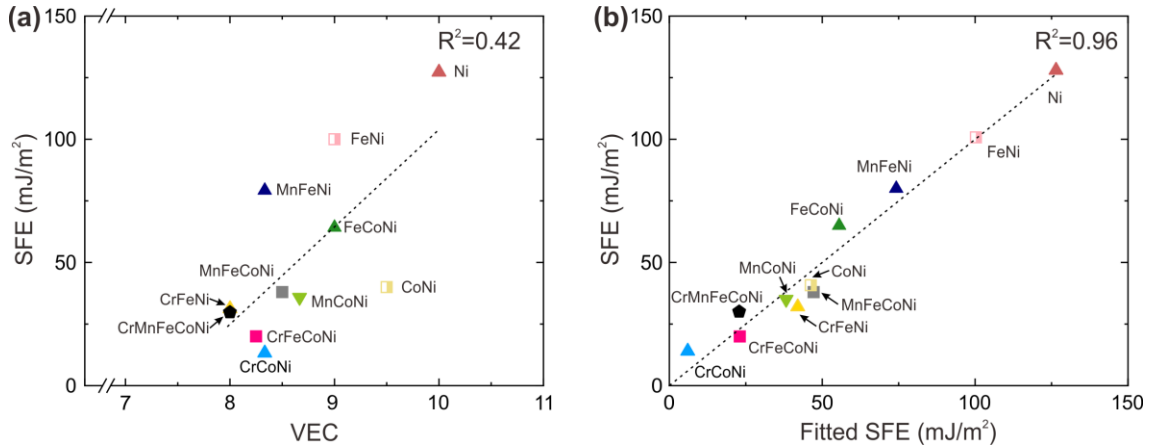


**Fig. 4.12** The SFE values of several HEA/MEAs and pure Ni plotted against (a) VEC values and (b) fitting values determined from chemical compositions. Some SFE values are from [43,44].

Fig. 4.13 summarizes the relationship between twinning shear stress and SFE in the present HEA/MEAs and some Cu-Al binary alloys [20]. The general belief is that a lower SFE will decrease the critical twinning stress. However, the opposite trend is observed in this work of the single crystals of three HEA/MEAs, which has also been reported in polycrystals [6,8]. Recently, M. J. Szczerba [25] reported that deformation twinning shear stress increased with the decrease of SFE in single crystals of a series Cu-Al alloys, and once the SFE is lower than a critical value (about 4 mJ/m<sup>2</sup>), no twinning is observed.

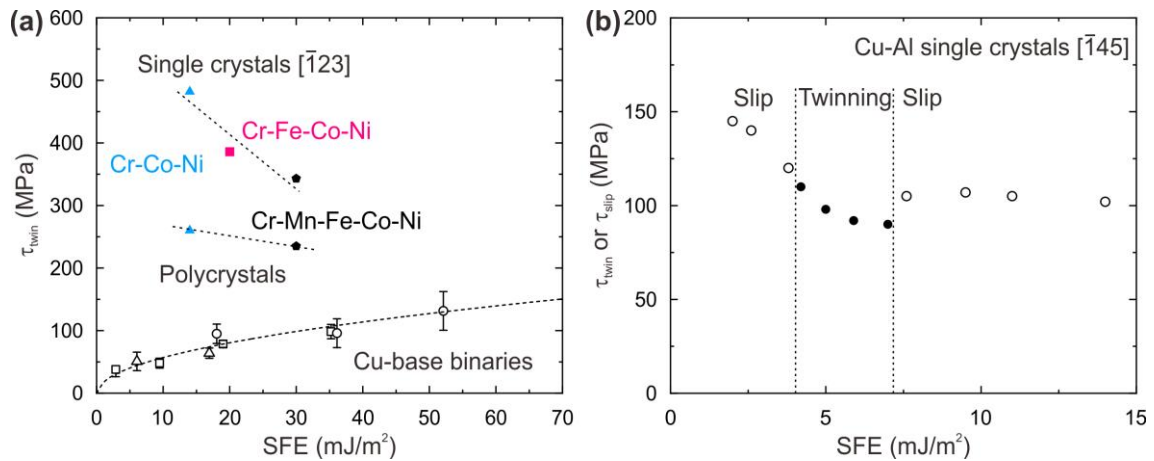


**Fig. 4.13** The twinning shear stress plotted as a function of SFE in (a) Cu-base binaries [20] and HEA/MEAs [6,8,31,32] (b) a series of Cu-Al alloys from [25].

In FCC alloys, it has been widely accepted that deformation twinning usually occur due to the motion of partial dislocations. With a low SFE, the partials distance will increase, thus the energy required to rebound partials into perfect dislocations is high and the frequency of cross-slip is decrease. Therefore, with a low SFE the activation of partial dislocation is energetically easier. However, this process only considered the nucleation of twin embryo with a few atomic layers thickness, and it does not essentially result in a lower macro twinning stress. From the experimental term, the onset of deformation twinning may be easily judged from the load drop, inflection point and/or click sound during the mechanical tests. These phenomena accompanied with twinning may require relative thicker twins (not only embryo) with sufficient volume fraction, i.e. the growth of twin embryos. This means that the macroscopic twinning stress, deduced from the stress-strain curves, should correspond to the twin growth instead of nucleation process. With a low SFE, most dislocation will array in their slip planes and the cross slip is less frequent, resulting a very high forest dislocation density with respect to the dominating

slip or twinning system. The high-density forest dislocations will in turn hinder the propagation of twin embryos.

## 4.5 Conclusions

The plastic deformation behavior of single crystals of the equiatomic Cr-Mn-Fe-Co-Ni, Cr-Fe-Co-Ni Cr-Co-Ni and Fe-Co-Ni MEAs both in tension and in compression as a function of temperature over a wide range 10-300 K, are investigated, in order to provide a systematic insight into the SSS effect, Labusch-type thermal activation process, SFE and twinning behavior in FCC HEA/HEAs. The main conclusion are as following:

(1) The high yield stress of these HEA/MEAs are indeed attributed to significant SSS model both by the traditional Labusch type model and the mean-square atomic displacement model. The results shows that the atomic size misfit dominate the SSS in these FCC HEA/MEAs, which is consistent with the long stand belief that edge dislocation predominate the plastic deformation of FCC alloys. Among the 3d-transition metals, the Cr play a significant role in size misfit thus the SSS in these alloys.

(2) The decrease of SFE in HEA/MEAs will induce additional deformation mechanism including deformation twinning and martensitic transformation, which will significantly increase the work hardening ability and thus the tensile ductility.

(3) The SFE of HEA/MEAs is found to be linearly related to their chemical compositions, which will be a power tool to control the SFE by composition optimization. The negative correlation between twinning shear stress and SFE may be explain by the twin-growth controlled twinning model instead of nucleation of twin embryo.

## Reference

- [1] Z. Wu, H. Bei, F. Otto, G.M. Pharr, E.P. George, Recovery, recrystallization, grain growth and phase stability of a family of FCC-structured multi-component equiatomic solid solution alloys, *Intermetallics*. 46 (2014) 131–140. <https://doi.org/https://doi.org/10.1016/j.intermet.2013.10.024>.
- [2] B. Gludovatz, A. Hohenwarter, D. Catoor, E.H. Chang, E.P. George, R.O. Ritchie, A fracture-resistant high-entropy alloy for cryogenic applications, *Science*. 345 (2014) 1153–1158. <https://doi.org/10.1126/science.1254581>.
- [3] Z. Wu, H. Bei, G.M. Pharr, E.P. George, Temperature dependence of the mechanical properties of equiatomic solid solution alloys with face-centered cubic crystal structures, *Acta Mater.* 81 (2014) 428–441. <https://doi.org/https://doi.org/10.1016/j.actamat.2014.08.026>.
- [4] Z.J. Zhang, M.M. Mao, J. Wang, B. Gludovatz, Z. Zhang, S.X. Mao, E.P. George, Q. Yu, R.O. Ritchie, Nanoscale origins of the damage tolerance of the high-entropy alloy CrMnFeCoNi, *Nat. Commun.* 6 (2015) 2–7. <https://doi.org/10.1038/ncomms10143>.
- [5] Z. Li, K.G. Pradeep, Y. Deng, D. Raabe, C.C. Tasan, Metastable high-entropy dual-phase alloys overcome the strength-ductility trade-off, *Nature*. 534 (2016) 227–230. <https://doi.org/10.1038/nature17981>.
- [6] G. Laplanche, A. Kostka, O.M. Horst, G. Eggeler, E.P. George, Microstructure evolution and critical stress for twinning in the CrMnFeCoNi high-entropy alloy, *Acta Mater.* 118 (2016) 152–163. <https://doi.org/https://doi.org/10.1016/j.actamat.2016.07.038>.
- [7] B. Gludovatz, A. Hohenwarter, K.V.S. Thurston, H. Bei, Z. Wu, E.P. George, R.O. Ritchie, Exceptional damage-tolerance of a medium-entropy alloy CrCoNi at cryogenic temperatures, *Nat. Commun.* 7 (2016) 1–8. <https://doi.org/10.1038/ncomms10602>.
- [8] G. Laplanche, A. Kostka, C. Reinhart, J. Hunfeld, G. Eggeler, E.P. George, Reasons for the superior mechanical properties of medium-entropy CrCoNi compared to high-entropy CrMnFeCoNi, *Acta Mater.* 128 (2017) 292–303. <https://doi.org/https://doi.org/10.1016/j.actamat.2017.02.036>.
- [9] Z. Wu, Y. Gao, H. Bei, Thermal activation mechanisms and Labusch-type strengthening analysis for a family of high-entropy and equiatomic solid-solution alloys, *Acta Mater.* 120 (2016) 108–119. <https://doi.org/https://doi.org/10.1016/j.actamat.2016.08.047>.
- [10] R.L. Fleischer, Substitutional solution hardening, *Acta Metall.* 11 (1963) 203–209. [https://doi.org/10.1016/0001-6160\(63\)90213-X](https://doi.org/10.1016/0001-6160(63)90213-X).
- [11] R. Labusch, A Statistical Theory of Solid Solution Hardening, *Phys. Status Solidi*. 41 (1970) 659–669. <https://doi.org/10.1002/pssb.19700410221>.
- [12] L.A. Gypen, A. Deruyttere, Multi-component solid solution hardening - Part 1 Proposed model, *J. Mater. Sci.* 12 (1977) 1028–1033. <https://doi.org/10.1007/BF00540987>.
- [13] L.A. Gypen, A. Deruyttere, Multi-component solid solution hardening - Part 2 Agreement with experimental results, *J. Mater. Sci.* 12 (1977) 1034–1038. <https://doi.org/10.1007/BF00540988>.

- [14] M. Z. BUTT, Review Solid-solution hardening, *J. Mater. Sci.* 28 (1993) 2557–2576.
- [15] M. Z. Butt, Investigation of the activation-parameters of low-temperature slip in cubic metals, *Czechoslov. J. Phys.* 49 (1998) 1177–1184.
- [16] I. Toda-Caraballo, P.E.J. Rivera-Díaz-del-Castillo, P.E.J. Rivera-Díaz-Del-Castillo, Modelling solid solution hardening in high entropy alloys, *Acta Mater.* 85 (2015) 14–23. <https://doi.org/10.1016/j.actamat.2014.11.014>.
- [17] C.C. Varvenne, A. Luque, W.A. Curtin, Theory of strengthening in fcc high entropy alloys, *Acta Mater.* 118 (2016) 164–176. <https://doi.org/10.1016/j.actamat.2016.07.040>.
- [18] C. Varvenne, G.P.M.M. Leyson, M. Ghazisaeidi, W.A. Curtin, Solute strengthening in random alloys, *Acta Mater.* 124 (2017) 660–683. <https://doi.org/https://doi.org/10.1016/j.actamat.2016.09.046>.
- [19] N.L. Okamoto, K. Yuge, K. Tanaka, H. Inui, E.P. George, Atomic displacement in the CrMnFeCoNi high-entropy alloy-A scaling factor to predict solid solution strengthening, *AIP Adv.* 6 (2016) 125008. <https://doi.org/10.1063/1.4971371>.
- [20] J.A. Venables, Deformation twinning, in: *Metall. Soc. AIME*, 1964: pp. 77–116.
- [21] J.A. Venables, Deformation twinning in face-centred cubic metals, *Philos. Mag. A J. Theor. Exp. Appl. Phys.* 6 (1961) 379–396. <https://doi.org/10.1080/14786436108235892>.
- [22] N. Narita, J. Takamura, Deformation twinning in silver- and copper-alloy crystals, *Philos. Mag.* 29 (1974) 1001–1028. <https://doi.org/10.1080/14786437408226586>.
- [23] J.W. Christian, S. Mahajan, Deformation twinning, *Prog. Mater. Sci.* 39 (1995) 1–157. [https://doi.org/https://doi.org/10.1016/0079-6425\(94\)00007-7](https://doi.org/https://doi.org/10.1016/0079-6425(94)00007-7).
- [24] B.C. De Cooman, Y. Estrin, S.K. Kim, Twinning-induced plasticity (TWIP) steels, *Acta Mater.* 142 (2018) 283–362. <https://doi.org/10.1016/j.actamat.2017.06.046>.
- [25] M.J. Szczerba, M.S. Szczerba, Slip versus twinning in low and very low stacking-fault energy Cu-Al alloy single crystals, *Acta Mater.* 133 (2017) 109–119. <https://doi.org/https://doi.org/10.1016/j.actamat.2017.05.011>.
- [26] S. Kibey, J.B. Liu, D.D. Johnson, H. Sehitoglu, Energy pathways and directionality in deformation twinning, *Appl. Phys. Lett.* 91 (2007) 2005–2008. <https://doi.org/10.1063/1.2800806>.
- [27] S. Kibey, J.B. Liu, D.D. Johnson, H. Sehitoglu, Predicting twinning stress in fcc metals: Linking twin-energy pathways to twin nucleation, *Acta Mater.* 55 (2007) 6843–6851. <https://doi.org/10.1016/j.actamat.2007.08.042>.
- [28] H. Huang, X. Li, Z. Dong, W. Li, S. Huang, D. Meng, X. Lai, T. Liu, S. Zhu, L. Vitos, Critical stress for twinning nucleation in CrCoNi-based medium and high entropy alloys, *Acta Mater.* 149 (2018) 388–396. <https://doi.org/https://doi.org/10.1016/j.actamat.2018.02.037>.
- [29] L. Deléhouzée, A. Deruyttere, The stacking fault density in solid solutions based on copper, silver, nickel, aluminium and lead, *Acta Metall.* 15 (1967) 727–734. [https://doi.org/10.1016/0001-6160\(67\)90353-7](https://doi.org/10.1016/0001-6160(67)90353-7).
- [30] P.C.J. Gallagher, The influence of alloying, temperature, and related effects on the stacking fault energy, *Metall. Trans.* 1 (1970) 2429–2461. <https://doi.org/10.1007/BF03038370>.
- [31] M. Kawamura, M. Asakura, N.L. Okamoto, K. Kishida, H. Inui, E.P. George, Plastic deformation of single crystals of the equiatomic Cr–Mn–Fe–Co–Ni high-entropy

- alloy in tension and compression from 10 K to 1273 K, *Acta Mater.* 203 (2021) 116454. <https://doi.org/10.1016/j.actamat.2020.10.073>.
- [32] L. Li, Z. Chen, S. Kuroiwa, M. Ito, K. Kishida, H. Inui, E.P. George, Tensile and compressive plastic deformation behavior of medium-entropy Cr-Co-Ni single crystals from cryogenic to elevated temperatures, *Int. J. Plast.* 148 (2022) 103144. <https://doi.org/10.1016/J.IJPLAS.2021.103144>.
- [33] P.R. Thornton, T.E. Mitchell, P.B. Hirsch, The strain-rate dependence of the flow stress of copper single crystals, *Philos. Mag.* 7 (1962) 337–358. <https://doi.org/10.1080/14786436208211866>.
- [34] E. Ashif, Deformation Mechanism of Single Crystals of F.C.C. Medium Entropy Alloys, Kyoto University, 2021.
- [35] V.A. Lubarda, On the effective lattice parameter of binary alloys, *Mech. Mater.* 35 (2003) 53–68. [https://doi.org/10.1016/S0167-6636\(02\)00196-5](https://doi.org/10.1016/S0167-6636(02)00196-5).
- [36] P. Jax, P. Kratochvil, P. Haasen, Solid solution hardening of gold and other f.c.c. single crystals, *Acta Metall.* 18 (1970) 237–245. [https://doi.org/10.1016/0001-6160\(70\)90029-5](https://doi.org/10.1016/0001-6160(70)90029-5).
- [37] Z. Dong, L. Vitos, Finite temperature magnetic properties of  $\text{Cr}_x\text{Co}_y\text{Ni}_{100-x-y}$  medium entropy alloys from first principles, *Scr. Mater.* 171 (2019) 78–82. <https://doi.org/10.1016/j.scriptamat.2019.06.019>.
- [38] M.L. Ali, Enhanced lattice distortion, yield strength, critical resolved shear stress, and improving mechanical properties of transition-metals doped CrCoNi medium entropy alloy, *RSC Adv.* 11 (2021) 23719–23724. <https://doi.org/10.1039/d1ra02073k>.
- [39] G. Laplanche, P. Gadaud, C. Bärsch, K. Demtröder, C. Reinhart, J. Schreuer, E.P. George, Elastic moduli and thermal expansion coefficients of medium-entropy subsystems of the CrMnFeCoNi high-entropy alloy, *J. Alloys Compd.* 746 (2018) 244–255. <https://doi.org/10.1016/j.jallcom.2018.02.251>.
- [40] G. Laplanche, M. Schneider, F. Scholz, J. Frenzel, G. Eggeler, J. Schreuer, Processing of a single-crystalline CrCoNi medium-entropy alloy and evolution of its thermal expansion and elastic stiffness coefficients with temperature, *Scr. Mater.* 177 (2020) 44–48. <https://doi.org/10.1016/j.scriptamat.2019.09.020>.
- [41] T. Teramoto, K. Yamada, R. Ito, K. Tanaka, Monocrystalline elastic constants and their temperature dependences for equi-atomic Cr-Mn-Fe-Co-Ni high-entropy alloy with the face-centered cubic structure, *J. Alloys Compd.* 777 (2019) 1313–1318. <https://doi.org/https://doi.org/10.1016/j.jallcom.2018.11.052>.
- [42] H. Suzuki, E. Kuramoto, Thermally activated glide in face-centered cubic alloys, *Trans JIM.* 9. (1968) 697–702.
- [43] X. Liu, Z. Pei, M. Eisenbach, Dislocation core structures and Peierls stresses of the high-entropy alloy NiCoFeCrMn and its subsystems, *Mater. Des.* 180 (2019) 107955. <https://doi.org/10.1016/j.matdes.2019.107955>.
- [44] M. Schneider, F. Werner, D. Langenkämper, C. Reinhart, G. Laplanche, Effect of temperature and texture on Hall–Petch strengthening by grain and annealing twin boundaries in the MnFeNi medium-entropy alloy, *Metals (Basel).* 9 (2019). <https://doi.org/10.3390/met9010084>.

## Chapter 5 Summary

The high-entropy alloys (HEAs), defined as complex solid solutions with multi-principal elements in high concentrations, have been recognized as a new class of promising structural materials since their first report in 2004. To date, the most widely studied families of Cr-Mn-Fe-Co-Ni with the face-centered cubic (FCC) structure, have attracted remarkable interest due to their excellent combination of strength & ductility from cryogenic to ambient temperatures. The strength and ductility of these HEAs are believed to be related to the complex solid solution configurations. However, the key parameters that essentially determine their excellent performances are still not clear. Based on the previous work, the mean-square atomic displacement (MSAD) and the stacking fault energy (SFE) have great potential to evaluate and predict the strength and ductility of HEAs.

Chapter 1 is a brief introduction about the background and the present research progress in the field of HEA/MEAs and other FCC alloys.

In Chapter 2, bulk single crystals of the equiatomic Cr-Co-Ni were tested in tension and compression between 14 K and 1373 K. At room temperature, the critical resolved shear stress (CRSS) for  $\{111\}\langle 100 \rangle$  slip is  $65 \pm 5$  MPa and does not exhibit a tension-compression asymmetry. A dulling of this temperature dependence occurs below 50 K, which may be due to the inertia effect. When the measured values above 50 K are extrapolated to lower temperatures, a value of 225 MPa is estimated for the CRSS at 0 K. This is larger than that (168 MPa) previously determined for the equiatomic Cr-Mn-Fe-Co-Ni high-entropy alloy. The stacking fault energy of the present Cr-Co-Ni is estimated to be about  $14 \text{ mJ/m}^2$ , which is sufficiently low to account for deformation twinning both

at 77 K and room temperature. Twinning at 77 K occurs on conjugate planes at an onset shear stress of 482 MPa after primary slip and propagates in the form of Lüders deformation. At room temperature, twinning occurs uniformly throughout the gauge section on primary (111) planes at an onset shear stress of 381 MPa after primary and subsequent conjugate slip. Thin layers with the hexagonal close-packed stacking are observed in association with twinning both at 77 K and room temperature.

In Chapter 3, short-range ordering (SRO), its evolution in the equiatomic Cr-Co-Ni medium-entropy alloy (MEA), and its effects on mechanical properties were investigated by, respectively, electrical resistivity measurements and tension and compression tests on single crystal specimens at room temperature and liquid nitrogen temperature. SRO below 973 K can be monitored by changes in electrical resistivity, which increases gradually with time to a saturation value during isothermal annealing in the temperature range of 673-973 K. While the time required to reach saturation is shorter at higher temperatures, the saturation resistivity is higher at lower temperatures, indicating a higher degree of SRO at lower temperature although it takes longer to reach saturation because of slower kinetics. No significant change in the plastic deformation behavior is found at room temperature and 77 K for different degrees of SRO. The yield stress as well as the slip localization behavior are basically the same after SRO, and the magnitude of yield drop does not correlate with the degree of SRO. Tensile stress-strain curves are not much affected by SRO up to high strain levels, resulting in identical shear stresses for the onset of deformation twinning at room temperature regardless of the degree of SRO. The dislocation structure, variations in dislocation dissociation width, and stacking fault energy are all essentially unchanged.

In Chapter 4, the plastic deformation behavior of single crystals of the equiatomic Cr-Fe-Co-Ni and Fe-Co-Ni MEAs both in tension and in compression as a function of temperature over a wide range 10-300 K, are investigated. The previous results of quinary Cr-Mn-Fe-Co-Ni and ternary Cr-Co-Ni are also included to provide a systematic insight into the SSS effect, Labusch-type thermal activation process, SFE and twinning behavior in FCC HEA/HEAs. The high yield stress of these HEA/MEAs are indeed attributed to significant SSS model both by the traditional Labusch type model and the mean-square atomic displacement model. The results shows that the atomic size misfit dominate the SSS in these FCC HEA/MEAs, which is consistent with the long stand belief that edge dislocation predominate the plastic deformation of FCC alloys. Among the 3d-transition metals, the Cr play a significant role in size misfit thus the SSS in these alloys. The decrease of SFE in HEA/MEAs will induce additional deformation mechanism including deformation twinning and martensitic transformation, which will significantly increase the work hardening ability and thus the tensile ductility. The SFE of HEA/MEAs is found to be linearly related to their chemical compositions, which will be a power tool to control the SFE by composition optimization. The negative correlation between twinning shear stress and SFE may be explain by the twin-growth controlled twinning model instead of nucleation of twin embryo.